



## Report Title

Student Support for Quantum Computing with Superconducting Charge States: Cavity QED with the Cooper-pair Box

### ABSTRACT

This project supplies support for an additional graduate student, Mr. David Schuster, on experimental investigations on quantum coherence, entanglement, and quantum computation in a solid-state, electronic realization of quantum bits based on superconducting single-electron devices, namely the single Cooper-pair box. Mr. Schuster has developed a process for fabrication of Al/AlO<sub>x</sub>/Al tunnel qubits with integrated transmission line resonators, and used these devices for cavity-QED manipulations and readout of qubits. This work has led to the first strong coupling of a solid-state qubit to a single photon, the first high-fidelity non-demolition readout of superconducting qubits, and the first high-visibility quantum control of superconducting qubits.

---

### List of papers submitted or published that acknowledge ARO support during this reporting period. List the papers, including journal references, in the following categories:

#### (a) Papers published in peer-reviewed journals (N/A for none)

- 1) "Cavity Quantum Electrodynamics for Superconducting Electrical Circuits: an Architecture for Quantum Computation," Alexandre Blais, Ren-Shou Huang, Andreas Wallraff, S.M. Girvin, and R.J. Schoelkopf, Phys. Rev. A 69, 062320 (2004).
- 2) "Coherent Coupling of a Single Photon to a Superconducting Qubit Using Circuit Quantum Electrodynamics," A. Wallraff, D. Schuster, Alexandre Blais, L. Frunzio, Ren-Shou Huang, J. Majer, S. Kumar, S.M. Girvin, and R.J. Schoelkopf, Nature 431, 162 (2004).
- 3) "AC Stark Shift and Dephasing in a Superconducting Qubit Strongly Coupled to a Cavity Field," D.I. Schuster, A. Wallraff, Alexandre Blais, L. Frunzio, Ren-Shou Huang, J. Majer, S.M. Girvin, and R.J. Schoelkopf, Phys. Rev. Lett. 94, 123602 (2005).
- 4) "Fabrication and Characterization of Superconducting Circuit QED Devices for Quantum Computation," L. Frunzio, A. Wallraff, D. Schuster, J. Majer, and R.J. Schoelkopf, IEEE Trans. on Applied Superconductivity 15, 860 (2005).
- 5) "Approaching Unit Visibility for Control of a Superconducting Qubit with Dispersive Readout," A. Wallraff, D.I. Schuster, A. Blais, L. Frunzio, J. Majer, M.H. Devoret, S.M. Girvin, and R.J. Schoelkopf, Phys. Rev. Lett. 95, 060501 (2005).

Number of Papers published in peer-reviewed journals: 5.00

---

#### (b) Papers published in non-peer-reviewed journals or in conference proceedings (N/A for none)

Number of Papers published in non peer-reviewed journals: 0.00

---

#### (c) Papers presented at meetings, but not published in conference proceedings (N/A for none)

Number of Papers not Published: 0.00

---

#### (d) Manuscripts

Number of Manuscripts: 0.00

---

Number of Inventions:

---

#### Graduate Students

David Schuster 100%

**Number of Graduate Students supported:** 1.00

**Total number of FTE graduate students:** 1.00

---

**Names of Post Doctorates**

**Number of Post Docs supported:** 0.00

**Total number of FTE Post Doctorates:** 0.00

---

**List of faculty supported by the grant that are National Academy Members**

---

**Names of Faculty Supported**

**Number of Faculty:** 0.00

---

**Names of Under Graduate students supported**

**Number of under graduate students:** 0.00

---

**Names of Personnel receiving masters degrees**

**Number of Masters Awarded:** 0.00

---

**Names of personnel receiving PHDs**

**Number of PHDs awarded:** 0.00

---

**Names of other research staff**

---

**Sub Contractors (DD882)**

**Inventions (DD882)**



## Results from the period 1/03-1/04

A summary of achievements in this period:

### I. Fabrication:

- Commissioned new fabrication setup (with M. Devoret), students and postdocs have gained expertise in fabrication.
- Produced and tested single-electron transistors and CPB qubits at Yale.
- Characterized junction areas and energy scales, can now fabricate qubits with specified transition frequencies.
- Produced detailed mask design for coupled two-qubit gate using CPB and SET readouts.
- Demonstrated fabrication process for qubits and SETs with controlled high-frequency coupling, including chip level microwave design.
- Began fabrication development for qubits with higher transition temperatures and superconducting bandgap engineering.
- Developed fab process for high quality-factor superconducting cavities.
- Developed process and fabricated single and multiple qubits integrated to cavities, devices are under test.

### II. Cavity QED Experiments with Cooper-pair Box Qubits:

- Tested quality factors of both Al and Nb transmission-line resonators, including temperature and magnetic field dependence.
- Obtained high quality factor resonators (Nb) with  $Q > 500,000$  at 250 mK
- Assembled and tested 5-10 GHz microwave readout system for cavity-based QND measurement of qubits
- Designed both one qubit and two coupled qubit designs for scQED architecture.
- Tested signal-to-noise of pulsed cavity readout, found high-fidelity single-shot readout of qubits should be possible.
- Testing of single qubits in cavities underway.

### I. Process Development and Fabrication of Superconducting Qubits at Yale University

This year has seen great progress in our fabrication capabilities at Yale. In collaboration with Michel Devoret's group, a robust process for Al/AlOx/Al shadow evaporated junctions has now been realized, so that single-electron transistors and CPB qubits can be produced, with a typical cycle time of one or two days. Steady progress has been made in reducing feature sizes to yield devices with appropriately large charging energies for sensitive SETs. An electron micrograph of such an SET is shown in Figure 1, along with an enlargement showing the actual junction region, consisting of crossed lines  $< 75$  nanometers in width.

Typically the basic device testing is performed in a Helium-3 refrigerator down to 250 mK. Conventional dc transport measurements of approximately a dozen SETs and test qubits can be performed in a single cool-down, lasting a couple of days to a week. At least six such design/fabricate/test cycles have been carried out in the last few months. Charging energies of the SETs are extracted from I-V characteristic measurements, as well as measurements of the RF "charging diamonds" of an RF-SET. A typical sample consists of 10 to 20 SETs and a similar number of test CPB qubits, which are small area SQUIDs configured for I-V curve measurements, rather than being measured as a qubit using an SET. This allows measurements of the resistance, critical current, sub-gap I-V characteristics, and flux modulation patterns, each of which are useful for determining important qubit characteristics. Successive iterations of this processing and testing has resulted in good control of the junction areas, current densities, and resistances, which can be reproduced to approximately 20% tolerances. This means that we can fabricate CPB qubits with good control over the energy spectrum of the qubit, in order to minimize problems with quasiparticles and parity, and to yield an optimal set of transition frequencies.

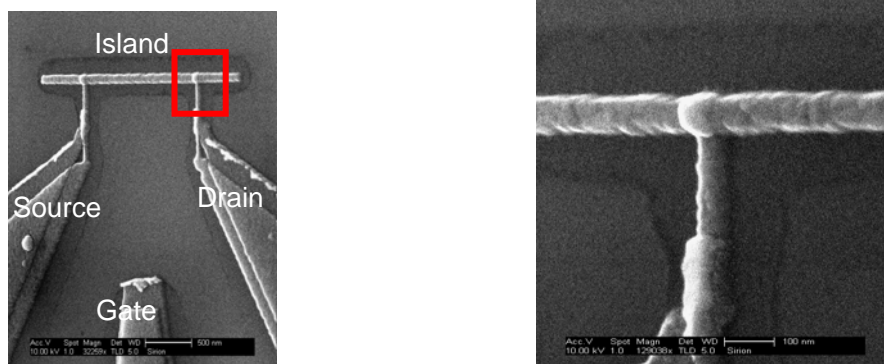


Figure 1: Electron micrograph of finished SET device fabricated at Yale (by D. Schuster and L. Frunzio). Left image shows overview of the SET, with the island, drain, source and gate labeled. Such a device has a charging energy  $E_C \sim 1$ -3 Kelvin. Right image shows a detail of one of the small junctions, with linewidths less than 75 nanometers.

We have also designed a new generation of sample holders with the goal of efficiently coupling microwave signals to qubits, and to present our qubits with a well-engineered, broad-band 50 Ohm electromagnetic environment. We have used custom-made microwave circuit boards with vias, and developed a coupling scheme using surface-mount SMP launchers, which can convert from a coaxial input to an on-board balanced transmission line, in a coplanar waveguide (CPW) geometry. This has the advantage that broadband interconnects to the chip can be made using conventional wire bonding, also available in our lab. In order to exploit the

advantages of this design philosophy, the qubit and SET chip must also incorporate these CPW lines. These can then be fabricated to make a constant impedance, broadband taper from the millimeter scale to the micron scale of the qubits. This required a combination of the fine-line electron-beam lithography and large scale patterning with our e-beam lithography system. This process was developed, and a test sample using this design is shown in Figure 2. Fabrication of actual qubit/readout chips is underway, and first tests will measure the capacitive coupling and quality of the junctions configuring them as a pair of coupled SETs. This fabrication and testing is underway. The chip-level microwave engineering is important in allowing fast microwave pulses for qubit control, and in preventing anomalous relaxation due to environmental resonances, and has not so far proven feasible with samples fabricated at Chalmers.

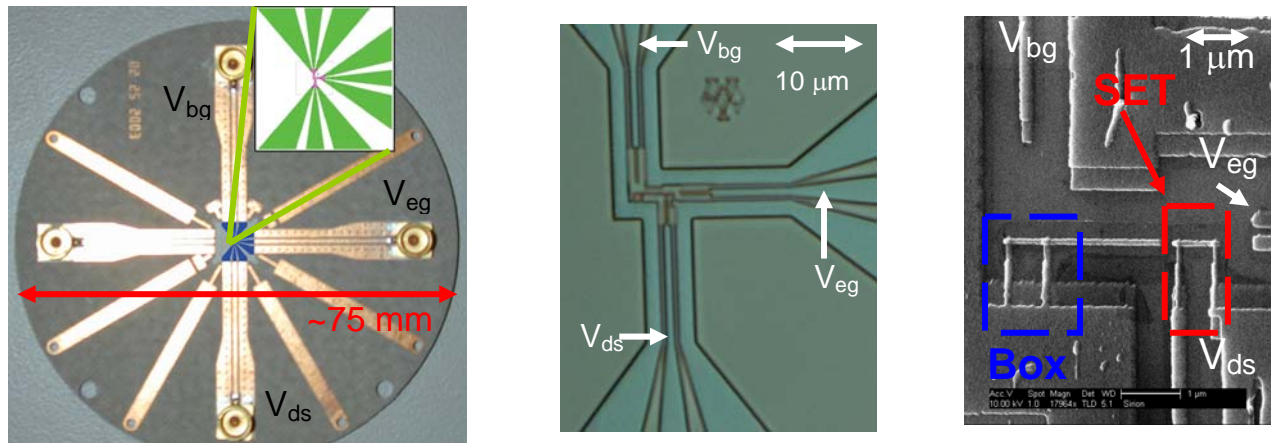


Figure 2: Pictures of Box+SET samples designed for efficient coupling of microwave pulses and control of the electrical environment to limit relaxation rates. A) Left panel shows a custom microwave circuit board, with 4 coplanar waveguide (CPW) lines for high frequency signals. The 5 x 5 mm chip containing SET and CPB qubit is placed in a machined recess at the center of the board. B) Optical micrograph of a test sample, fabricated at Yale, which incorporates CPW line tapers to match the device to circuit board. C) SEM image of a sample containing CPB box qubit, and readout SET in this optimized geometry.

Another effort in design has looked at extending this type of design to a coupled qubit system for demonstrating simple gates. This requires two CPB qubits with capacitive coupling, and two individual RF-SETs for readout of the qubit states. A mask design for such a circuit is shown in Figure 3, and is intended for use with the same sample holder and design philosophy as described above for single qubits. Schemes for two qubit control and gate operation with such a circuit have been investigated by our theory team, as described in section III below.

Other fabrication work has investigated a possible process for producing qubits with higher  $T_c$  superconductors, in order to reduce the importance of quasiparticle effects. We have invested in some techniques for etching tantalum islands ( $T_c = 4$  K), and also experimented with oxygen-doped aluminum films, which can have  $T_c$ 's up to 2 Kelvin.

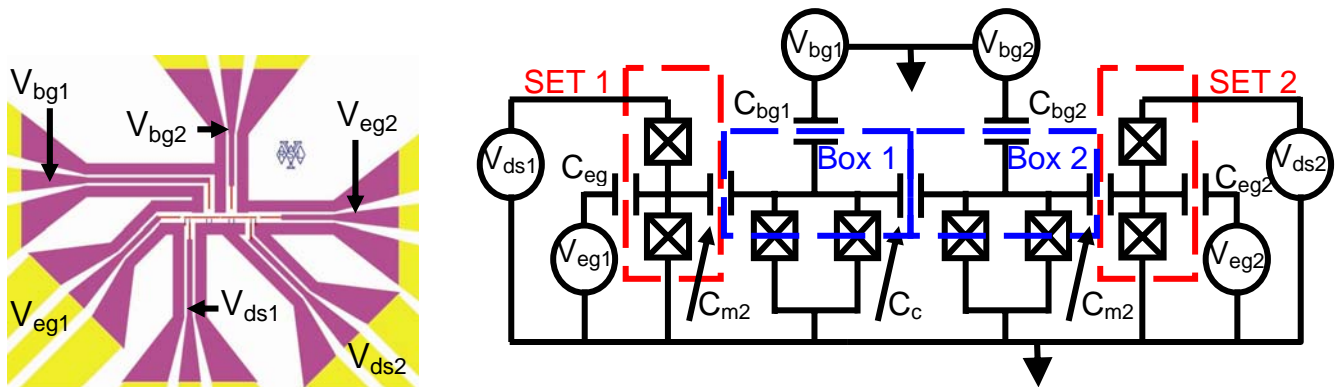


Figure 3: Left: Mask design for a two-qubit gate using CPB qubits and SET readouts. All lines are coupled to CPW transmission lines. Right: a circuit schematic of the two qubit-two SET readout circuit. The boxes have a fixed coupling by a capacitor. Operation protocols for such a gate have been theoretically investigated and described below.

The final area of work in fabrication has been in the production of high-Q resonant cavities for the scQED architecture (see description of the architecture below in Section III, and of recent experimental progress in Section IV). Optical lithography is used to produce approximately 30 resonators at a time on a two-inch silicon or sapphire wafer. Two different generations of optical masks have been designed and tested. Resonators with both aluminum and niobium superconducting films were made and tested down to 250 mK, showing more than adequate quality factors. We have also developed several techniques for integrating CPB qubits into the resonant cavities to achieve the scQED architecture. This uses the standard process for Al shadow-evaporated junctions, described above, and fabricated within the resonator by direct write, after aligning to the resonator structure to tolerances of about 150 nanometers. An example of both single and multiple qubits inside one of these resonators is shown in Figure 4. Testing of such qubits at 20 mK is underway.

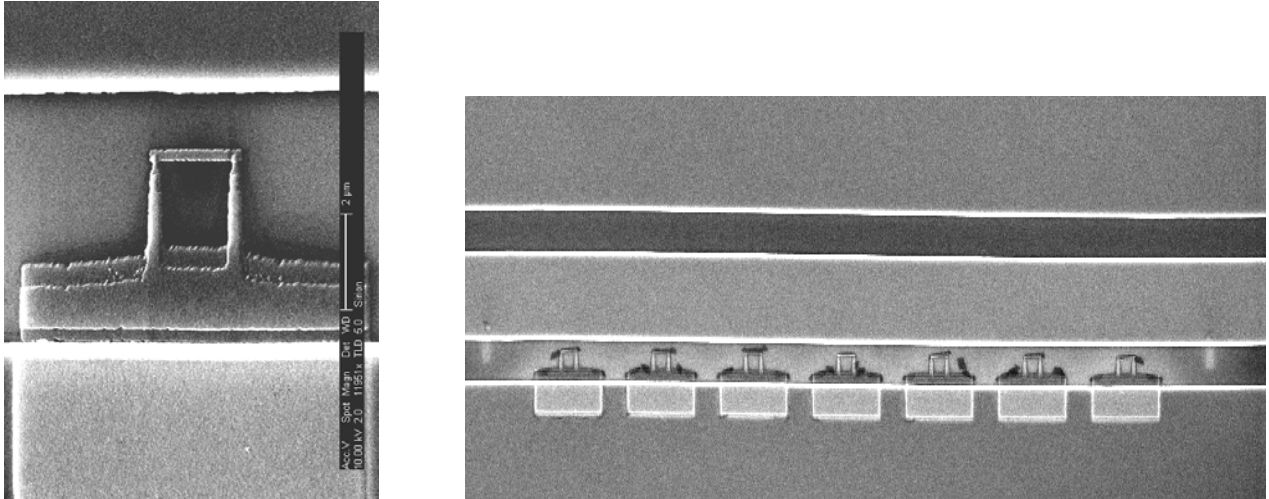


Figure 4: Electron micrograph of CPB qubits inside transmission line resonators. Shown are a single qubit, with an island, two junctions, and a small SQUID loop to allow tuning of the Josephson energy. On right is a test sample with seven qubits coupled to a single resonator.

## II. Cavity QED Experiments with Cooper-pair Box Qubits:

A major part of our experimental effort has been directed to implementing the cavity QED architecture for quantum computing with superconductors described briefly above. The concept for this architecture, described above, has been presented at several international conferences and workshops, and submitted for publication to Physical Review B. The technology for the design, fabrication, and measurement of these devices has been developed, initial devices have been fabricated, and the first measurements are now underway. Future plans for this approach are discussed in section V.

One of the first tasks for implementing the cQED experiments was to master the design and fabrication of the cavities themselves. These are fabricated in our cleanroom at Yale using optical lithography (see section I). We have designed and tested resonant cavities from two generations of optical masks, and tested the quality factors of several different designs in both Al and Nb at temperatures down to 250 mK. These results have been very encouraging, as high quality factors (in excess of  $10^5$ ) are routinely observed. Our present designs use Nb resonators, in which we have attained quality factors of nearly a million ( $>600,000$ ) at 100 mK. Our proposal and first generation devices only require a quality factor of about 10,000, which we easily obtain by strongly coupling the resonator to its input and output. We also studied the temperature and magnetic field dependence of the cavity losses, and found that though affected by large magnetic fields, the cavities can retain their high Q's even for fields of 10-100 Gauss, which is large enough to allow the Josephson energy of the qubit to be widely tuned via the simple application of a global field.

In order to perform such tests, we designed and implemented a new sample holder which allows for good high-frequency coupling to the resonators, without exciting spurious resonances that can confuse the measurement of a weakly coupled resonator. A picture of such a sample holder, incorporating a custom microwave circuit board with vias, is shown in Figure 11, along with a representative measurement of a single resonator transmission spectrum. This setup has two coaxial inputs, allowing the measurement of the transmission, and also allowing for separate control and measurement of a two-qubit cQED gate, as described below.

A further advantage of this cQED architecture is that it is trivial to imagine multi-qubit couplings, as the resonator itself can be used as a quantum bus to make entanglement between different qubits. Since the size of the CPB qubit is small compared to the dimensions of the resonator a large number of qubits can easily be fabricated inside a single cavity (see Figure 4). In order to operate multiple qubits inside the cavity, however, their offset charge must be separately controlled and set to the optimum value at the charge degeneracy point of the box. For the initial step to two qubits, this can be done without any additional complexity in fabrication or wiring, by placing the qubits within the resonator, but close enough to opposite ends so that there is a selective coupling from the input and output coaxial port to the individual qubits. This is shown schematically in Figure 12 below, along with a detailed drawing of the geometry near the end and the results of a finite-element capacitance simulation for the box and control wiring.

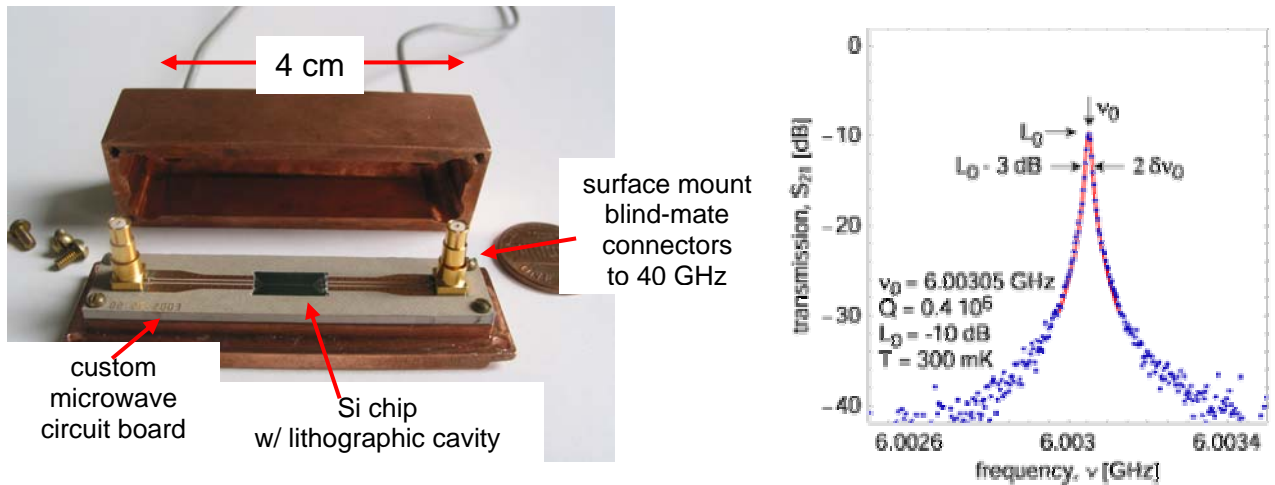


Figure 11: (left) Sample holder for high-frequency measurements of microwave transmission line resonators. (right) Measurement of a niobium coplanar-waveguide resonator at 250 mK, showing a quality factor in excess of 400,000, at a resonant frequency (full-wave resonator) of about 6 GHz.

In the last year we also built up a microwave test setup for measuring the transmission through the cavities and controlling the qubits within the cavities. A schematic of this apparatus, which includes the possibility to perform both single and two-qubit operations and measurements, is shown in Figure 13. The resonator has two equivalent ports, one of which is the transmit arm (on left), and the other the receive arm (right). Each arm has a bias-tee that allows the introduction of separate dc voltages to control the offset charge and tune the qubits separately into resonance with the cavity or with each other. The transmit arm connects to microwave generators at room temperature. Microwave pulses at different frequencies are used to perform one-bit rotations by irradiating at the transition frequencies of the two qubits. With our theory collaborators, we are also investigating ways in which a third microwave frequency can effectively turn the two-qubit coupling on and off, to effect two-qubit operations and yield a CNOT. Finally, the readout is to be performed by irradiating on the transmit line near the cavity frequency (typically 6-10 GHz), and measuring the transmitted signal using a low noise cryogenic HEMT amplifier, located on the receive arm. The phase shift of the cavity is predicted to be as large as 180 degrees for different states of a single qubit. In the case of a two-qubit sample, two pulses at slightly different frequencies can in principle yield two bits of classical information, allowing access to the states of both qubits, without introducing any additional wiring or channels for decoherence. We are optimistic that this minimal approach and relatively low complexity of this two-qubit setup make it a logical next step that can be attempted shortly after the characterization of single-qubit cQED samples.

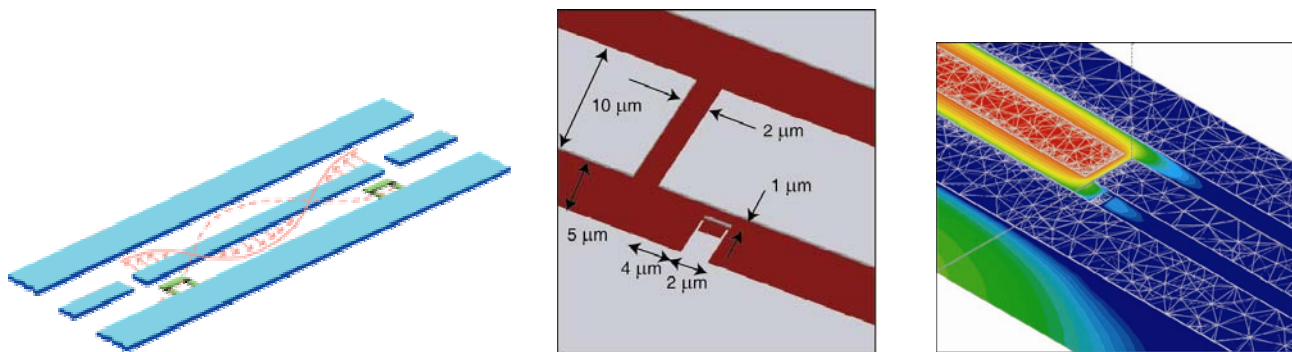


Figure 12: Design for a two-qubit gate in the superconducting cavity QED architecture. Two Cooper-pair boxes are placed near the ends of a transmission line resonator, so that they are coupled to the common electromagnetic mode. Two qubit interactions are effected by tuning the qubits into resonance with one another, via the combination of dc and ac signals on their gates. Center panel shows a detail of the physical layout of the CPB qubit near the end of the transmission line, and the right panel shows results of a finite-element electrostatic simulation of the geometry, from which the capacitances of the circuit are determined. This design shows that it will be possible to individually address two qubits from opposite ends of the resonator, without inducing a substantial channel for decay into the external electromagnetic environment.

The apparatus shown in Figure 13 has been tested in our  $^3\text{He}$  refrigerator at 250 mK, and is presently installed in our dilution refrigerator and being used for tests of our first cQED samples with single qubits. In earlier tests on a cavity without a qubit, however, we performed several tests of the signal-to-noise expected for the cQED readout. First, we were able to show that even with the measurement and control lines in place, the photon occupancy of the cavity is small, less than a few photons, and probably in agreement with the number expected from thermal equilibrium at about 300 mK. Second, we were able to measure the noise temperature of the new HEMT amplifier, and found it to be as low as about 20 photons (6 K at 6 GHz), about five times better than our estimate used in the design study. To determine whether the phase shift through the cavity, and eventually the qubit state, can be

detected in a single-shot measurement lasting less than a few microseconds, we made histograms of the measured transmission phase, and inserted a phase shift of  $\pi$  at room temperature on the transmitting arm. Histograms showing the probability of occurrence for different measured phases are shown in Figure 14, for integration times of 300 nanoseconds and 1.5 microseconds, respectively. The fidelity for distinguishing between these two “classical” bits was greater than 90% and 99%, respectively. In a real experiment with a qubit, the maximum integration time, and thus the signal-to-noise and the fidelity, are entirely determined by the observed lifetime ( $T_1$ ) of the qubit. Using the cQED architecture, one may hope for this time to exceed 50 microseconds, and the readout to be very efficient. However, this lifetime can be limited by many so far unknown processes, and therefore the determination of the  $T_1$  lifetime limits for a box in the cavity remains one of our first priorities.

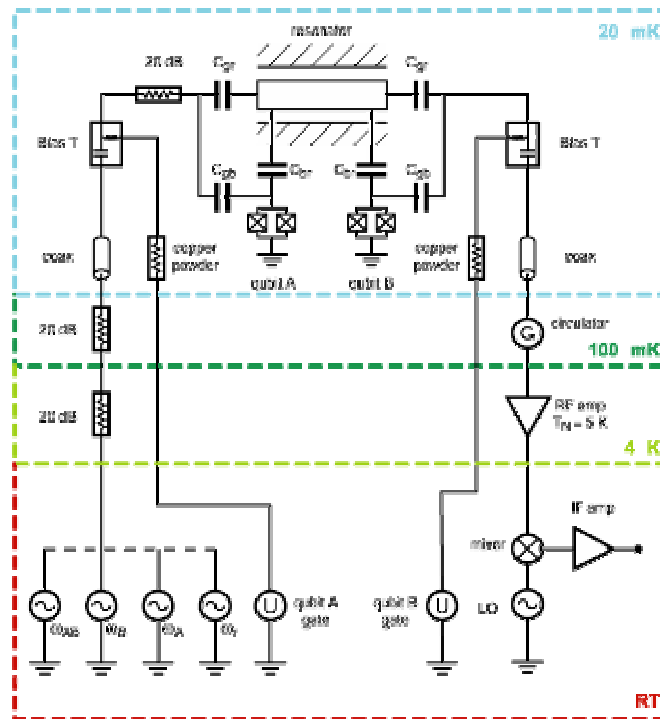


Figure 13: Schematic of the microwave apparatus for control and measurement of the cQED qubits. On left is the transmit arm, which connects the resonator to microwave sources at room temperature for generating one and two-qubit rotations. The selectivity is accomplished by using different frequencies, which are coupled to the qubits with some additional filtering by the resonator. Individual biasing of the gates of the two Cooper-pair boxes is provided by the lines coupled to the two arms via bias-tees. On the right is the receive arm, with cryogenic circulators and HEMT amplifier for performing readout via the phase of the cavity transmission.

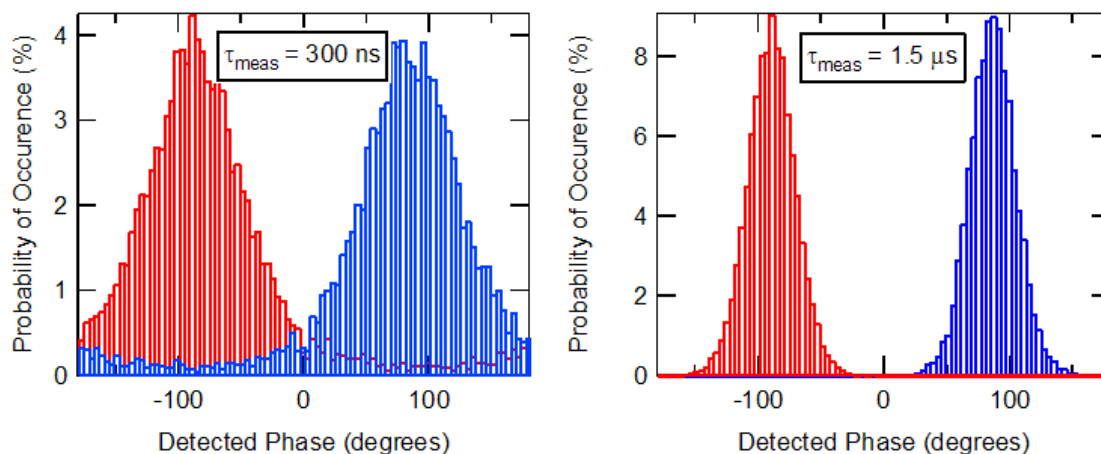
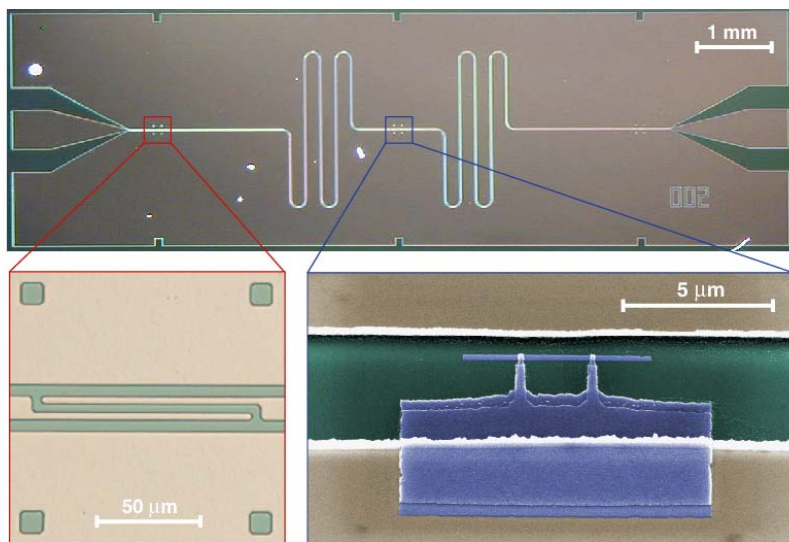


Figure 14: Test of the phase sensitive detection technique for the cQED resonators. A phase shift of 180 degrees was introduced on the transmit arm, and sent through an overcoupled resonator at 250 mK. The readout pulses had a magnitude of about 100 photons, and a duration of 300 ns and 1.5 microseconds, respectively. The fidelity for measurement of this classical bit was greater than 90% and 99% in the two cases, and was consistent with the noise expected from the first stage HEMT.

## Results from the period 1/04-8/31/04

In a joint experiment/theory collaboration we have conceived in the last two years a new architecture for quantum computation, adapting the idea of cavity QED (quantum electrodynamics) from atomic physics to superconducting electrical circuits, an idea that we refer to as cQED or 'circuit quantum electrodynamics' (see paper 1 below). During the past year we successfully implemented this new paradigm of 'quantum optics on a chip' and have two significant publications in *Nature* (Sept. 9, 2004, see paper 2 below) and *Phys. Rev. Lett.* (in press, see paper 3) which have confirmed the predictions in our proposal paper. This work was featured in the *Search and Discovery* section of the November issue of *Physics Today* and has attracted considerable interest within the atomic physics community and the superconducting qubit communities in the US and Europe. (see our website, [www.eng.yale.edu/rslab](http://www.eng.yale.edu/rslab) for more info)

To achieve these cQED results, we employed devices fabricated in our nanofabrication facility at Yale, using a process for Nb transmission line resonators, patterned with optical lithography, combined with Cooper-pair box (CPB) qubits using submicron Al/AIOx/Al made with direct-write electron beam lithography. This process was developed during the previous year, and testing of the first devices began in January of 2004. An optical/SEM micrograph of such an integrated device, used for the work reported in *Nature*, is shown in Figure 1 below.



**Figure 1:** Micrograph of a superconducting integrated circuit for cavity QED experiments in control and measurement of a CPB qubit (adapted from paper 2). The Nb resonator (top), on a Si substrate, is patterned using optical lithography. An interdigitated capacitor (lower left) provides relatively strong coupling ( $Q \sim 10,000$ ) of microwave signals in and out of the resonant cavity. A false color image (lower right) of the Al CPB qubit (blue), embedded at the center of the resonator. A loop allows control of the effective Josephson energy, and a dc voltage applied to the center conductor of the resonator provides the gate bias to control the Coulomb energy and allow operation at the charge degeneracy point.

We were then able to use the combined cavity-qubit system to perform a new type of dispersive measurement (**Milestone 2**) of the CPB qubit's ground and excited state properties. Microwave signals, with powers such that the cavity is typically occupied with 1 to 100 photons, were transmitted through the cavity. When the qubit is detuned in frequency from the cavity by several MHz to a GHz, these photons do not create any excitation or relaxation of the qubit. However, the qubit acts as an effective dielectric medium in the cavity, whose sign is positive or negative, depending on whether the qubit is in its ground or excited state. This creates a frequency shift of the cavity which can be an appreciable fraction of the cavity's linewidth, leading to an easily measurable phase shift of the transmitted signal. This measurement is unique so far amongst readouts for solid-state qubits in that it is a completely dissipation-free: it cannot excite the qubit, nor are any quasiparticles created or any photons absorbed within the chip. This technique appears to be a significant help in reducing the coupling to external degrees of freedom, and preserving the coherence and fidelity of the qubit itself.

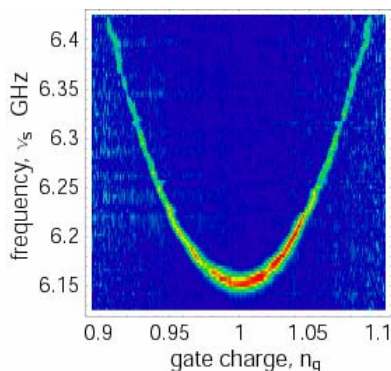


**Figure 2:** Spectroscopy of CPB qubit using cavity QED readout. The color scale shows the phase shift on a probe beam transmitted through the cavity at 6.0443 GHz, which is proportional to the excited state population. A continuous wave pump beam, whose frequency is varied from 6.1 to 6.5 GHz (vertical axis), excites the qubit when it matches the qubit transition frequency. The gate charge applied to the CPB is plotted on the horizontal axis, and the charge degeneracy point (gate charge of 1) is in the center of the plot, where the transition frequency is determined only by the Josephson energy, and the qubit is insensitive to  $1/f$  charge noise.

We then performed spectroscopy on the qubit, by adding a second microwave tone which was tuned to the qubit transition frequency. Though this signal is attenuated by the cavity, it can nevertheless be made sufficiently strong to drive transitions in the qubit, and can further be pulse modulated to produce control of the qubit state. Measuring the change in the phase shift in response to this spectroscopic signal, we performed spectroscopy on the qubit as a function of frequency, shown in Figure 2. One notices that this spectrum is extremely clean, displaying none of the spurious junction resonances seen in larger junctions by Martinis and coworkers. Also, the transition can be followed smoothly down to the charge degeneracy point (center of Fig. 2), where the energy level separation of the qubit is an extremum, and the qubit is first-order insensitive to  $1/f$  noise in the offset or gate charge. This point is found to give greatly enhanced coherence times for the CPB qubit. It can also be seen that the spectroscopic lines are sharp – one can use these linewidths to obtain a **worst-case estimate** of the coherence time indicating that  $T_2$  is greater than 200 ns. These times have since been confirmed in Ramsey and Rabi experiments, showing coherence times up to 800 ns, corresponding to a phase quality factor  $Q_\phi = \omega_{01}T_2 \sim 25,000$ , allowing in principle thousands of one-bit operations. This spectroscopy constitutes the first coherence time measurements on a qubit fabricated at Yale. Similarly encouraging results have been obtained by M. Devoret and co-workers, with devices measured at Saclay in France.

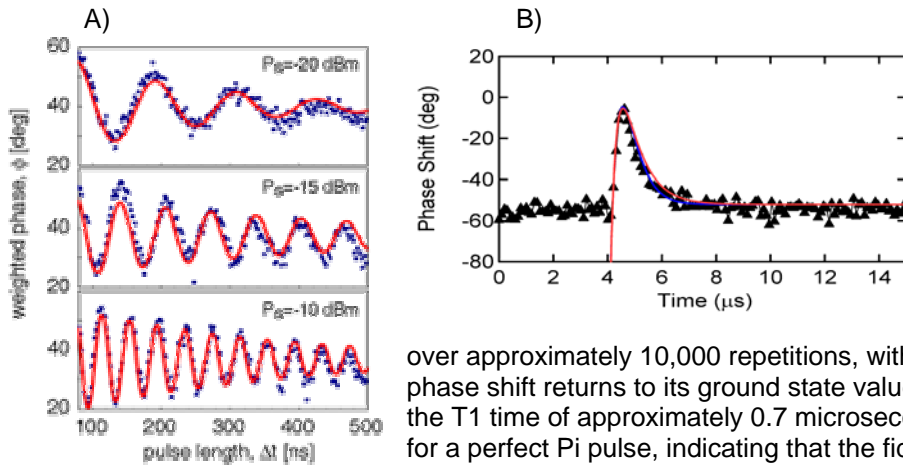


Figure 3: Rabi oscillations of a CPB qubit in a cavity. A) The phase shift, proportional to the excited state population, is plotted as a function of the length of the microwave pulse applied to the qubit. Increasing the power in the pulse (successive panels), increases the Rabi frequency. B) The response in time domain to a single Pi pulse, averaged over approximately 10,000 repetitions, with a weak continuous measurement. The phase shift returns to its ground state value as the excited-state population decays in the  $T_1$  time of approximately 0.7 microseconds. Red line shows predicted phase shift for a perfect Pi pulse, indicating that the fidelity of the oscillations is greater than 50%, and consistent with full contrast (100%).

To perform coherent control of the qubit in the cavity, we applied pulses of microwaves tuned to the qubit frequency. Since these are detuned from the cavity by 10 MHz to 1 GHz, their rise and fall times are simply limited to the inverse of this detuning, or about 1 to 100 nanoseconds. The response of the qubit to a pulse of microwaves, showing Rabi oscillations, is shown in Figure 3A. The Rabi frequency is observed to depend on the RF amplitude (not power), doubling for every 6 dB in microwave power, as expected. The fastest Rabi flops performed to date are about 30 ns, but this is still limited only by the microwave power applied and the pulse modulation electronics. An advantage of the cQED dispersive measurement, which is a quantum non-demolition (QND) measurement, is that it can be used either as a strong pulsed measurement, or as a weak continuous measurement, and it is particularly simple to understand. A time trace, showing the response of a weak continuous measurement (averaged over about 10,000 shots) with a Pi pulse is applied at  $\sim 4$  microseconds, is shown in Figure 3B. The phase shift of the cavity should be equal and opposite between ground and excited state, so we know the degree of polarization change induced in the qubit. The decay of the phase back to the ground state value (-60 degrees), is a direct measurement of the energy relaxation, or  $T_1$ , time of the qubit, here about 0.7 microseconds. The measurement rise time is simply determined by the photon lifetime in the cavity (i.e. the inverse of the cavity decay rate,  $\kappa^{-1} = Q / \omega_{cavity}$ ). The observed phase shift indicates at least 50% fidelity for the Pi pulse, but because of the low-pass filtering effect of the cavity lifetime, the data are also consistent with fidelity of order 100%. More recent measurements have improved the  $T_1$  time of the qubit, and the separation between these two timescales, so that the fidelity can be more accurately determined.

The relaxation time of 0.7 microseconds observed in Fig 3, is similar to the best results observed with superconducting charge qubits, namely the earlier Yale/Schoelkopf measurements (Lehnert et al., 2003) using an RF-SET, and the results of Devoret and co-workers at Saclay. Because the detuning of the qubit from the cavity is predicted to reduce the spontaneous emission rate of qubit and enhance the  $T_1$  time, however, it these cQED measurements indicate that there is an intrinsic, or local, source of dissipation that can limit the ultimate coherence times of these devices. The cQED architecture is an ideal way to study these mechanisms, and improving the relaxation times, is a topic for future work in this project. We have already fabricated cQED samples on different dielectric substrates in order to determine if this affects the relaxation.

Taking advantage of the tunability of the CPB qubit, we were also able to investigate the resonant regime of cavity QED, where the qubit's transition matches the cavity frequency, and observe coherent superpositions between our qubit and a single microwave photon. This required control of the CPB qubit Hamiltonian to a few parts in 10,000, so that the transition frequency at the degeneracy point is equal to the 6.044 GHz cavity frequency. In this case, the dipole coupling between the qubit and the cavity induces vacuum Rabi oscillations, at a rate  $2g=12$  MHz. This was observed

spectroscopically by measuring the splitting of the cavity transmission into a doublet of peaks, separated by the splitting  $2g$ , as shown in Figure 4 (adapted from Wallraff et al., Nature, paper 2). The two peaks correspond to excitation of the symmetric and anti-symmetric superpositions ( $|\pm\rangle = |\downarrow, n=1\rangle \pm |\uparrow, n=0\rangle$ ) of the qubit in its ground (excited) state  $|\downarrow\rangle(|\uparrow\rangle)$  and one (zero) photons in the cavity  $|n=1\rangle(|n=0\rangle)$ , and are expected to be entangled states, though that has not yet been demonstrated by correlation measurements. The width of these peaks is due to the combination of qubit and photon decay, since the states have a mixed qubit/photon character. The separation of the peaks by more than 10 linewidths indicates that our sample is clearly in the strong coupling limit of cavity QED, and that coherent exchange between qubit and cavity states is taking place. This also indicates that future experiments can use the cavity as an intermediary “bus” to transport entanglement across a chip to a different qubit, not necessarily a nearest-neighbor. Performing swap operations of the qubit and cavity, and between two qubits, is planned for the next year’s work.

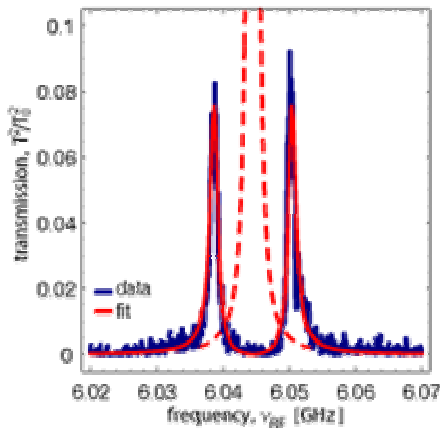


Figure 4: Vacuum Rabi splitting of the cavity mode due to coupling with a CPB qubit. The transmission through the cavity is plotted as a function of frequency, for a measurement probe beam of approximately -170 dBm, corresponding to 0.1 photons of excitation in the cavity. Dashed line shows the transmission through the bare resonator, when the qubit is strongly detuned, which has a Lorentzian shape with a Q of 10,000. Blue lines show the measured data when the qubit is tuned to resonance with the cavity frequency at the qubit charge degeneracy point. Solid red lines show a model prediction, based on the vacuum Rabi coupling strength  $2g = 12$  MHz extracted from measurements in the dispersive regime, the measured cavity quality factor, and a single fit parameter for the qubit transition linewidth,  $T_2 = 200$  ns. The clear separation of the peaks indicates that we are in the strong coupling limit of cavity QED, for the first time in a solid-state system. (Adapted from Wallraff et al., Nature 2004, paper 2)

Finally, we have fabricated cQED samples with multiple CPB qubits. Our second dilution refrigerator, already almost 1.5 years overdue, was further delayed and has only been commissioned in November 2004. We anticipate that testing of these multi-qubit devices will begin in 2005, when the new fridge has been instrumented and tested for microwave experiments. We have also observed the AC Stark shift of our qubits due to the measurement probe beam, and the dephasing that this induces in the qubit, which is described in the theory section below, and has been submitted to Physical Review Letters (Schuster et al., 2004, see paper 3 below). This means that we have a good understanding of the measurement-induced backaction of the cQED readout, when it is used as a weak continuous measurement. We have also performed pulsed measurement experiments with the cQED system, this work is in progress and will be described later. However, turning off the measurement is observed to enhance the coherence time of the CPB qubit in the cavity, leading to a record coherence time of 0.8 microseconds, as measured in a Ramsey experiment. The AC Stark shift can also be used in future as a mechanism for producing a single qubit phase gate, or to shift two qubits into resonance.

## Results from the period 8/04-8/05

### A listing of milestones achieved in this period: (from August 2005 program review)

- 1) Developed model and quantitative predictions for fidelity of continuous measurements.
- 2) Performed single-shot cavity QED readout with 40% fidelity.
- 3) Measured  $T_2 > 500$  ns and  $T_1 > 7$   $\mu$ s for CPB qubit w/ cQED dispersive readout.
- 4) Observed Rabi oscillations with  $> 95\%$  visibility.
- 5) Performed first experiments on two qubits in a cavity.

We have continued our very successful experiments on a new architecture for quantum computation, adapting the idea of cavity QED (quantum electrodynamics) from atomic physics to superconducting electrical circuits, an idea that we refer to as cQED or 'circuit quantum electrodynamics'. During the past year we have published our work on the AC Stark shift and the dephasing due to continuous measurements using the cavity as a quantum non-demolition probe of the state of the qubit (Schuster et al. PRL '05, Paper #3, below), and then concentrated on pulsed measurements and quantum control of the qubit. We were able to measure the fidelity of single-shot readouts for cQED measurement, perform Rabi and Ramsey experiments to obtain record values for coherence and excited state lifetimes of a superconducting qubit, perform the first high-fidelity control of the quantum state of a superconducting qubit as indicated by a visibility of Rabi flops which approaches unity (Wallraff et. al. PRL '05; Paper #4 below), and begin experiments on two remote qubits coupled via a single cavity.

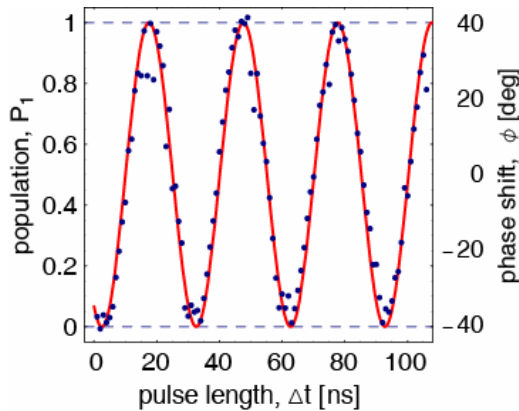


Figure 2: Rabi oscillations of a Cooper-pair box qubit in cQED architecture, using the cavity as a QND measurement of the qubit. The right axis shows the phase shift of the transmission thru the cavity, which can be directly converted into a qubit population in the excited state. Blue points are the data, and the red line is a sinusoidal oscillation (at the Rabi frequency) with unit amplitude. The data are consistent with a visibility of  $95\% \pm 5\%$ , marking the first demonstration of truly high-fidelity. Note that there is no noticeable decay in the oscillation amplitude, consistent with the coherence time  $T_2 = 500$  nanoseconds measured in a Ramsey expt. (not shown).

The results of some of the time domain measurements on the qubit are shown in Figure 2. The advantage of the cQED measurement technique is that the interaction of qubit and measurement can be understood and tested in quantitative detail. In particular, our work on steady-state spectroscopy and backaction published in Paper 2 verify that we understand precisely how to convert the measured experimental quantity, the transmission phase shift through the cavity, directly into an excited state population of the qubit. This allows us to convert our measured Rabi oscillations into a quantitative qubit population, and to extract a precise measurement, for the first time, of the visibility of Rabi oscillations for a superconducting qubit. As seen in Figure 2, the Rabi oscillations are consistent with unit visibility, indicating that our qubit is not interacting strongly with spurious degrees of freedom in its environment, perhaps because it is protected by the cavity and the dispersive measurement which does not heat or excite quasiparticles or other modes. Using a pulsed measurement and two  $\text{Pi}/2$  pulses on the qubit (i.e. a three-pulse experiment) we performed Ramsey experiments to measure the true coherence time of the qubit to be about 0.5 microseconds, essentially equaling the previous record achieved by Devoret and co-workers at Saclay. We also measured a relaxation ( $T_1$ ) time of the qubit of approximately 7 microseconds, which is also a record high value for such qubits, and again encouraging for future work.

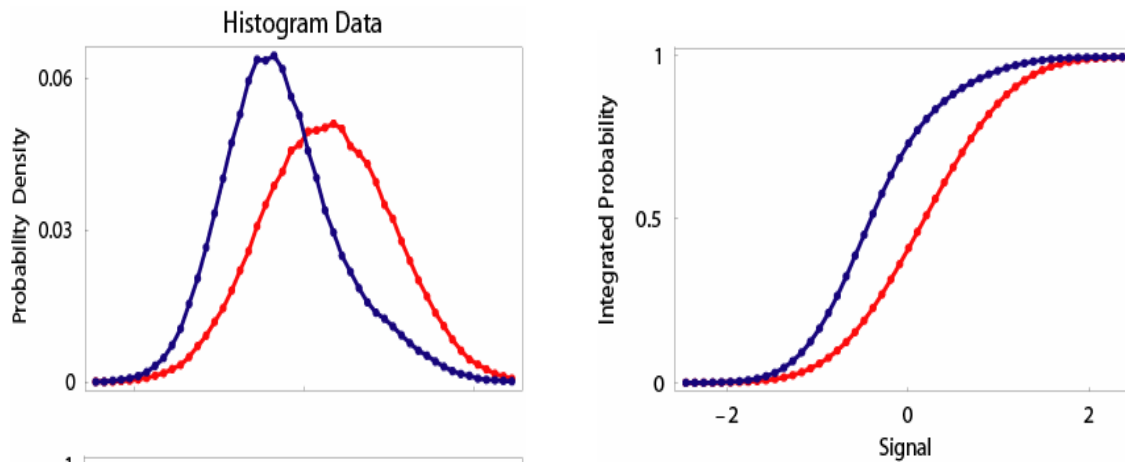


Figure 3: Fidelity of single-shot QND measurements of a qubit with the cavity. Left panel shows histogram of approximately  $10^7$  individual shots (about 5 minutes of data total) for measuring the qubit in the ground state (blue) or following a single Pi pulse to create the excited state (red). The probability (vertical axis) of obtaining a particular measurement value is plotted versus the total signal (horizontal axis, in arbitrary units). The right panel shows the integrated probabilities for ground (blue) and excited state (red) as a function of the same signal. Around a threshold value of zero signal, the curves are separated by 30-40%, which indicates the fidelity for performing a single-shot measurement.

We have also studied the fidelity of single-shot measurements with the cQED dispersive measurement, as shown in Figure 3. This works well, and the measurement and data collection are rapid, making studies of qubit or readout behavior very efficient. The signal to noise is limited by a combination of the finite measurement time for a given shot (i.e. the  $T_1$  relaxation time of the qubit), the strength of the measurement probe signal (here about  $10^{-16}$  Watts, corresponding to populating the cavity with about 10 photons at the 5 GHz cavity frequency), and the amplifier noise. The measured fidelity is about 30-40%, consistent with the expectations for these settings, but it should be possible to significantly improve this number either with increased qubit lifetime, lower amplifier noise, or stronger measurement signals. We have also undertaken a theoretical study of the measurement process and the readout fidelity (Braff et. al., in preparation; Paper 5), which explains both the observed histograms and the fidelity. This work was done by a Yale undergraduate, William Braff, as part of his senior thesis, and will be submitted to Phys. Rev. A.

Building on these results with the cavity QED architecture for the Cooper-pair box, we have begun experiments with two qubits coupled and readout via a single microwave cavity. A micrograph of such a sample is shown in Figure 4 below. Relatively simple measurements (see left grayscale plot) show the presence of the two qubits. By employing two gates and unequal SQUID loop areas for the qubits, the individual qubit properties can be found, and their energies can be controlled independently. This data also indicates that each qubit can be strongly coupled to the cavity mode. Using various RF methods (described in the theory section below), the coupling between the qubits via resonant or virtual exchange of a cavity photon could then be used to experiment with two-qubit gates.

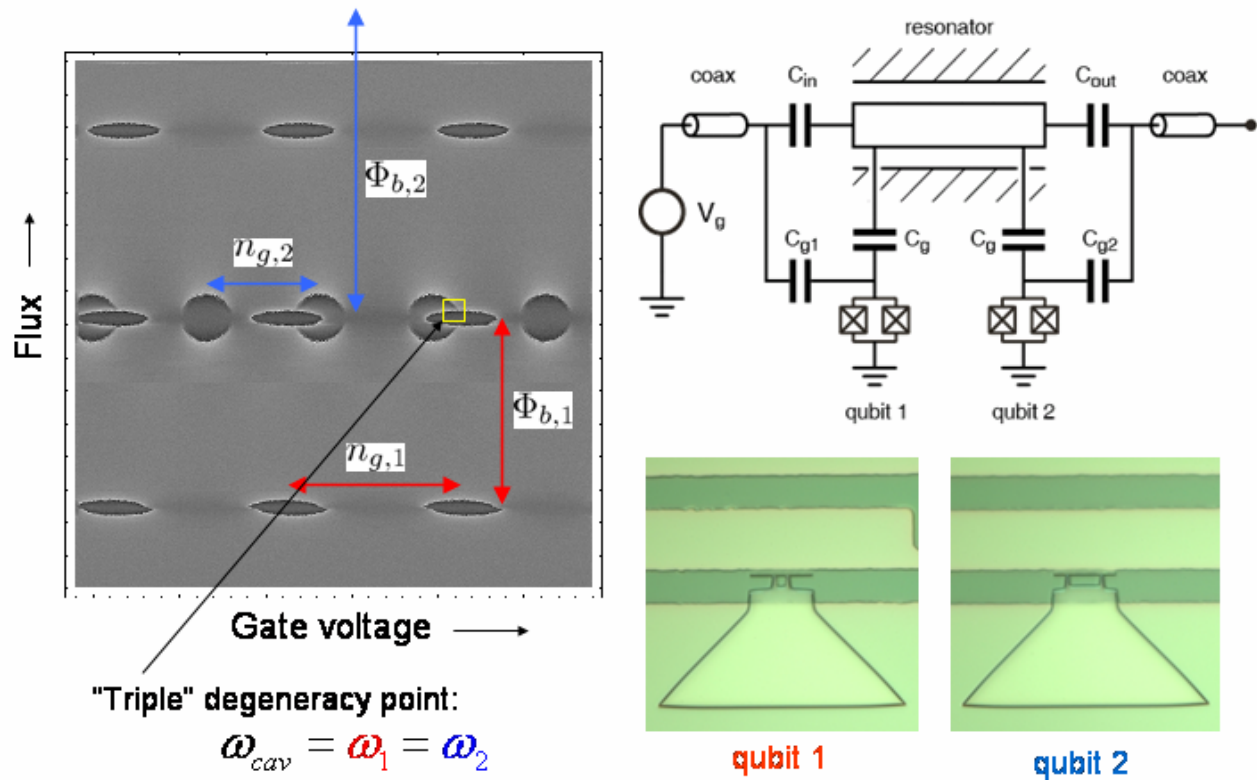


Figure 4: First experiments with two coupled qubits in a cavity. The schematic of the experiment is shown in the upper right. Two Cooper-pair box qubits are placed within a superconducting transmission-line resonant cavity, near the opposite ends, approximately 2 centimeters apart from one another. Gate voltages applied to the input and output ports of the resonator, respectively, control the gate charge of the two qubits independently. The qubits are fabricated with SQUID loops of different sizes (see optical micrographs in lower right), so that applying a global magnetic field tunes the Josephson energies, and thus the transition frequencies, of the two qubits with different periodicities. Measurements on this system are shown on the left. The gray scale indicates the phase shift through the cavity, which exhibits a sharp jump (boundaries of the dark ellipses) when one or the other of the qubits is tuned into resonance with the cavity. The figure shows tuning of the qubits with magnetic field (vertical axis) and one of the two gate voltages (horizontal). This type of figure allows both the determination of the Josephson and charging energies of the two qubits, and a determination of the setting which match qubit frequencies. An arrow indicates a point where both qubits may be tuned through resonance with the cavity (a triple degeneracy), where the qubits should be coupled to one another and entanglement and two-qubit gates should be possible. Further experiments are in progress, including time-domain control of the individual qubits in this system.

**Publications submitted or appearing during this period:**

(copies of these papers are attached following this page)

- 1) “*Cavity Quantum Electrodynamics for Superconducting Electrical Circuits: an Architecture for Quantum Computation,*” Alexandre Blais, Ren-Shou Huang, Andreas Wallraff, S.M. Girvin, and R.J. Schoelkopf, Phys. Rev. A **69**, 062320 (2004).
- 2) “*Coherent Coupling of a Single Photon to a Superconducting Qubit Using Circuit Quantum Electrodynamics,*” A. Wallraff, D. Schuster, Alexandre Blais, L. Frunzio, Ren-Shou Huang, J. Majer, S. Kumar, S.M. Girvin, and R.J. Schoelkopf, Nature **431**, 162 (2004).
- 3) “*AC Stark Shift and Dephasing in a Superconducting Qubit Strongly Coupled to a Cavity Field,*” D.I. Schuster, A. Wallraff, Alexandre Blais, L. Frunzio, Ren-Shou Huang, J. Majer, S.M. Girvin, and R.J. Schoelkopf, Phys. Rev. Lett. **94**, 123602 (2005).
- 4) “*Fabrication and Characterization of Superconducting Circuit QED Devices for Quantum Computation,*” L. Frunzio, A. Wallraff, D. Schuster, J. Majer, and R.J. Schoelkopf, IEEE Trans. on Applied Superconductivity **15**, 860 (2005).
- 5) “*Approaching Unit Visibility for Control of a Superconducting Qubit with Dispersive Readout,*” A. Wallraff, D.I. Schuster, A. Blais, L. Frunzio, J. Majer, M.H. Devoret, S.M. Girvin, and R.J. Schoelkopf, Phys. Rev. Lett. **95**, 060501 (2005).

**MASTER COPY:** PLEASE KEEP THIS "MEMORANDUM OF TRANSMITTAL" BLANK FOR REPRODUCTION PURPOSES. WHEN REPORTS ARE GENERATED UNDER THE ARO SPONSORSHIP, FORWARD A COMPLETED COPY OF THIS FORM WITH EACH REPORT SHIPMENT TO THE ARO. THIS WILL ASSURE PROPER IDENTIFICATION. NOT TO BE USED FOR INTERIM PROGRESS REPORTS; SEE PAGE 2 FOR INTERIM PROGRESS REPORT INSTRUCTIONS.

**MEMORANDUM OF TRANSMITTAL**

U.S. Army Research Office  
ATTN: AMSRL-RO-BI (TR)  
P.O. Box 12211  
Research Triangle Park, NC 27709-2211

Reprint (Orig + 2 copies)

Technical Report (Orig + 2 copies)

Manuscript (1 copy)

Final Progress Report (Orig + 2 copies)

Related Materials, Abstracts, Theses (1 copy)

CONTRACT/GRANT NUMBER:

REPORT TITLE:

is forwarded for your information.

SUBMITTED FOR PUBLICATION TO (applicable only if report is manuscript):

Sincerely,

Robert J. Schoelkopf

# Cavity quantum electrodynamics for superconducting electrical circuits: an architecture for quantum computation

Alexandre Blais,<sup>1</sup> Ren-Shou Huang,<sup>1,2</sup> Andreas Wallraff,<sup>1</sup> S. M. Girvin,<sup>1</sup> and R. J. Schoelkopf<sup>1</sup>

<sup>1</sup>*Departments of Physics and Applied Physics, Yale University, New Haven, CT 06520*

<sup>2</sup>*Department of Physics, Indiana University, Bloomington, IN 47405*

(Dated: March 28, 2004)

We propose a realizable architecture using one-dimensional transmission line resonators to reach the strong coupling limit of cavity quantum electrodynamics in superconducting electrical circuits. The vacuum Rabi frequency for the coupling of cavity photons to quantized excitations of an adjacent electrical circuit (qubit) can easily exceed the damping rates of both the cavity and the qubit. This architecture is attractive both as a macroscopic analog of atomic physics experiments and for quantum computing and control, since it provides strong inhibition of spontaneous emission, potentially leading to greatly enhanced qubit lifetimes, allows high-fidelity quantum non-demolition measurements of the state of multiple qubits, and has a natural mechanism for entanglement of qubits separated by centimeter distances. In addition it would allow production of microwave photon states of fundamental importance for quantum communication.

PACS numbers: 03.67.Lx, 73.23.Hk, 74.50.+r, 32.80.-t

## I. INTRODUCTION

Cavity quantum electrodynamics (cQED) studies the properties of atoms coupled to discrete photon modes in high  $Q$  cavities. Such systems are of great interest in the study of the fundamental quantum mechanics of open systems, the engineering of quantum states and the study of measurement-induced decoherence [1–3], and have also been proposed as possible candidates for use in quantum information processing and transmission [1–3]. Ideas for novel cQED analogs using nano-mechanical resonators have recently been suggested by Schwab and collaborators [4, 5]. We present here a realistic proposal for cQED via Cooper pair boxes coupled to a one-dimensional (1D) transmission line resonator, within a simple circuit that can be fabricated on a single microelectronic chip. As we discuss, 1D cavities offer a number of practical advantages in reaching the strong coupling limit of cQED over previous proposals using discrete LC circuits [6, 7], large Josephson junctions [8–10], or 3D cavities [11–13]. Besides the potential for entangling qubits to realize two-qubit gates addressed in those works, in the present work we show that the cQED approach also gives strong and controllable isolation of the qubits from the electromagnetic environment, permits high fidelity quantum non-demolition (QND) readout of multiple qubits, and can produce states of microwave photon fields suitable for quantum communication. The proposed circuits therefore provide a simple and efficient architecture for solid-state quantum computation, in addition to opening up a new avenue for the study of entanglement and quantum measurement physics with macroscopic objects. We will frame our discussion in a way that makes contact between the language of atomic physics and that of electrical engineering.

We begin in Sec. II with a brief general overview of cQED before turning to a discussion of our proposed

solid-state realization of cavity QED in Sec. III. We then discuss in Sec. IV the case where the cavity and the qubit are tuned in resonance and in Sec. V the case of large detuning which leads to lifetime enhancement of the qubit. In Sec. VI, a quantum non-demolition read-out protocol is presented. Realization of one-qubit logical operations is discussed in Sec. VII and two-qubit entanglement in Sec. VIII. We show in Sec. IX how to take advantage of encoded universality and decoherence-free subspace in this system.

## II. BRIEF REVIEW OF CAVITY QED

Cavity QED studies the interaction between atoms and the quantized electromagnetic modes inside a cavity. In the optical version of cQED [2], schematically shown in Fig. 1(a), one drives the cavity with a laser and monitors changes in the cavity transmission resulting from coupling to atoms falling through the cavity. One can also monitor the spontaneous emission of the atoms into transverse modes not confined by the cavity. It is not generally possible to directly determine the state of the atoms after they have passed through the cavity because the spontaneous emission lifetime is on the scale of nanoseconds. One can, however, infer information about the state of the atoms inside the cavity from real-time monitoring of the cavity optical transmission.

In the microwave version of cQED [3], one uses a very high  $Q$  superconducting 3D resonator to couple photons to transitions in Rydberg atoms. Here one does not directly monitor the state of the photons, but is able to determine with high efficiency the state of the atoms after they have passed through the cavity (since the excited state lifetime is of order 30 ms). From this state-selective detection one can infer information about the state of the photons in the cavity.

The key parameters describing a cQED system (see

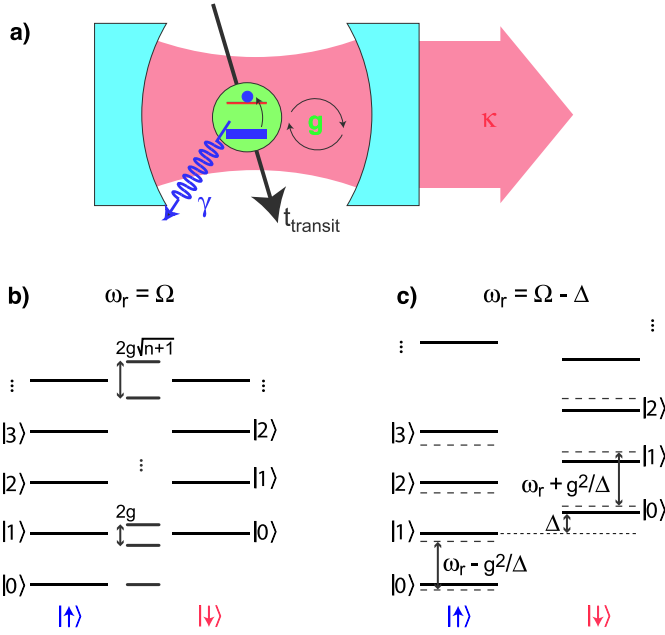


FIG. 1: (color online). a) Standard representation of cavity quantum electrodynamic system, comprising a single mode of the electromagnetic field in a cavity with decay rate  $\kappa$  coupled with a coupling strength  $g = \mathcal{E}_{\text{rms}}d/\hbar$  to a two-level system with spontaneous decay rate  $\gamma$  and cavity transit time  $t_{\text{transit}}$ . b) Energy spectrum of the uncoupled (left and right) and dressed (center) atom-photon states in the case of zero detuning. The degeneracy of the two-dimensional manifolds of states with  $n - 1$  quanta is lifted by  $2g\sqrt{n+1}$ . c) Energy spectrum in the dispersive regime (long dash lines). To second order in  $g$ , the level separation is independent of  $n$ , but depends on the state of the atom.

Table I) are the cavity resonance frequency  $\omega_r$ , the atomic transition frequency  $\Omega$ , and the strength of the atom-photon coupling  $g$  appearing in the Jaynes-Cummings Hamiltonian [14]

$$H = \hbar\omega_r \left( a^\dagger a + \frac{1}{2} \right) + \frac{\hbar\Omega}{2} \sigma^z + \hbar g (a^\dagger \sigma^- + \sigma^+ a) + H_\kappa + H_\gamma. \quad (1)$$

Here  $H_\kappa$  describes the coupling of the cavity to the continuum which produces the cavity decay rate  $\kappa = \omega_r/Q$ , while  $H_\gamma$  describes the coupling of the atom to modes other than the cavity mode which cause the excited state to decay at rate  $\gamma$  (and possibly also produce additional dephasing effects). An additional important parameter in the atomic case is the transit time  $t_{\text{transit}}$  of the atom through the cavity.

In the absence of damping, exact diagonalization of the Jaynes-Cumming Hamiltonian yields the excited eigenstates (dressed states) [15]

$$|+, n\rangle = \cos \theta_n |\downarrow, n\rangle + \sin \theta_n |\uparrow, n+1\rangle \quad (2)$$

$$|-, n\rangle = -\sin \theta_n |\downarrow, n\rangle + \cos \theta_n |\uparrow, n+1\rangle \quad (3)$$

and ground state  $|\uparrow, 0\rangle$  with corresponding eigenenergies

$$E_{\pm, n} = (n+1)\hbar\omega_r \pm \frac{\hbar}{2} \sqrt{4g^2(n+1) + \Delta^2} \quad (4)$$

$$E_{\uparrow, 0} = -\frac{\hbar\Delta}{2}. \quad (5)$$

In these expressions,

$$\theta_n = \frac{1}{2} \tan^{-1} \left( \frac{2g\sqrt{n+1}}{\Delta} \right), \quad (6)$$

and  $\Delta \equiv \Omega - \omega_r$  the atom-cavity detuning.

Figure 1b) shows the spectrum of these dressed-states for the case of zero detuning,  $\Delta = 0$ , between the atom and the cavity. In this situation, degeneracy of the pair of states with  $n$  quanta is lifted by  $2g\sqrt{n+1}$  due to the atom-photon interaction. In the manifold with a single excitation, Eqs. (2) and (3) reduce to the maximally entangled atom-field states  $|\pm, 0\rangle = (|\uparrow, 1\rangle \pm |\downarrow, 0\rangle)/\sqrt{2}$ . An initial zero-photon excited atom state  $|\uparrow, 0\rangle$  will therefore flop into a photon  $|\downarrow, 1\rangle$  and back again at the vacuum Rabi frequency  $g/\pi$ . Since the excitation is half atom and half photon, the decay rate of  $|\pm, 0\rangle$  is  $(\kappa + \gamma)/2$ . The pair of states  $|\pm, 0\rangle$  will be resolved in a transmission experiment if the splitting  $2g$  is larger than this linewidth. The value of  $g = \mathcal{E}_{\text{rms}}d/\hbar$  is determined by the transition dipole moment  $d$  and the rms zero-point electric field of the cavity mode. Strong coupling is achieved when  $g \gg \kappa, \gamma$  [15].

For large detuning,  $g/\Delta \ll 1$ , expansion of Eq. (4) yields the dispersive spectrum shown in Fig. 1c). In this situation, the eigenstates of the one excitation manifold take the form [15]

$$|-, 0\rangle \sim -(g/\Delta) |\downarrow, 0\rangle + |\uparrow, 1\rangle \quad (7)$$

$$|+, 0\rangle \sim |\downarrow, 0\rangle + (g/\Delta) |\uparrow, 1\rangle. \quad (8)$$

The corresponding decays rates are then simply given by

$$\Gamma_{-, 0} \simeq (g/\Delta)^2 \gamma + \kappa \quad (9)$$

$$\Gamma_{+, 0} \simeq \gamma + (g/\Delta)^2 \kappa. \quad (10)$$

More insight into the dispersive regime is gained by making the unitary transformation

$$U = \exp \left[ \frac{g}{\Delta} (a\sigma^+ - a^\dagger\sigma^-) \right] \quad (11)$$

and expanding to second order in  $g$  (neglecting damping for the moment) to obtain

$$UHU^\dagger \approx \hbar \left[ \omega_r + \frac{g^2}{\Delta} \sigma^z \right] a^\dagger a + \frac{\hbar}{2} \left[ \Omega + \frac{g^2}{\Delta} \right] \sigma^z. \quad (12)$$

As is clear from this expression, the atom transition is ac-Stark/Lamb shifted by  $(g^2/\Delta)(n+1/2)$ . Alternatively, one can interpret the ac-Stark shift as a dispersive shift of the cavity transition by  $\sigma_z g^2/\Delta$ . In other words, the atom pulls the cavity frequency by  $\pm g^2/\kappa\Delta$ .

parameter	symbol	3D optical	3D microwave	1D circuit
resonance/transition frequency	$\omega_r/2\pi, \Omega/2\pi$	350 THz	51 GHz	10 GHz
vacuum Rabi frequency	$g/\pi, g/\omega_r$	220 MHz, $3 \times 10^{-7}$	47 kHz, $1 \times 10^{-7}$	100 MHz, $5 \times 10^{-3}$
transition dipole	$d/ea_0$	$\sim 1$	$1 \times 10^3$	$2 \times 10^4$
cavity lifetime	$1/\kappa, Q$	10 ns, $3 \times 10^7$	1 ms, $3 \times 10^8$	160 ns, $10^4$
atom lifetime	$1/\gamma$	61 ns	30 ms	$2 \mu\text{s}$
atom transit time	$t_{\text{transit}}$	$\geq 50 \mu\text{s}$	$100 \mu\text{s}$	$\infty$
critical atom number	$N_0 = 2\gamma\kappa/g^2$	$6 \times 10^{-3}$	$3 \times 10^{-6}$	$\leq 6 \times 10^{-5}$
critical photon number	$m_0 = \gamma^2/2g^2$	$3 \times 10^{-4}$	$3 \times 10^{-8}$	$\leq 1 \times 10^{-6}$
# of vacuum Rabi flops	$n_{\text{Rabi}} = 2g/(\kappa + \gamma)$	$\sim 10$	$\sim 5$	$\sim 10^2$

TABLE I: Key rates and cQED parameters for optical [2] and microwave [3] atomic systems using 3D cavities, compared against the proposed approach using superconducting circuits, showing the possibility for attaining the strong cavity QED limit ( $n_{\text{Rabi}} \gg 1$ ). For the 1D superconducting system, a full-wave ( $L = \lambda$ ) resonator,  $\omega_r/2\pi = 10$  GHz, a relatively low  $Q$  of  $10^4$  and coupling  $\beta = C_g/C_\Sigma = 0.1$  are assumed. For the 3D microwave case, the number of Rabi flops is limited by the transit time. For the 1D circuit case, the intrinsic Cooper-pair box decay rate is unknown; a conservative value equal to the current experimental upper bound  $\gamma \leq 1/(2 \mu\text{s})$  is assumed.

### III. CIRCUIT IMPLEMENTATION OF CAVITY QED

We now consider the proposed realization of cavity QED using superconducting circuits shown in Fig. 2. A 1D transmission line resonator consisting of a full-wave section of superconducting coplanar waveguide plays the role of the cavity and a superconducting qubit plays the role of the atom. A number of superconducting quantum circuits could function as artificial atom, but for definiteness we focus here on the Cooper pair box [6, 16–18].

#### A. Cavity: coplanar stripline resonator

An important advantage of this approach is that the zero-point energy is distributed over a very small effective volume ( $\approx 10^{-5}$  cubic wavelengths) for our choice of a quasi-one-dimensional transmission line ‘cavity.’ As shown in appendix A, this leads to significant rms voltages  $V_{\text{rms}}^0 \sim \sqrt{\hbar\omega_r/cL}$  between the center conductor and the adjacent ground plane at the antinodal positions, where  $L$  is the resonator length and  $c$  is the capacitance per unit length of the transmission line. At a resonant frequency of 10 GHz ( $h\nu/k_B \sim 0.5$  K) and for a  $10 \mu\text{m}$  gap between the center conductor and the adjacent ground plane,  $V_{\text{rms}} \sim 2 \mu\text{V}$  corresponding to electric fields  $\mathcal{E}_{\text{rms}} \sim 0.2$  V/m, some 100 times larger than achieved in the 3D cavity described in Ref. [3]. Thus, this geometry might also be useful for coupling to Rydberg atoms [19].

In addition to the small effective volume, and the fact that the on-chip realization of cQED shown in Fig. 2 can be fabricated with existing lithographic techniques, a transmission-line resonator geometry offers other practical advantages over lumped LC circuits or current-biased large Josephson junctions. The qubit can be placed within the cavity formed by the transmission line to

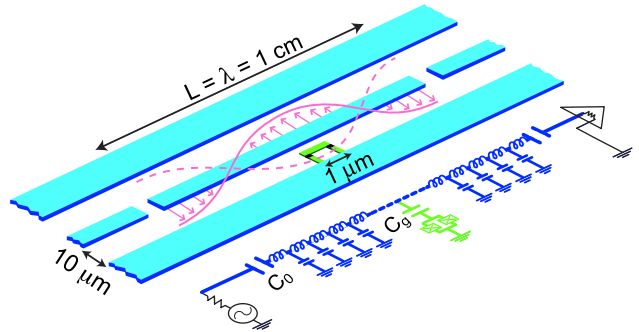


FIG. 2: (color online). Schematic layout and equivalent lumped circuit representation of proposed implementation of cavity QED using superconducting circuits. The 1D transmission line resonator consists of a full-wave section of superconducting coplanar waveguide, which may be lithographically fabricated using conventional optical lithography. A Cooper pair box qubit is placed between the superconducting lines, and is capacitively coupled to the center trace at a maximum of the voltage standing wave, yielding a strong electric dipole interaction between the qubit and a single photon in the cavity. The box consists of two small ( $\sim 100 \text{ nm} \times 100 \text{ nm}$ ) Josephson junctions, configured in a  $\sim 1 \mu\text{m}$  loop to permit tuning of the effective Josephson energy by an external flux  $\Phi_{\text{ext}}$ . Input and output signals are coupled to the resonator, via the capacitive gaps in the center line, from  $50 \Omega$  transmission lines which allow measurements of the amplitude and phase of the cavity transmission, and the introduction of dc and rf pulses to manipulate the qubit states. Multiple qubits (not shown) can be similarly placed at different antinodes of the standing wave to generate entanglement and two-bit quantum gates across distances of several millimeters.

strongly suppress the spontaneous emission, in contrast to a lumped LC circuit, where without additional special filtering, radiation and parasitic resonances may be induced in the wiring [20]. Since the resonant frequency of the transmission line is determined primarily by a fixed

geometry, its reproducibility and immunity to  $1/f$  noise should be superior to Josephson junction plasma oscillators. Finally, transmission line resonances in coplanar waveguides with  $Q \sim 10^6$  have already been demonstrated [21, 22], suggesting that the internal losses can be very low. The optimal choice of the resonator  $Q$  in this approach is strongly dependent on the intrinsic decay rates of superconducting qubits which as described below, are presently unknown, but can be determined with the setup proposed here. Here we assume the conservative case of an overcoupled resonator with a  $Q \sim 10^4$ , which is preferable for the first experiments.

### B. Artificial atom: the Cooper pair box

Our choice of ‘atom’, the Cooper pair box [6, 16] is a mesoscopic superconducting island. As shown in Fig. 3, the island is connected to a large reservoir through a Josephson junction with Josephson energy  $E_J$  and capacitance  $C_J$ . It is voltage biased from a lead having capacitance  $C_g$  to the island. If the superconducting gap is larger than both the charging energy  $E_c = e^2/2C_\Sigma$  (where  $C_\Sigma = C_J + C_g$  is the total box capacitance) and temperature, the only relevant degree of freedom is the number of Cooper pairs  $N$  on the island. In this basis, the Hamiltonian describing the superconducting island takes the form

$$H_Q = 4E_c \sum_N (N - N_g)^2 |N\rangle \langle N| - \frac{E_J}{2} \sum_N (|N+1\rangle \langle N| + h.c.), \quad (13)$$

where  $N_g = C_g V_g / 2e$  is the dimensionless gate charge representing the total polarization charge injected into the island by the voltage source.

In the charge regime,  $4E_c \gg E_J$ , and restricting the gate charge to the range  $N_g \in [0, 1]$ , only a pair of adjacent charge states on the island are relevant and the

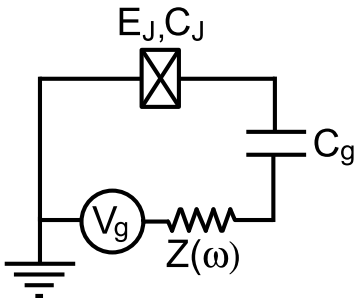


FIG. 3: Circuit diagram of the Cooper pair box. The gate voltage is connected to the island through an environmental impedance  $Z(\omega)$ .

Hamiltonian then reduces to a  $2 \times 2$  matrix

$$H_Q = -\frac{E_{el}}{2} \bar{\sigma}^z - \frac{E_J}{2} \bar{\sigma}^x, \quad (14)$$

with  $E_{el} = 4E_c(1 - 2N_g)$ . The Cooper pair box can in this case be mapped to a pseudo spin-1/2 particle, with effective fields in the  $x$  and  $z$  directions.

Replacing the Josephson junction by a pair of junctions in parallel, each with energy  $E_J/2$ , the effective field in the  $x$  direction becomes  $E_J \cos(\pi \Phi_{ext}/\Phi_0)/2$ . By threading a flux  $\Phi_{ext}$  in the loop formed by the pair of junctions and changing the gate voltage  $V_g$ , it is possible to control the effective field acting on the qubit. In the setup of Fig. 2, application of dc gate voltage on the island can be conveniently achieved by applying a bias voltage to the center conductor of the transmission line. The resonator coupling capacitance  $C_0$ , the gate capacitance  $C_g$  (the capacitance between the center conductor of the resonator and the island) and the capacitance to ground of the resonator then act as a voltage divider.

### C. Combined system: superconducting cavity QED

For a superconducting island fabricated inside a resonator, in addition to a dc part  $V_g^{dc}$ , the gate voltage has a quantum part  $v$ . As shown in appendix A, if the qubit is placed in the center of the resonator, this latter contribution is given by  $v = V_{rms}^0(a^\dagger + a)$ . Taking into account both  $V_g^{dc}$  and  $v$  in (14), we obtain

$$H_Q = -2E_c(1 - 2N_g^{dc}) \bar{\sigma}^z - \frac{E_J}{2} \bar{\sigma}^x - e \frac{C_g}{C_\Sigma} \sqrt{\frac{\hbar \omega_r}{Lc}} (a^\dagger + a)(1 - 2N_g - \bar{\sigma}^z). \quad (15)$$

Working in the eigenbasis  $\{|\uparrow\rangle, |\downarrow\rangle\}$  of the first two terms of the above expression [23], and adding the Hamiltonian of the oscillator mode coupled to the qubit, the Hamiltonian of the interacting qubit and resonator system takes the form

$$H = \hbar \omega_r \left( a^\dagger a + \frac{1}{2} \right) + \frac{\hbar \Omega}{2} \sigma^z - e \frac{C_g}{C_\Sigma} \sqrt{\frac{\hbar \omega_r}{Lc}} (a^\dagger + a)(1 - 2N_g - \cos(\theta) \sigma^z + \sin(\theta) \sigma^x). \quad (16)$$

Here,  $\sigma^x$  and  $\sigma^z$  are Pauli matrices in the eigenbasis  $\{|\uparrow\rangle, |\downarrow\rangle\}$ ,  $\theta = \arctan[E_J/4E_c(1 - 2N_g^{dc})]$  is the mixing angle and the energy splitting of the qubit is  $\Omega = \sqrt{E_J^2 + [4E_c(1 - 2N_g^{dc})]^2}/\hbar$  [23]. Note that contrary to the case of a qubit fabricated outside the cavity where the  $N_g^2$  term in (13) has no effect, here this term slightly renormalize the cavity frequency  $\omega_r$  and displaces the oscillator coordinate. These effects are implicit in Eq. (16).

At the charge degeneracy point (where  $N_g = C_g V_g^{dc}/2e = 1/2$  and  $\theta = \pi/2$ ), neglecting rapidly oscillating terms and omitting damping for the moment,

Eq. (16) reduces to the Jaynes-Cummings Hamiltonian (1) with  $\Omega = E_J/\hbar$  and the vacuum Rabi frequency

$$g = \frac{\beta e}{\hbar} \sqrt{\frac{\hbar \omega_r}{cL}}, \quad (17)$$

where  $\beta \equiv C_g/C_\Sigma$ . The quantum electrical circuit of Fig. 2 is therefore mapped to the problem of a two-level atom inside a cavity. Away from the degeneracy point, this mapping can still be performed, but with a coupling strength reduced by  $\sin \theta$  and an additional term proportional to  $(a^\dagger + a)$ .

In this circuit, the ‘atom’ is highly polarizable at the charge degeneracy point, having transition dipole moment  $d \equiv \hbar g/\mathcal{E}_{\text{rms}} \sim 2 \times 10^4$  atomic units ( $ea_0$ ), or more than an order of magnitude larger than even a typical Rydberg atom [15]. An experimentally realistic [18] coupling  $\beta \sim 0.1$  leads to a vacuum Rabi rate  $g/\pi \sim 100$  MHz, which is three orders of magnitude larger than in corresponding atomic microwave cQED experiments [3], or approximately 1% of the transition frequency. Unlike the usual cQED case, these artificial ‘atoms’ remain at fixed positions indefinitely and so do not suffer from the problem that the coupling  $g$  varies with position in the cavity.

A comparison of the experimental parameters for implementations of cavity QED with optical and microwave atomic systems and for the proposed implementation with superconducting circuits is presented in Table I. We assume here a relatively low  $Q = 10^4$  and a worst case estimate, consistent with the bound set by previous experiments with superconducting qubits (discussed further below), for the intrinsic qubit lifetime of  $1/\gamma \geq 2 \mu\text{s}$ .

The standard figures of merit [24] for strong coupling are the critical photon number needed to saturate the atom on resonance  $m_0 = \gamma^2/2g^2 \leq 1 \times 10^{-6}$  and the minimum atom number detectable by measurement of the cavity output  $N_0 = 2\gamma\kappa/g^2 \leq 6 \times 10^{-5}$ . These remarkably low values are clearly very favorable, and show that superconducting circuits could access the interesting regime of very strong coupling.

#### IV. ZERO DETUNING

In the case of a low  $Q$  cavity ( $g < \kappa$ ) and zero detuning, the radiative decay rate of the qubit into the transmission line becomes strongly *enhanced* by a factor of  $Q$  relative to the rate in the absence of the cavity [15]. This is due to the resonant enhancement of the density of states at the atomic transition frequency. In electrical engineering language, the  $\sim 50 \Omega$  external transmission line impedance is transformed on resonance to a high value which is better matched to extract energy from the qubit.

For strong coupling  $g > \kappa, \gamma$ , the first excited state becomes a doublet with line width  $(\kappa + \gamma)/2$ , as explained in section II. As can be seen from Table I, the coupling

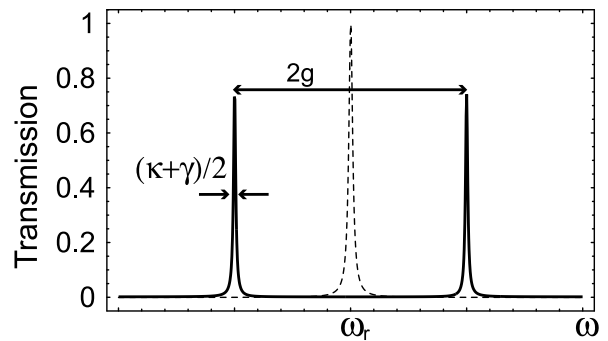


FIG. 4: Expected transmission spectrum of the resonator in the absence (broken line) and presence (full line) of a superconducting qubit biased at its degeneracy point. Parameters are those presented in Table I. The splitting exceeds the line width by two orders of magnitude.

in the proposed superconducting implementation is so strong that, even for the low  $Q = 10^4$  we have assumed,  $2g/(\kappa + \gamma) \sim 100$  vacuum Rabi oscillations are possible. Moreover, as shown in Fig. 4, the frequency splitting ( $g/\pi \sim 100$  MHz) will be readily resolvable in the transmission spectrum of the resonator. This spectrum, calculated here following Ref. [25], can be observed in the same manner as employed in optical atomic experiments, with a continuous wave measurement at low drive, and will be of practical use to find the dc gate voltage needed to tune the box into resonance with the cavity.

Of more fundamental importance than this simple avoided level crossing however, is the fact that the Rabi splitting scales with the square root of the photon number, making the level spacing anharmonic. This should cause a number of novel non-linear effects [14] to appear in the spectrum at higher drive powers when the average photon number in the cavity is large ( $\langle n \rangle > 1$ ).

A conservative estimate of the noise energy for a 10 GHz cryogenic high electron mobility (HEMT) amplifier is  $n_{\text{amp}} = k_B T_N/\hbar\omega \sim 100$  photons, where  $T_N$  is the noise temperature of the amplification circuit. As a result, these spectral features should be readily observable in a measurement time  $t_{\text{meas}} = 2n_{\text{amp}}/\langle n \rangle\kappa$ , or only  $\sim 32 \mu\text{s}$  for  $\langle n \rangle \sim 1$ .

#### V. LARGE DETUNING: LIFETIME ENHANCEMENT

For qubits *not* inside a cavity, fluctuation of the gate voltage acting on the qubit is an important source of relaxation and dephasing. As shown in Fig. 3, in practice the qubit’s gate is connected to the voltage source through external wiring having, at the typical microwave transition frequency of the qubit, a real impedance of value close to the impedance of free space ( $\sim 50 \Omega$ ). The relaxation rate expected from purely quantum fluctuations across this impedance (spontaneous emission)

is [18, 23]

$$\frac{1}{T_1} = \frac{E_j^2}{E_j^2 + E_{e1}^2} \left(\frac{e}{\hbar}\right)^2 \beta^2 S_V(+\Omega), \quad (18)$$

where  $S_V(+\Omega) = 2\hbar\Omega \text{Re}[Z(\Omega)]$  is the spectral density of voltage fluctuations across the environmental impedance (in the quantum limit). It is difficult in most experiments to precisely determine the real part of the high frequency environmental impedance presented by the leads connected to the qubit, but reasonable estimates [18] yield values of  $T_1$  in the range of  $1 \mu\text{s}$ .

For qubits fabricated inside a cavity, the noise across the environmental impedance does not couple directly to the qubit, but only indirectly through the cavity. For the case of strong detuning, coupling of the qubit to the continuum is therefore substantially reduced. One can view the effect of the detuned resonator as filtering out the vacuum noise at the qubit transition frequency or, in electrical engineering terms, as providing an impedance transformation which strongly *reduces* the real part of the environmental impedance seen by the qubit.

Solving for the normal modes of the resonator and transmission lines, including an input impedance  $R$  at each end of the resonator, the spectrum of voltage fluctuations as seen by the qubit fabricated in the center of the resonator can be shown to be well approximated by

$$S_V(\Omega) = \frac{2\hbar\omega_r}{Lc} \frac{\kappa/2}{\Delta^2 + (\kappa/2)^2}. \quad (19)$$

Using this transformed spectral density in (18) and assuming a large detuning between the cavity and the qubit, the relaxation rate due to vacuum fluctuations takes a form that reduces to  $1/T_1 \equiv \gamma_\kappa = (g/\Delta)^2 \kappa \sim 1/(64 \mu\text{s})$ , at the qubit's degeneracy point. This is the result already obtained in Eq. (10) using the dressed state picture for the coupled atom and cavity, except for the additional factor  $\gamma$  reflecting loss of energy to modes outside of the cavity. For large detuning, damping due to spontaneous emission can be much less than  $\kappa$ .

One of the important motivations for this cQED experiment is to determine the various contributions to the qubit decay rate so that we can understand their fundamental physical origins as well as engineer improvements. Besides  $\gamma_\kappa$  evaluated above, there are two additional contributions to the total damping rate  $\gamma = \gamma_\kappa + \gamma_\perp + \gamma_{\text{NR}}$ . Here  $\gamma_\perp$  is the decay rate into photon modes other than the cavity mode, and  $\gamma_{\text{NR}}$  is the rate of other (possibly non-radiative) decays. Optical cavities are relatively open and  $\gamma_\perp$  is significant, but for 1D microwave cavities,  $\gamma_\perp$  is expected to be negligible (despite the very large transition dipole). For Rydberg atoms the two qubit states are both highly excited levels and  $\gamma_{\text{NR}}$  represents (radiative) decay out of the two-level subspace. For Cooper pair boxes,  $\gamma_{\text{NR}}$  is completely unknown at the present time, but could have contributions from phonons, two-level systems in insulating [20] barriers and substrates, or thermally excited quasiparticles.

For Cooper box qubits *not* inside a cavity, recent experiments [18] have determined a relaxation time  $1/\gamma = T_1 \sim 1.3 \mu\text{s}$  despite the back action of continuous measurement by a SET electrometer. Vion et al. [17] found  $T_1 \sim 1.84 \mu\text{s}$  (without measurement back action) for their charge-phase qubit. Thus in these experiments, if there are non-radiative decay channels, they are at most comparable to the vacuum radiative decay rate (and may well be much less) estimated using Eq. (18). Experiments with a cavity will present the qubit with a simple and well controlled electromagnetic environment, in which the radiative lifetime can be enhanced with detuning to  $1/\gamma_\kappa > 64 \mu\text{s}$ , allowing  $\gamma_{\text{NR}}$  to dominate and yielding valuable information about any non-radiative processes.

## VI. DISPERSIVE QND READOUT OF QUBIT

In addition to lifetime enhancement, the dispersive regime is advantageous for read-out of the qubit. This can be realized by microwave irradiation of the cavity and then probing the transmitted or reflected photons [26].

### A. Measurement Protocol

A drive of frequency  $\omega_{\mu\text{w}}$  on the resonator can be modeled by [15]

$$H_{\mu\text{w}}(t) = \hbar\varepsilon(t)(a^\dagger e^{-i\omega_{\mu\text{w}}t} + a e^{+i\omega_{\mu\text{w}}t}), \quad (20)$$

where  $\varepsilon(t)$  is a measure of the drive the amplitude. In the dispersive limit, one expects from Fig. 1c) peaks in the transmission spectrum at  $\omega_r - g^2/\Delta$  and  $\Omega + 2g^2/\Delta$  if the qubit is initially in its ground state. In a frame rotating at the drive frequency, the matrix elements for these transitions are respectively

$$\begin{aligned} \langle \uparrow, 0 | H_{\mu\text{w}} | \overline{-}, \overline{n} \rangle &\sim \varepsilon \\ \langle \uparrow, 0 | H_{\mu\text{w}} | \overline{+}, \overline{n} \rangle &\sim \frac{\varepsilon g}{\Delta}. \end{aligned} \quad (21)$$

In the large detuning case, the peak at  $\Omega + 2g^2/\Delta$ , corresponding approximately to a qubit flip, is highly suppressed.

The matrix element corresponding to a qubit flip from the excited state is also suppressed and, as shown in Fig. 5, depending on the qubit being in its ground or excited states, the transmission spectrum will present a peak of width  $\kappa$  at  $\omega_r - g^2/\Delta$  or  $\omega_r + g^2/\Delta$ . With the parameters of Table I, this dispersive pull of the cavity frequency is  $\pm g^2/\kappa\Delta = \pm 2.5$  line widths for a 10% detuning. Exact diagonalization (4) shows that the pull is power dependent and decreases in magnitude for cavity photon numbers on the scale  $n = n_{\text{crit}} \equiv \Delta^2/4g^2$ . In the regime of non-linear response, single-atom optical bistability [14] can be expected when the drive frequency is off resonance at low power but on resonance at high power [29].

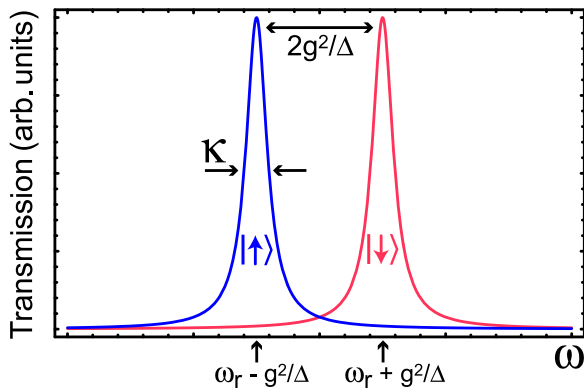


FIG. 5: (color online). Transmission spectrum of the cavity, which is “pulled” by an amount  $\pm g^2/\Delta = \pm 2.5\omega_r \times 10^{-4}$ , depending on the state of the qubit (red for the excited state, blue for the ground state). To perform a measurement of the qubit, a pulse of microwave photons, at a probe frequency  $\omega_{\mu w} = \omega_r$  or  $\omega_r \pm g^2/\Delta$  is sent through the cavity. Additional peaks near  $\Omega$  corresponding to qubit flips are suppressed by  $g/\Delta$ .

The state-dependent pull of the cavity frequency by the qubit can be used to entangle the state of the qubit with that of the photons transmitted or reflected by the resonator. For  $g^2/\kappa\Delta > 1$ , as in Fig. 5, the pull is greater than the line width and irradiating the cavity at one of the pulled frequencies  $\omega_r \pm g^2/\Delta$ , the transmission of the cavity will be close to unity for one state of the qubit and close to zero for the other [30].

Choosing the drive to be instead at the bare cavity frequency  $\omega_r$ , the state of the qubit is encoded in the phase of the reflected and transmitted microwaves. An initial qubit state  $|\chi\rangle = \alpha|\uparrow\rangle + \beta|\downarrow\rangle$  evolves under microwave irradiation into the entangled state  $|\psi\rangle = \alpha|\uparrow, \theta\rangle + \beta|\downarrow, -\theta\rangle$ , where  $\tan\theta = 2g^2/\kappa\Delta$ , and  $|\pm\theta\rangle$  are (interaction representation) coherent states with the appropriate mean photon number and opposite phases. In the situation where  $g^2/\kappa\Delta \ll 1$ , this is the most appropriate strategy.

It is interesting to note that such an entangled state can be used to couple qubits in distant resonators and allow quantum communication [31]. Moreover, if an independent measurement of the qubit state can be made, such states can be turned into photon Schrödinger cats [15].

To characterize these two measurement schemes corresponding to two different choices of the drive frequency, we compute the average photon number inside the resonator  $\bar{n}$  and the homodyne voltage on the 50Ω impedance at the output of the resonator. Since the power coupled to the outside of the resonator is  $P = \langle n \rangle \hbar\omega_r \kappa/2 = \langle V_{\text{out}} \rangle^2/R$ , the homodyne voltage can be expressed as  $\langle V_{\text{out}} \rangle = \sqrt{R\hbar\omega_r \kappa} \langle a + a^\dagger \rangle/2$  and is proportional to the real part of the field inside the cavity.

In the absence of dissipation, the time dependence of

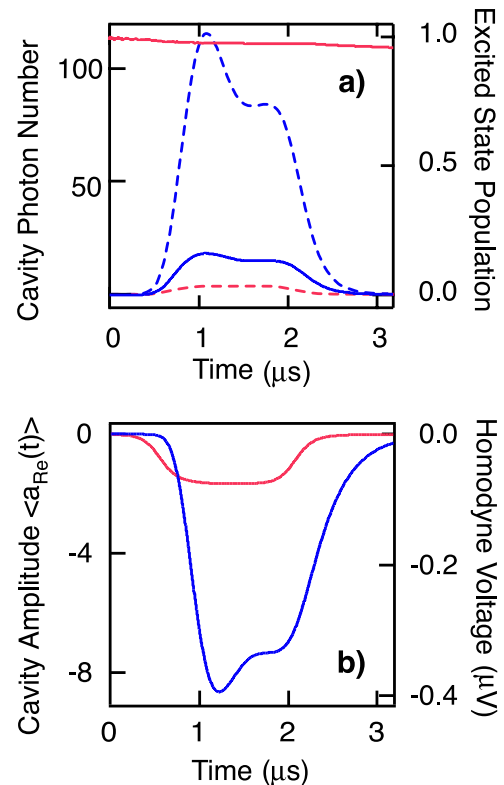


FIG. 6: (color online). Results of numerical simulations using the quantum state diffusion method. A microwave pulse of duration  $\sim 15/\kappa$  and centered at the pulled frequency  $\omega_r + g^2/\Delta$  drives the cavity. a) The occupation probability of the excited state (right axis, full lines), for the case in which the qubit is initially in the ground (blue) or excited (red) state and intracavity photon number (left axis, dash lines), are shown as a function of time. Though the qubit states are temporarily coherently mixed during the pulse, the probability of real transitions is seen to be small. Depending on the qubit’s state, the pulse is either on or away from the combined cavity-qubit resonance, and therefore is mostly transmitted or mostly reflected. b) The real component of the cavity electric field amplitude (left axis), and the transmitted voltage phasor (right axis) in the output transmission line, for the two possible initial qubit states. The parameters used for the simulation are presented in Table I.

the field inside the cavity can be obtained in the Heisenberg picture from Eqs. (12) and (20). This leads to a closed set of differential equations for  $a$ ,  $\sigma_z$  and  $a\sigma_z$  which is easily solved. In the presence of dissipation however (i.e. performing the transformation (11) on  $H_\kappa$  and  $H_\gamma$ , and adding the resulting terms to Eqs. (12) and (20)), the set is no longer closed and we resort to numerical stochastic wave function calculations [32]. See Appendix B for a brief presentation of this numerical method.

Figures 6 and 7 show the numerical results for the two choices of drive frequency and using the parameters of Table I. For these calculations, a pulse of duration  $\sim 15/\kappa$  with a hyperbolic tangent rise and fall, is used to excite the cavity. Fig. 6 corresponds to a drive at the

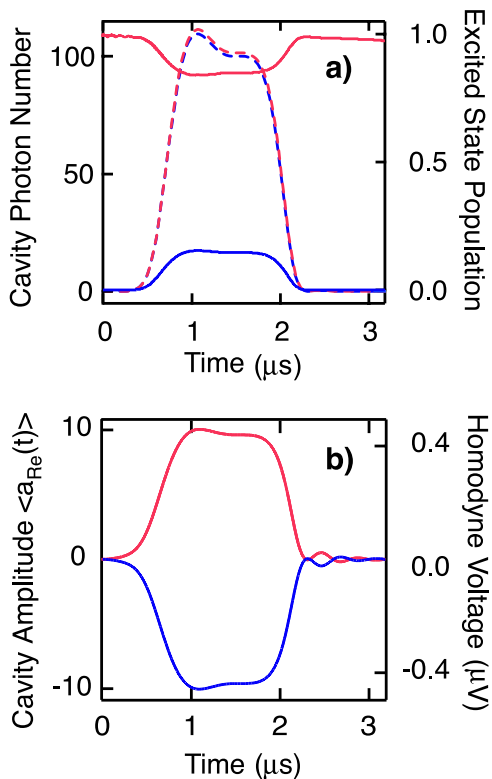


FIG. 7: (color online). Same as Fig. 6 for the drive at the bare cavity frequency  $\omega_r$ . Depending on the qubit's state, the pulse is either above or below the combined cavity-qubit resonance, and so is partly transmitted and reflected but with a large relative phase shift that can be detected with homodyne detection. In b), the opposing phase shifts cause a change in sign of the output, which can be measured with high signal-to-noise to realize a single-shot, QND measurement of the qubit.

pulled frequency  $\omega_r + g^2/\Delta$ . In Fig. 6a) the probability  $P_{\downarrow}$  to find the qubit in its excited state (right axis) is plotted as a function of time for the qubit initially in the ground (blue) or excited state (red). The dashed lines represent the corresponding number of photons in the cavity (left axis). Fig. 6b) shows, in a frame rotating at the drive frequency, the real part of the cavity electric field amplitude (left axis) and transmitted voltage phase (right axis) in the output transmission line, again for the two possible initial qubit states. These quantities are shown in Fig. 7 for a drive at the bare frequency  $\omega_r$ .

As expected, for the first choice of drive frequency, the information about the state of the qubit is mostly stored in the number of transmitted photons. When the drive is at the bare frequency however, there is very little information in the photon number, with most of the information being stored in the phase of the transmitted and reflected signal. This phase shift can be measured using standard heterodyne techniques. As also discussed in appendix C, both approaches can serve as a high efficiency quantum non-demolition dispersive readout of the

state of the qubit.

## B. Measurement Time and Backaction

As seen from Eq. (12), the back action of the dispersive cQED measurement is due to quantum fluctuations of the number of photons  $n$  within the cavity. These fluctuations cause variations in the ac Stark shift  $(g^2/\Delta)n\sigma^z$  that in turn dephase the qubit. It is useful to compute the corresponding dephasing rate and compare it with the measurement rate, i.e. the rate at which information about the state of the qubit can be acquired.

To determine the dephasing rate, we assume that the cavity is driven at the bare cavity resonance frequency and that the pull of the resonance is small compared to the line width  $\kappa$ . The relative phase accumulated between the ground and excited states of the qubit is

$$\varphi(t) = 2\frac{g^2}{\Delta} \int_0^t dt' n(t') \quad (22)$$

which yield a mean phase advance  $\langle \varphi \rangle = 2\theta_0 N$  with  $\theta_0 = 2g^2/\kappa\Delta$  and  $N = \kappa\bar{n}t/2$  the total number of transmitted photons [14]. For weak coupling, the dephasing time will greatly exceed  $1/\kappa$  and, in the long time limit, the noise in  $\varphi$  induced by the ac Stark shift will be gaussian. Dephasing can then be evaluated by computing the long time decay of the correlator

$$\begin{aligned} \langle \sigma^+(t)\sigma^-(0) \rangle &= \langle e^{i\int_0^t dt' \varphi(t')} \rangle \\ &\simeq e^{-\frac{1}{2}\left(2\frac{g^2}{\Delta}\right)^2 \int_0^t \int_0^t dt_1 dt_2 \langle n(t_1)n(t_2) \rangle}. \end{aligned} \quad (23)$$

To evaluate this correlator in the presence of a continuous-wave (CW) drive on the cavity, we first perform a canonical transformation on the cavity operators  $a^{(\dagger)}$  by writing them in terms of a classical  $\alpha^{(*)}$  and a quantum part  $d^{(\dagger)}$ :

$$a(t) = \alpha(t) + d(t). \quad (24)$$

Under this transformation, the coherent state obeying  $a|\alpha\rangle = \alpha|\alpha\rangle$ , is simply the vacuum for the operator  $d$ . It is then easy to verify that

$$\langle (n(t) - \bar{n})(n(0) - \bar{n}) \rangle = \alpha^2 \langle d(t)d^\dagger(0) \rangle = \bar{n}e^{-\frac{\kappa}{2}|t|}. \quad (25)$$

It is interesting to note that the factor of 1/2 in the exponent is due to the presence of the coherent drive. If the resonator is not driven, the photon number correlator rather decays at a rate  $\kappa$ . Using this result in (23) yields the dephasing rate

$$\Gamma_\varphi = 4\theta_0^2 \frac{\kappa}{2} \bar{n}. \quad (26)$$

Since the rate of transmission on resonance is  $\kappa\bar{n}/2$ , this means that the dephasing per transmitted photon is  $4\theta_0^2$ .

To compare this result to the measurement time  $T_{\text{meas}}$ , we imagine a homodyne measurement to determine the

transmitted phase. Standard analysis of such an interferometric set up [14] shows that the minimum phase change which can be resolved using  $N$  photons is  $\delta\theta = 1/\sqrt{N}$ . Hence the measurement time to resolve the phase change  $\delta\theta = 2\theta_0$  is

$$T_m = \frac{1}{2\kappa\bar{n}\theta_0^2}, \quad (27)$$

which yields

$$T_m\Gamma_\varphi = 1. \quad (28)$$

This exceeds the quantum limit [33]  $T_m\Gamma_\varphi = 1/2$  by a factor of 2. Equivalently, in the language of Ref. [34] (which uses a definition of the measurement time twice as large as that above) the efficiency ratio is  $\chi \equiv 1/(T_m\Gamma_\varphi) = 0.5$ .

The failure to reach the quantum limit can be traced [35] to the fact that the coupling of the photons to the qubit is not adiabatic. A small fraction  $R \approx \theta_0^2$  of the photons incident on the resonator are reflected rather than transmitted. Because the phase shift of the reflected wave [14] differs by  $\pi$  between the two states of the qubit, it turns out that, despite its weak intensity, the reflected wave contains precisely the same amount of information about the state of the qubit as the transmitted wave which is more intense but has a smaller phase shift. In the language of Ref. [34], this ‘wasted’ information accounts for the excess dephasing relative to the measurement rate. By measuring also the phase shift of the reflected photons, it could be possible to reach the quantum limit.

Another form of possible back action is mixing transitions between the two qubit states induced by the microwaves. First, as seen from Fig. 6a) and 7a), increasing the average number of photons in the cavity induces mixing. This is simply caused by dressing of the qubit by the cavity photons. Using the dressed states (2) and (3), the level of this coherent mixing can be estimated as

$$P_{\downarrow,\uparrow} = \frac{1}{2} \langle \pm, \bar{n} | \mathbb{1} \pm \sigma^z | \pm, \bar{n} \rangle \quad (29)$$

$$= \frac{1}{2} \left( 1 \pm \frac{\Delta}{\sqrt{4g^2(\bar{n}+1) + \Delta^2}} \right) \quad (30)$$

Exciting the cavity to  $n = n_{\text{crit}}$ , yields  $P_{\downarrow} \sim 0.85$ . As is clear from the numerical results, this process is completely reversible and does not lead to errors in the readout.

The drive can also lead to real transitions between the qubit states. However, since the coupling is so strong, large detuning  $\Delta = 0.1\omega_r$  can be chosen, making the mixing rate limited not by the frequency spread of the drive pulse, but rather by the width of the qubit excited state itself. The rate of driving the qubit from ground to excited state when  $n$  photons are in the cavity is  $R \approx n(g/\Delta)^2\gamma$ . If the measurement pulse excites the cavity to  $n = n_{\text{crit}}$ , we see that the excitation rate is still only 1/4 of the relaxation rate. As a result, the main

limitation on the fidelity of this QND readout is the decay of the excited state of the qubit during the course of the readout. This occurs (for small  $\gamma$ ) with probability  $P_{\text{relax}} \sim \gamma t_{\text{meas}} \sim 15 \times \gamma/\kappa \sim 3.75\%$  and leads to a small error  $P_{\text{err}} \sim 5\gamma/\kappa \sim 1.5\%$  in the measurement, where we have taken  $\gamma = \gamma_\kappa$ . As confirmed by the numerical calculations of Fig. 6 and 7, this dispersive measurement is therefore highly non-demolition.

### C. Signal-to-Noise

For homodyne detection in the case where the cavity pull  $g^2/\Delta\kappa$  is larger than one, the signal-to-noise ratio (SNR) is given by the ratio of the number of photons  $n_{\text{sig}} = n\kappa\Delta t/2$  accumulated over an integration period  $\Delta t$ , divided by the detector noise  $n_{\text{amp}} = k_B T_N / \hbar\omega_r$ . Assuming the integration time to be limited by the qubit’s decay time  $1/\gamma$  and exciting the cavity to a maximal amplitude  $n_{\text{crit}} = 100 \sim n_{\text{amp}}$ , we obtain  $\text{SNR} = (n_{\text{crit}}/n_{\text{amp}})(\kappa/2\gamma)$ . If the qubit lifetime is longer than a few cavity decay times ( $1/\kappa = 160$  ns), this SNR can be very large. In the most optimistic situation where  $\gamma = \gamma_\kappa$ , the signal-to-noise ratio is  $\text{SNR}=200$ .

When taking into account the fact that the qubit has a finite probability to decay during the measurement, a better strategy than integrating the signal for a long time is to take advantage of the large SNR to measure quickly. Simulations have shown that in the situation where  $\gamma = \gamma_\kappa$ , the optimum integration time is roughly 15 cavity lifetimes. This is the pulse length used for the stochastic numerical simulations shown above. The readout fidelity, including the effects of this stochastic decay, and related figures of merit of the single-shot high efficiency QND readout are summarized in Table II.

This scheme has other interesting features that are worth mentioning here. First, since nearly all the energy used in this dispersive measurement scheme is dissipated in the remote terminations of the input and output transmission lines, it has the practical advantage of avoiding quasiparticle generation in the qubit.

Another key feature of the cavity QED readout is that it lends itself naturally to operation of the box at the charge degeneracy point ( $N_g = 1/2$ ), where it has been shown that  $T_2$  can be enormously enhanced [17] because the energy splitting has an extremum with respect to gate voltage and isolation of the qubit from 1/f dephasing is optimal. The derivative of the energy splitting with respect to gate voltage is the charge difference in the two qubit states. At the degeneracy point this derivative vanishes and the environment cannot distinguish the two states and thus cannot dephase the qubit. This also implies that a charge measurement cannot be used to determine the state of the system [4, 5]. While the first derivative of the energy splitting with respect to gate voltage vanishes at the degeneracy point, the second derivative, corresponding to the difference in charge *polarizability* of the two quantum states, is *maximal*. One can think

parameter	symbol	1D circuit
dimensionless cavity pull	$g^2/\kappa\Delta$	2.5
cavity-enhanced lifetime	$\gamma_\kappa^{-1} = (\Delta/g)^2\kappa^{-1}$	64 $\mu\text{s}$
readout SNR	$\text{SNR} = (n_{\text{crit}}/n_{\text{amp}})\kappa/2\gamma$	200 (6)
readout error	$P_{\text{err}} \sim 5 \times \gamma/\kappa$	1.5 % (14%)
1 bit operation time	$T_\pi > 1/\Delta$	> 0.16 ns
entanglement time	$t_{\sqrt{i\text{SWAP}}} = \pi\Delta/4g^2$	$\sim 0.05 \mu\text{s}$
2 bit operations	$N_{\text{op}} = 1/[\gamma t_{\sqrt{i\text{SWAP}}}]$	> 1200 (40)

TABLE II: Figures of merit for readout and multi-qubit entanglement of superconducting qubits using dispersive (off-resonant) coupling to a 1D transmission line resonator. The same parameters as Table 1, and a detuning of the Cooper pair box from the resonator of 10% ( $\Delta = 0.1 \omega_r$ ), are assumed. Quantities involving the qubit decay  $\gamma$  are computed both for the theoretical lower bound  $\gamma = \gamma_\kappa$  for spontaneous emission via the cavity, and (in parentheses) for the current experimental upper bound  $1/\gamma \geq 2 \mu\text{s}$ . Though the signal-to-noise of the readout is very high in either case, the estimate of the readout error rate is dominated by the probability of qubit relaxation during the measurement, which has a duration of a few cavity lifetimes ( $\sim 1 - 10 \kappa^{-1}$ ). If the qubit non-radiative decay is low, both high efficiency readout and more than  $10^3$  two-bit operations could be attained.

of the qubit as a non-linear quantum system having a state-dependent capacitance (or in general, an admittance) which changes sign between the ground and excited states [36]. It is this change in polarizability which is measured in the dispersive QND measurement.

In contrast, standard charge measurement schemes [18, 37] require moving away from the optimal point. Simmonds et al. [20] have recently raised the possibility that there are numerous parasitic environmental resonances which can relax the qubit when its frequency  $\Omega$  is changed during the course of moving the operating point. The dispersive cQED measurement is therefore highly advantageous since it operates best at the charge degeneracy point. In general, such a measurement of an ac property of the qubit is strongly desirable in the usual case where dephasing is dominated by low frequency ( $1/f$ ) noise. Notice also that the proposed quantum non-demolition measurement would be the inverse of the atomic microwave cQED measurement in which the state of the photon field is inferred non-destructively from the phase shift in the state of atoms sent through the cavity [3].

## VII. COHERENT CONTROL

While microwave irradiation of the cavity at its resonance frequency constitutes a measurement, irradiation close to the qubit's frequency can be used to coherently control the state of the qubit. In the former case, the phase shift of the transmitted wave is strongly dependent on the state of the qubit and hence the photons become entangled with the qubit, as shown in Fig. 8. In the latter case however, driving is *not* a measurement because, for large detuning, the photons are largely reflected with a phase shift which is independent of the state of the qubit. There is therefore little entanglement between the field and the qubit in this situation and the rotation fidelity

is high.

To model the effect of the drive on the qubit, we add the microwave drive of Eq. (20) to the Jaynes-Cummings Hamiltonian (1) and apply the transformation (11) (again neglecting damping) to obtain the following effective one-qubit Hamiltonian

$$H_{1q} = \frac{\hbar}{2} \left[ \Omega + 2\frac{g^2}{\Delta} \left( a^\dagger a + \frac{1}{2} \right) - \omega_{\mu w} \right] \sigma^z + \hbar \frac{g\varepsilon(t)}{\Delta} \sigma^x + \hbar(\omega_r - \omega_{\mu w}) a^\dagger a + \hbar\varepsilon(t)(a^\dagger + a), \quad (31)$$

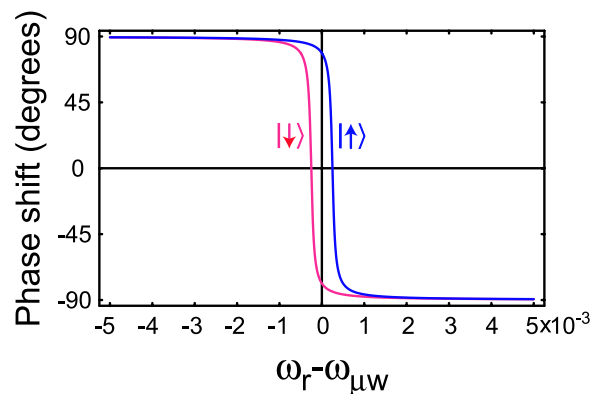


FIG. 8: (color online). Phase shift of the cavity field for the two states of the qubit as a function of detuning between the driving and resonator frequencies. Obtained from the steady-state solution of the equation of motion for  $a(t)$  while only taking into account damping on the cavity and using the parameters of Table I. Read-out of the qubit is realized at, or close to, zero detuning between the drive and resonator frequencies where the dependence of the phase shift on the qubit state is largest. Coherent manipulations of the qubit are realized close to the qubit frequency which is 10% detuned from the cavity (not shown on this scale). At such large detunings, there is little dependence of the phase shift on the qubit's state.

in a frame rotating at the drive frequency  $\omega_{\mu w}$ . Choosing  $\omega_{\mu w} = \Omega + (2n + 1)g^2/\Delta$ ,  $H_{1q}$  generates rotations of the qubit about the  $x$  axis with Rabi frequency  $g\varepsilon/\Delta$ . Different drive frequencies can be chosen to realize rotations around arbitrary axes in the  $x$ - $z$  plane. In particular, choosing  $\omega_{\mu w} = \Omega + (2n + 1)g^2/\Delta - 2g\varepsilon/\Delta$  and  $t = \pi\Delta/2\sqrt{2}g\varepsilon$  generates the Hadamard transformation  $\mathcal{H}$ . Since  $\mathcal{H}\sigma_x\mathcal{H} = \sigma_z$ , these two choices of frequency are sufficient to realize any 1-qubit logical operation.

Assuming that we can take full advantage of lifetime enhancement inside the cavity (i.e. that  $\gamma = \gamma_\kappa$ ), the number of  $\pi$  rotations about the  $x$  axis which can be carried out is  $N_\pi = 2\varepsilon\Delta/\pi g\kappa \sim 10^5\varepsilon$  for the experimental parameters assumed in Table I. For large  $\varepsilon$ , the choice of drive frequency must take into account the power dependence of the cavity frequency pulling.

Numerical simulation shown in Fig. 9 confirms this simple picture and that single-bit rotations can be performed with very high fidelity. It is interesting to note that since detuning between the resonator and the drive is large, the cavity is only virtually populated, with an average photon number  $\bar{n} \approx \varepsilon^2/\Delta^2 \sim 0.1$ . Virtual population and depopulation of the cavity can be realized much faster than the cavity lifetime  $1/\kappa$  and, as a result, the qubit feels the effect of the drive rapidly after the drive has been turned on. The limit on the speed of turn on and off of the drive is set by the detuning  $\Delta$ . If the drive is turned on faster than  $1/\Delta$ , the frequency spread of the drive is such that part of the drive's photons will pick up phase information (see Fig. 8) and dephase the qubit. As a result, for large detuning, this approach leads to a fast and accurate way to coherently control the state of the qubit.

To model the effect of the drive on the resonator an alternative model is to use the cavity-modified Maxwell-Bloch equations [25]. As expected, numerical integration of the Maxwell-Bloch equations reproduce very well the stochastic numerical results when the drive is at the qubit's frequency but do *not* reproduce these numerical results when the drive is close to the bare resonator frequency (Fig. 6 and 7), i.e. when entanglement between the qubit and the photons cannot be neglected.

### VIII. RESONATOR AS QUANTUM BUS: ENTANGLEMENT OF MULTIPLE QUBITS

The transmission-line resonator has the advantage that it should be possible to place multiple qubits along its length ( $\sim 1$  cm) and entangle them together, which is an essential requirement for quantum computation. For the case of two qubits, they can be placed closer to the ends of the resonator but still well isolated from the environment and can be separately dc biased by capacitive coupling to the left and right center conductors of the transmission line. Additional qubits would have to have separate gate bias lines installed.

For the pair of qubits labeled  $i$  and  $j$ , both coupled

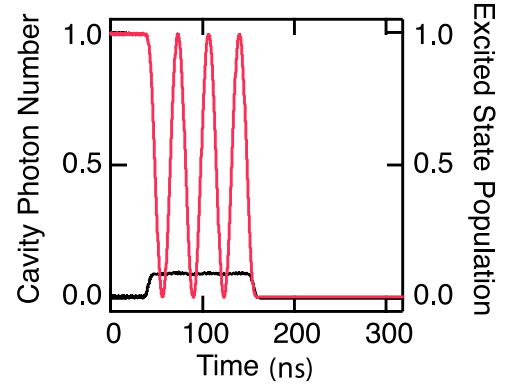


FIG. 9: (color online). Numerical stochastic wave function simulation showing coherent control of a qubit by microwave irradiation of the cavity at the ac-Stark and Lamb shifted qubit frequency. The qubit is first left to evolve freely for about 40ns. The drive is turned on for  $t = 7\pi\Delta/2g\varepsilon \sim 115$ ns, corresponding to  $7\pi$  pulses, and then turned off. Since the drive is tuned far away from the cavity, the cavity photon number is small even for the moderately large drive amplitude  $\varepsilon = 0.03\omega_r$  used here.

with strength  $g$  to the cavity and detuned from the resonator but in resonance with each other, the transformation (11) yields the effective two-qubit Hamiltonian [3, 38, 39]

$$H_{2q} \approx \hbar \left[ \omega_r + \frac{g^2}{\Delta} (\sigma_i^z + \sigma_j^z) \right] a^\dagger a + \frac{1}{2} \hbar \left[ \Omega + \frac{g^2}{\Delta} \right] (\sigma_i^z + \sigma_j^z) + \hbar \frac{g^2}{\Delta} (\sigma_i^+ \sigma_j^- + \sigma_i^- \sigma_j^+). \quad (32)$$

In addition to ac-Stark and Lamb shifts, the last term couples the qubits through virtual excitations of the resonator.

In a frame rotating at the qubit's frequency  $\Omega$ ,  $H_{2q}$  generates the evolution

$$U_{2q}(t) = \exp \left[ -i \frac{g^2}{\Delta} t \left( a^\dagger a + \frac{1}{2} \right) (\sigma_i^z + \sigma_j^z) \right] \cdot \begin{pmatrix} 1 & & & \\ & \cos \frac{g^2 t}{\Delta} & i \sin \frac{g^2 t}{\Delta} & \\ & i \sin \frac{g^2 t}{\Delta} & \cos \frac{g^2 t}{\Delta} & \\ & & & 1 \end{pmatrix} \otimes \mathbb{1}_r, \quad (33)$$

where  $\mathbb{1}_r$  is the identity operator in the resonator space. Up to phase factors, this corresponds at  $t = \pi\Delta/4g^2 \sim 50$  ns to a  $\sqrt{i}$ SWAP logical operation. Up to one-qubit gates, this operation is equivalent to the controlled-NOT. Together with one-qubit gates, the interaction  $H_{2q}$  is therefore sufficient for universal quantum computation [40]. Assuming again that we can take full advantage of the lifetime enhancement inside the cavity, the number of  $\sqrt{i}$ SWAP operations which can be carried out is  $N_{2q} = 4\Delta/\pi\kappa \sim 1200$  for the parameters assumed above.

This can be further improved if the qubit's non-radiative decay is sufficiently small, and higher  $Q$  cavities are employed.

When the qubits are detuned from each other, the off-diagonal coupling provided by  $H_{2q}$  is only weakly effective and the coupling is for all practical purposes turned off. Two-qubit logical gates in this setup can therefore be controlled by individually tuning the qubits. Moreover, single-qubit and two-qubit logical operations on different qubits and pairs of qubits can both be realized simultaneously, a requirement to reach presently known thresholds for fault-tolerant quantum computation [41].

It is interesting to point out that the dispersive QND readout presented in section VI may be able to determine the state of multiple qubits in a single shot without the need for additional signal ports. For example, for the case of two qubits with different detunings, the cavity pull will take four different values  $\pm g_1^2/\Delta_1 \pm g_2^2/\Delta_2$  allowing single-shot readout of the coupled system. This can in principle be extended to  $N$  qubits provided that the range of individual cavity pulls can be made large enough to distinguish all the combinations. Alternatively, one could read them out in small groups at the expense of having to electrically vary the detuning of each group to bring them into strong coupling with the resonator.

## IX. ENCODED UNIVERSALITY AND DECOHERENCE-FREE SUBSPACE

Universal quantum computation can also be realized in this architecture under the encoding  $\mathcal{L} = \{|\uparrow\downarrow\rangle, |\downarrow\uparrow\rangle\}$  by controlling only the qubit's detuning and, therefore, by turning on and off the interaction term in  $H_{2q}$  [42].

An alternative encoded two-qubit logical operation to the one suggested in Ref. [42] can be realized here by tuning the four qubits forming the pair of encoded qubits in resonance for a time  $t = \pi\Delta/3g^2$ . The resulting effective evolution operator can be written as  $\hat{U}_{2q} = \exp[-i(\pi\Delta/3g^2)\hat{\sigma}_{x1}\hat{\sigma}_{x2}]$ , where  $\hat{\sigma}_{xi}$  is a Pauli operator acting on the  $i^{\text{th}}$  encoded qubit. Together with encoded one-qubit operations,  $\hat{U}_{2q}$  is sufficient for universal quantum computation using the encoding  $\mathcal{L}$ .

We point out that the subspace  $\mathcal{L}$  is a decoherence-free subspace with respect to global dephasing [43] and use of this encoding will provide some protection against noise. The application of  $\hat{U}_{2q}$  on the encoded subspace  $\mathcal{L}$  however causes temporary leakage out of this protected subspace. This is also the case with the approach of Ref. [42]. In the present situation however, since the Hamiltonian generating  $\hat{U}_{2q}$  commutes with the generator of global dephasing, this temporary excursion out of the protected subspace does not induce noise on the encoded qubit.

## X. SUMMARY AND CONCLUSIONS

In summary, we propose that the combination of one-dimensional superconducting transmission line resonators, which confine their zero point energy to extremely small volumes, and superconducting charge qubits, which are electrically controllable qubits with large electric dipole moments, constitutes an interesting system to access the strong-coupling regime of cavity quantum electrodynamics. This combined system is an advantageous architecture for the coherent control, entanglement, and readout of quantum bits for quantum computation and communication. Among the practical benefits of this approach are the ability to suppress radiative decay of the qubit while still allowing one-bit operations, a simple and minimally disruptive method for readout of single and multiple qubits, and the ability to generate tunable two-qubit entanglement over centimeter-scale distances. We also note that in the structures described here, the emission or absorption of a single photon by the qubit is tagged by a sudden large change in the resonator transmission properties [29] making them potentially useful as single photon sources and detectors.

### Acknowledgments

We are grateful to David DeMille, Michel Devoret, Clifford Cheung and Florian Marquardt for useful conversations. We also thank André-Marie Tremblay and the Canadian Foundation for Innovation for access to computing facilities. This work was supported in part by the National Security Agency (NSA) and Advanced Research and Development Activity (ARDA) under Army Research Office (ARO) contract number DAAD19-02-1-0045, NSF DMR-0196503, NSF DMR-0342157, the David and Lucile Packard Foundation, the W.M. Keck Foundation and NSERC.

### APPENDIX A: QUANTIZATION OF THE 1D TRANSMISSION LINE RESONATOR

A transmission line of length  $L$ , whose cross section dimension is much less than the wavelength of the transmitted signal can be approximated by a 1-D model. For relatively low frequencies it is well described by an infinite series of inductors with each node capacitively connected to ground, as shown in Fig. 2. Denoting the inductance per unit length  $l$  and the capacitance per unit length  $c$ , the Lagrangian of the circuit is

$$\mathcal{L} = \int_{-L/2}^{L/2} dx \left( \frac{l}{2} j^2 - \frac{1}{2c} q^2 \right), \quad (\text{A1})$$

where  $j(x, t)$  and  $q(x, t)$  are the local current and charge density, respectively. We have ignored for the moment

the two semi-infinite transmission lines capacitively coupled to the resonator. Defining the variable  $\theta(x, t)$

$$\theta(x, t) \equiv \int_{-L/2}^x dx' q(x', t), \quad (\text{A2})$$

the Lagrangian can be rewritten as

$$\mathcal{L} = \int_{-L/2}^{L/2} dx \left( \frac{l}{2} \dot{\theta}^2 - \frac{1}{2c} (\nabla\theta)^2 \right). \quad (\text{A3})$$

The corresponding Euler-Lagrange equation is a wave equation with the speed  $v = \sqrt{l/c}$ . Using the boundary conditions due to charge neutrality

$$\theta(-L/2, t) = \theta(L/2, t) = 0, \quad (\text{A4})$$

we obtain

$$\begin{aligned} \theta(x, t) = & \sqrt{\frac{2}{L}} \sum_{k_o=1}^{k_o, \text{cutoff}} \phi_{k_o}(t) \cos \frac{k_o \pi x}{L} \\ & + \sqrt{\frac{2}{L}} \sum_{k_e=2}^{k_e, \text{cutoff}} \phi_{k_e}(t) \sin \frac{k_e \pi x}{L}, \end{aligned} \quad (\text{A5})$$

for odd and even modes, respectively. For finite length  $L$ , the transmission line acts as a resonator with resonant frequencies  $\omega_k = k\pi v/L$ . The cutoff is determined by the fact that the resonator is not strictly one dimensional.

Using the normal mode expansion (A5) in (A3), one obtains, after spatial integration, the Lagrangian in the form of a set of harmonic oscillators

$$\mathcal{L} = \sum_k \frac{l}{2} \dot{\phi}_k^2 - \frac{1}{2c} \left( \frac{k\pi}{L} \right)^2 \phi_k^2. \quad (\text{A6})$$

Promoting the variable  $\phi_k$  and its canonically conjugated momentum  $\pi_k = l\dot{\phi}_k$  to conjugate operators and introducing the boson creation and annihilation operators  $a_k^\dagger$  and  $a_k$  satisfying  $[a_k, a_{k'}^\dagger] = \delta_{kk'}$ , we obtain the usual relations diagonalizing the Hamiltonian obtained from the Lagrangian (A6)

$$\hat{\phi}_k(t) = \sqrt{\frac{\hbar\omega_k c}{2}} \frac{L}{k\pi} (a_k(t) + a_k^\dagger(t)) \quad (\text{A7})$$

$$\hat{\pi}_k(t) = -i\sqrt{\frac{\hbar\omega_k l}{2}} (a_k(t) - a_k^\dagger(t)). \quad (\text{A8})$$

From these relations, the voltage on the resonator can be expressed as

$$\begin{aligned} V(x, t) &= \frac{1}{c} \frac{\partial\theta(x, t)}{\partial x} \quad (\text{A9}) \\ &= - \sum_{k_o=1}^{\infty} \sqrt{\frac{\hbar\omega_{k_o}}{Lc}} \sin \left( \frac{k_o \pi x}{L} \right) [a_{k_o}(t) + a_{k_o}^\dagger(t)] \\ &\quad + \sum_{k_e=1}^{\infty} \sqrt{\frac{\hbar\omega_{k_e}}{Lc}} \cos \left( \frac{k_e \pi x}{L} \right) [a_{k_e}(t) + a_{k_e}^\dagger(t)]. \end{aligned}$$

In the presence of the two semi-infinite transmission lines coupled to the resonator, the Lagrangian (A3) and the boundary conditions (A4) are modified to take into account the voltage drop on the coupling capacitors  $C_0$ . Assuming no spatial extent for the capacitors  $C_0$ , the problem is still solvable analytically. Due to this coupling, the wavefunction can now extend outside of the central segment which causes a slight red-shift, of order  $C_0/Lc$ , of the cavity resonant frequency.

As shown in Fig. 2, we assume the qubit to be fabricated at the center of the resonator. As a result, at low temperatures, the qubit is coupled to the mode  $k = 2$  of the resonator, which as an anti-node of the voltage in its center. The rms voltage between the center conductor and the ground plane is then  $V_{\text{rms}}^0 = \sqrt{\hbar\omega_r/cL}$  with  $\omega_r = \omega_2$  and the voltage felt by the qubit is  $V(0, t) = V_{\text{rms}}^0(a_2(t) + a_2^\dagger(t))$ . In the main body of this paper, we work only with this second harmonic and drop the mode index on the resonator operators.

## APPENDIX B: TREATMENT OF DISSIPATION

The evolution of the total density matrix, including the qubit, cavity mode and baths, is described by the von Neuman equation

$$\dot{\rho}_{\text{tot}} = -i[H_{\text{sys}} + H_\kappa + H_\gamma, \rho_{\text{tot}}], \quad (\text{B1})$$

where  $H_{\text{sys}}$  stands for the first three terms of Eq. (1) plus the drive Hamiltonian of Eq. (20). When the coupling between the system (qubit plus cavity mode) and the baths is weak, the reduced density operator for the system can be shown to obey the master equation [14]

$$\dot{\rho} = -i[H_{\text{sys}}, \rho] - \sum_{m=\{\kappa, \gamma\}} (L_m^\dagger L_m \rho + \rho L_m^\dagger L_m - 2L_m \rho L_m^\dagger) \quad (\text{B2})$$

in the Markov approximation. Here,  $L_m$  are Lindblad operators describing the effect of the baths on the system and can be expressed as  $L_\kappa = \sqrt{\kappa}a$  and  $L_\gamma = \sqrt{\gamma}\sigma^-$ . The effect of finite temperature and pure dephasing, for example, can also be taken into account easily by introducing additional Lindblad operators.

The master equation is solved numerically by truncating the cavity Hilbert space to  $N$  photons. This leads to  $(2N)^2$  coupled differential equations which, for large  $N$ , can be difficult to solve in practice. An alternative approach is to write an equivalent stochastic differential equation for the wavefunction [32, 44]. There exist different such ‘unravellings’ of the master equation and here we use the quantum state diffusion equation [32, 44]

$$\begin{aligned} |d\psi\rangle &= -iH_{\text{sys}} |\psi\rangle dt + \sum_m (L_m - \langle L_m \rangle_\psi) |\psi\rangle d\xi_m \\ &- \sum_m (L_m^\dagger L_m + \langle L_m^\dagger \rangle_\psi \langle L_m \rangle_\psi - 2\langle L_m^\dagger \rangle_\psi \langle L_m \rangle_\psi) |\psi\rangle dt. \end{aligned} \quad (\text{B3})$$

The  $d\xi_m$  are complex independent Wiener processes satisfying

$$\overline{d\xi_m} = \overline{d\xi_m d\xi_n} = 0, \quad (\text{B4})$$

$$\overline{d\xi_m^* d\xi_n} = \delta_{mn} dt. \quad (\text{B5})$$

An advantage of this approach is that now only  $2N$  coupled differential equations have to be solved. A drawback is that the results must be averaged over many realizations of the noise to obtain accurate results. Still, this leads to much less important memory usage and to speedup in the numerical calculations [32, 45].

### APPENDIX C: QUANTUM NON-DEMOLITION MEASUREMENTS

Read-out of a qubit can lead to both mixing and dephasing [23, 33]. While dephasing is unavoidable, mixing of the measured observable can be eliminated in a QND measurement by choosing the qubit-measurement apparatus interaction such that the measured observable is a

constant of motion. In that situation, the measurement-induced mixing is rather introduced in the operator conjugate to the operator being measured.

In the situation of interest in this paper, the operator being probed is  $\sigma_z$  and, from Eq. (12), the qubit-measurement apparatus interaction Hamiltonian is  $H_{\text{int}} = (g^2/\Delta)\sigma_z a^\dagger a$ , such that  $[\sigma_z, H_{\text{int}}] = 0$ . For  $\sigma_z$  to be a constant of motion also requires that it commutes with the qubit Hamiltonian. This condition is also satisfied in Eq. (12).

That the measured observable is a constant of motion implies that repeated observations will yield the same result. This allows for the measurement result to reach arbitrary large accuracy by accumulating signal. In practice however, there are always environmental dissipation mechanisms acting on the qubit independently of the read-out. Even in a QND situation, these will lead to a finite mixing rate  $1/T_1$  of the qubit in the course of the measurement. Hence, high fidelity can only be achieved by a strong measurement completed in a time  $T_m \ll T_1$ . This simple point is not as widely appreciated as it should be.

- 
- [1] H. Mabuchi and A. Doherty, *Science* **298**, 1372 (2002).
  - [2] C. J. Hood, T. W. Lynn, A. C. Doherty, A. S. Parkins, and H. J. Kimble, *Science* **287**, 1447 (2000).
  - [3] J. Raimond, M. Brune, and S. Haroche, *Rev. Mod. Phys.* **73**, 565 (2001).
  - [4] A. Armour, M. Blencowe, and K. C. Schwab, *Phys. Rev. Lett.* **88**, 148301 (2002).
  - [5] E. K. Irish and K. Schwab (2003), *cond-mat/0301252*.
  - [6] Y. Makhlin, G. Schön, and A. Shnirman, *Rev. Mod. Phys.* **73**, 357 (2001).
  - [7] O. Buisson and F. Hekking, in *Macroscopic Quantum Coherence and Quantum Computing*, edited by D. V. Averin, B. Ruggiero, and P. Silvestrini (Kluwer, New York, 2001).
  - [8] F. Marquardt and C. Bruder, *Phys. Rev. B* **63**, 054514 (2001).
  - [9] F. Plastina and G. Falci, *Phys. Rev. B* **67**, 224514 (2003).
  - [10] A. Blais, A. Maassen van den Brink, and A. Zagoskin, *Phys. Rev. Lett.* **90**, 127901 (2003).
  - [11] W. Al-Saidi and D. Stroud, *Phys. Rev. B* **65**, 014512 (2001).
  - [12] C.-P. Yang, S.-I. Chu, and S. Han, *Phys. Rev. A* **67**, 042311 (2003).
  - [13] J. Q. You and F. Nori, *Phys. Rev. B* **68**, 064509 (2003).
  - [14] D. Walls and G. Milburn, *Quantum optics* (Springer-Verlag, Berlin, 1994).
  - [15] S. Haroche, in *Fundamental Systems in Quantum Optics*, edited by J. Dalibard, J. Raimond, and J. Zinn-Justin (Elsevier, 1992), p. 767.
  - [16] V. Bouchiat, D. Vion, P. Joyez, D. Esteve, and M. Devoret, *Physica Scripta* **T76**, 165 (1998).
  - [17] D. Vion, A. Aassime, A. Cottet, P. Joyez, H. Pothier, C. Urbina, D. Esteve, and M. Devoret, *Science* **296**, 886 (2002).
  - [18] K. Lehnert, K. Bladh, L. Spietz, D. Gunnarsson, D. Schuster, P. Delsing, and R. Schoelkopf, *Phys. Rev. Lett.* **90**, 027002 (2003).
  - [19] A. S. Sorensen, C. H. van der Wal, L. Childress, and M. D. Lukin (2003), (*quant-ph/0308145*).
  - [20] R. W. Simmonds, K. M. Lang, D. A. Hite, D. P. Pappas, and J. Martinis (2003), submitted to *Phys. Rev. Lett.*
  - [21] P. K. Day, H. G. LeDuc, B. A. Mazin, A. Vayonakis, and J. Zmuidzinas, *Nature (London)* **425**, 817 (2003).
  - [22] A. Wallraff and R. Schoelkopf, unpublished.
  - [23] R. Schoelkopf, A. Clerk, S. Girvin, K. Lehnert, and M. Devoret, *Quantum noise in mesoscopic physics* (Kluwer Ac. Publ., 2003), chap. Qubits as Spectrometers of Quantum Noise, pp. 175–203.
  - [24] H. Kimble, *Structure and dynamics in cavity quantum electrodynamics* (Academic Press, 1994).
  - [25] C. Wang and R. Vyas, *Phys. Rev. A* **55**, 823 (1997).
  - [26] A lumped LC circuit was used in Ref. [27, 28] to probe flux qubits in a different way.
  - [27] E. Il'ichev, N. Oukhanski, A. Izmailkov, T. Wagner, M. Grajcar, H.-G. Meyer, A. Y. Smirnov, A. M. van den Brink, M. Amin, and A. Zagoskin, *Phys. Rev. Lett.* **91**, 097906 (2003).
  - [28] A. Izmailkov, M. Grajcar, E. Il'ichev, T. Wagner, H.-G. Meyer, A. Smirnov, M. Amin, A. Maassen van den Brink, and A. Zagoskin (2004), *cond-mat/0312332*.
  - [29] S. Girvin, A. Blais, and R. Huang, unpublished.
  - [30] We note that for the case of  $Q = 10^6$ , the cavity pull is a remarkable  $\pm 250$  line widths, but, depending on the non-radiative decay rate of the qubit, this may be in the regime  $\kappa < \gamma$ , making the state measurement too slow.
  - [31] S. van Enk, J. Cirac, and P. Zoller, *Science* **279**, 2059 (1998).
  - [32] R. Schack and T. A. Brun, *Comp. Phys. Comm.* **102**, 210 (1997).
  - [33] M. Devoret and R. Schoelkopf, *Nature* **406**, 1039 (2000).

- [34] A. Clerk, S. Girvin, and A. Stone, *Phys. Rev. B* **67**, 165324 (2003).
- [35] F. Marquardt, unpublished.
- [36] D. Averin and C. Bruder, *Phys. Rev. Lett.* **91**, 057003 (2003).
- [37] Y. Nakamura, Y. Pashkin, and J. Tsai, *Nature (London)* **398**, 786 (1999).
- [38] A. Sørensen and K. Mølmer, *Phys. Rev. Lett.* **82**, 1971 (1999).
- [39] S.-B. Zheng and G.-C. Guo, *Phys. Rev. Lett.* **85**, 2392 (2000).
- [40] A. Barenco, C. Bennett, R. Cleve, D. DiVincenzo, N. Margolus, S. P. T. Sleator, J. Smolin, and H. Weinfurter, *Phys. Rev. A* **52**, 3457 (1995).
- [41] D. Aharonov and M. Ben-Or, in *Proceedings of the 37th Annual Symposium on Foundations of Computer Science* (IEEE Comput. Soc. Press, 1996), p. 46.
- [42] D. Lidar and L.-A. Wu, *Phys. Rev. Lett.* **88**, 017905 (2002).
- [43] J. Kempe, D. Bacon, D. Lidar, and K. B. Whaley, *Phys. Rev. A* **63**, 042307 (2001).
- [44] C. Gardiner and P. Zoller, *Quantum Noise* (Springer Verlag, 2000).
- [45] K. Molmer, Y. Castin, and J. Dalibard, *J. Opt. Soc. Am. B* **10**, 524 (1993).

coupled system by applying pulses of varying length. In Fig. 3b, Rabi oscillations are shown for the  $|00\rangle$  to  $|11\rangle$  transition. When the microwave frequency is detuned from resonance, the Rabi oscillations are accelerated (bottom four curves, to be compared with the fifth curve). After a  $\pi$  pulse which prepares the system in the  $|10\rangle$  state, these oscillations are suppressed (second curve in Fig. 3b). After a  $2\pi$  pulse they are revived (first curve in Fig. 3b). In the case of Fig. 3c, the qubit is first excited onto the  $|10\rangle$  state by a  $\pi$  pulse, and a second pulse in resonance with the red sideband transition drives the system between the  $|10\rangle$  and  $|01\rangle$  states. The Rabi frequency depends linearly on the microwave amplitude, with a smaller slope compared to the bare qubit driving. During the time evolution of the coupled Rabi oscillations shown in Fig. 3b and c, the qubit and the oscillator experience a time-dependent entanglement, although the present data do not permit us to quantify it to a sufficient degree of confidence.

The sideband Rabi oscillations of Fig. 3 show a short coherence time ( $\sim 3$  ns), which we attribute mostly to the oscillator relaxation. To determine its relaxation time, we performed the following experiment. First, we excite the oscillator with a resonant low power microwave pulse. After a variable delay  $\Delta t$ , during which the oscillator relaxes towards  $n = 0$ , we start recording Rabi oscillations on the red sideband transition (see Fig. 4a for  $\Delta t = 1$  ns). The decay of the oscillation amplitude as a function of  $\Delta t$  corresponds to an oscillator relaxation time of  $\sim 6$  ns (Fig. 4b), consistent with a quality factor of 100–150 estimated from the width of the  $\nu_p$  resonance. The exponential fit (continuous line in Fig. 4b) shows an offset of  $\sim 4\%$  due to thermal effects. To estimate the higher bound of the sample temperature, we consider that the visibility of the oscillations presented here (Figs 2–4) is set by the detection efficiency and not by the state preparation. When related to the maximum signal of the qubit Rabi oscillations of  $\sim 40\%$ , the 4%-offset corresponds to  $\sim 10\%$  thermal occupation of oscillator excited states (an effective temperature of  $\sim 60$  mK). Consistently, we also observe low-amplitude red sideband oscillations without preliminary microwave excitation of the oscillator.

We have demonstrated coherent dynamics of a coupled superconducting two-level plus harmonic oscillator system, implying that the two subsystems are entangled. Increasing the coupling strength and the oscillator relaxation time should allow us to quantify the entanglement, as well as to study non-classical states of the oscillator. Our results provide strong indications that solid-state quantum devices could in future be used as elements for the manipulation of quantum information.  $\square$

Received 25 May; accepted 5 July 2004; doi:10.1038/nature02831.

1. Nielsen, M. A. & Chuang, I. L. *Quantum Computation and Quantum Information* (Cambridge Univ. Press, Cambridge, 2000).
2. Nakamura, Y. *et al.* Coherent control of macroscopic quantum states in a single-Cooper-pair box. *Nature* **398**, 786–788 (1999).
3. Vion, D. *et al.* Manipulating the quantum state of an electrical circuit. *Science* **296**, 886–889 (2002).
4. Yu, Y., Han, S., Chu, X., Chu, S. & Wang, Z. Coherent temporal oscillations of macroscopic quantum states in a Josephson junction. *Science* **296**, 889–892 (2002).
5. Martinis, J. M., Nam, S., Aumentado, J. & Urbina, C. Rabi oscillations in a large Josephson-junction qubit. *Phys. Rev. Lett.* **89**, 117901 (2002).
6. Chiorescu, I., Nakamura, Y., Harmans, C. J. P. M. & Mooij, J. E. Coherent quantum dynamics of a superconducting flux qubit. *Science* **299**, 1869–1871 (2003).
7. Pashkin, Yu. A. *et al.* Quantum oscillations in two coupled charge qubits. *Nature* **421**, 823–826 (2003).
8. Berkley, A. J. *et al.* Entangled macroscopic quantum states in two superconducting qubits. *Science* **300**, 1548–1550 (2003).
9. Majer, J. B., Paauf, F. G., ter Haar, A. C. J., Harmans, C. J. P. M. & Mooij, J. E. Spectroscopy on two coupled flux qubits. Preprint at (<http://arxiv.org/abs/cond-mat/0308192>) (2003).
10. Izmalkov, A. *et al.* Experimental evidence for entangled states formation in a system of two coupled flux qubits. Preprint at (<http://arxiv.org/abs/cond-mat/0312332>) (2003).
11. Yamamoto, T., Pashkin, Yu. A., Astafiev, O., Nakamura, Y. & Tsai, J. S. Demonstration of conditional gate operation using superconducting charge qubits. *Nature* **425**, 941–944 (2003).
12. Leibfried, D., Blatt, R., Monroe, C. & Wineland, D. Quantum dynamics of single trapped ions. *Rev. Mod. Phys.* **75**, 281–324 (2003).
13. Mandel, O. *et al.* Controlled collisions for multi-particle entanglement of optically trapped atoms. *Nature* **425**, 937–940 (2003).
14. Raimond, J. M., Brune, M. & Haroche, S. Manipulating quantum entanglement with atoms and photons in a cavity. *Rev. Mod. Phys.* **73**, 565–582 (2001).

15. Mooij, J. E. *et al.* Josephson persistent-current qubit. *Science* **285**, 1036–1039 (1999).
16. van der Wal, C. H. *et al.* Quantum superposition of macroscopic persistent-current states. *Science* **290**, 773–777 (2000).
17. Burkard, G. *et al.* Asymmetry and decoherence in double-layer persistent-current qubit. Preprint at (<http://arxiv.org/abs/cond-mat/0405273>) (2004).
18. Goorden, M. C., Thorwart, M. & Grifoni, M. Entanglement spectroscopy of a driven solid-state qubit and its detector. Preprint at (<http://arxiv.org/abs/cond-mat/0405220>) (2004).
19. Tinkham, M. *Introduction to Superconductivity* 2nd edn (McGraw-Hill, New York, 1996).
20. Cohen-Tannoudji, C., Dupont-Roc, J. & Grynberg, G. *Atom-photon Interactions: Basic Processes and Applications* Ch. II E (Wiley & Sons, New York, 1992).

**Acknowledgements** We thank A. Blais, G. Burkard, D. DiVincenzo, G. Falci, M. Grifoni, S. Lloyd, S. Miyashita, T. Orlando, R. N. Schouten, L. Vandersypen and F. K. Wilhelm for discussions. This work was supported by the Dutch Foundation for Fundamental Research on Matter (FOM), the EU Marie Curie and SQUBIT grants, and the US Army Research Office.

**Competing interests statement** The authors declare that they have no competing financial interests.

**Correspondence** and requests for materials should be addressed to I.C. ([chiorescu@pa.msu.edu](mailto:chiorescu@pa.msu.edu)) and J.E.M. ([mooij@qt.tn.tudelft.nl](mailto:mooij@qt.tn.tudelft.nl)).

## Strong coupling of a single photon to a superconducting qubit using circuit quantum electrodynamics

A. Wallraff<sup>1</sup>, D. I. Schuster<sup>1</sup>, A. Blais<sup>1</sup>, L. Frunzio<sup>1</sup>, R.-S. Huang<sup>1,2</sup>, J. Majer<sup>1</sup>, S. Kumar<sup>1</sup>, S. M. Girvin<sup>1</sup> & R. J. Schoelkopf<sup>1</sup>

<sup>1</sup>Departments of Applied Physics and Physics, Yale University, New Haven, Connecticut 06520, USA

<sup>2</sup>Department of Physics, Indiana University, Bloomington, Indiana 47405, USA

The interaction of matter and light is one of the fundamental processes occurring in nature, and its most elementary form is realized when a single atom interacts with a single photon. Reaching this regime has been a major focus of research in atomic physics and quantum optics<sup>1</sup> for several decades and has generated the field of cavity quantum electrodynamics<sup>2,3</sup>. Here we perform an experiment in which a superconducting two-level system, playing the role of an artificial atom, is coupled to an on-chip cavity consisting of a superconducting transmission line resonator. We show that the strong coupling regime can be attained in a solid-state system, and we experimentally observe the coherent interaction of a superconducting two-level system with a single microwave photon. The concept of circuit quantum electrodynamics opens many new possibilities for studying the strong interaction of light and matter. This system can also be exploited for quantum information processing and quantum communication and may lead to new approaches for single photon generation and detection.

In atomic cavity quantum electrodynamics (QED), an isolated atom with electric dipole moment  $d$  interacts with the vacuum state electric field  $E_0$  of a cavity. The quantum nature of the field gives rise to coherent oscillations of a single excitation between the atom and the cavity at the vacuum Rabi frequency  $\nu_{\text{Rabi}} = 2dE_0/\hbar$ , which can be observed when  $\nu_{\text{Rabi}}$  exceeds the rates of relaxation and decoherence of both the atom and the field. This effect has been observed in the time domain using Rydberg atoms in three-dimensional microwave cavities<sup>3</sup> and spectroscopically using alkali atoms in very small optical cavities with large vacuum fields<sup>4</sup>.

Coherent quantum effects have been recently observed in several superconducting circuits<sup>5–10</sup>, making these systems well suited for use as quantum bits (qubits) for quantum information processing.

Of the various superconducting qubits, the Cooper pair box<sup>11</sup> is especially well suited for cavity QED because of its large effective electric dipole moment  $d$ , which can be  $10^4$  times larger than in an alkali atom and ten times larger than a typical Rydberg atom<sup>12</sup>. As suggested in our earlier theoretical study<sup>12</sup>, the simultaneous combination of this large dipole moment and the large vacuum field strength—due to the small size of the quasi one-dimensional transmission line cavity—in our implementation is ideal for reaching the strong coupling limit of cavity QED in a circuit. Other solid-state analogues of strong coupling cavity QED have been envisaged in superconducting<sup>13–20</sup>, semiconducting<sup>21,22</sup>, and even micro-mechanical systems<sup>23</sup>. First steps towards realizing such a regime have been made for semiconductors<sup>21,24,25</sup>. To our knowledge, our experiments constitute the first experimental observation of strong coupling cavity QED with a single artificial atom and a single photon in a solid-state system.

The on-chip cavity is made by patterning a thin superconducting film deposited on a silicon chip. The quasi-one-dimensional coplanar waveguide resonator<sup>26</sup> consists of a narrow centre conductor of length  $l$  and two nearby lateral ground planes, see Fig. 1a. Close to its full-wave ( $l = \lambda$ ) resonance frequency,  $\omega_r = 2\pi\nu_r = 1/\sqrt{LC} = 2\pi \cdot 6.044$  GHz, where  $\nu_r$  is the bare resonance frequency, the resonator can be modelled as a parallel combination of a capacitor  $C$  and an inductor  $L$  (the internal losses are negligible). This simple resonant circuit behaves as a harmonic oscillator described by the hamiltonian  $H_r = \hbar\omega_r(a^\dagger a + 1/2)$ , where  $\langle a^\dagger a \rangle = \langle \hat{n} \rangle = n$  is the average photon number. At our operating temperature of  $T < 100$  mK, much less than  $\hbar\omega_r/k_B \approx 300$  mK, the resonator is nearly in its ground state, with a thermal occupancy  $n < 0.06$ . The vacuum fluctuations of the resonator give rise to a root mean square (r.m.s.) voltage  $V_{\text{rms}} = \sqrt{\hbar\omega_r/2C} \approx 1 \mu\text{V}$  on its centre conductor,

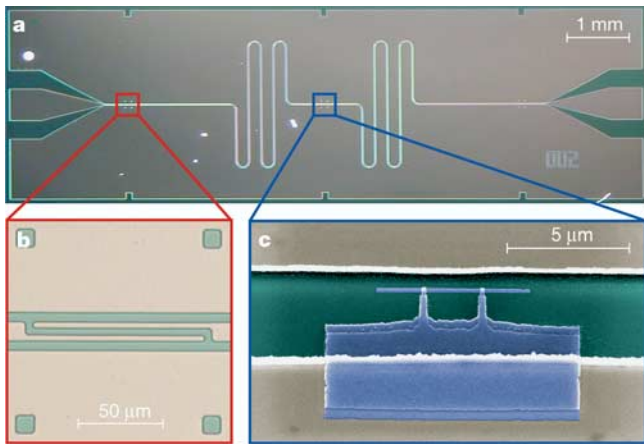


**Figure 1** Integrated circuit for cavity QED. **a**, The superconducting niobium coplanar waveguide resonator is fabricated on an oxidized  $10 \times 3$  mm<sup>2</sup> silicon chip using optical lithography. The width of the centre conductor is  $10 \mu\text{m}$  separated from the lateral ground planes extending to the edges of the chip by a gap of width  $5 \mu\text{m}$  resulting in a wave impedance of the structure of  $Z = 50 \Omega$  being optimally matched to conventional microwave components. The length of the meandering resonator is  $l = 24$  mm. It is coupled by a capacitor at each end of the resonator (see **b**) to an input and output feed line, fanning out to the edge of the chip and keeping the impedance constant. **b**, The capacitive coupling to the input and output lines and hence the coupled quality factor  $Q$  is controlled by adjusting the length and separation of the finger capacitors formed in the centre conductor. **c**, False colour electron micrograph of a Cooper pair box (blue) fabricated onto the silicon substrate (green) into the gap between the centre conductor (top) and the ground plane (bottom) of a resonator (beige) using electron beam lithography and double angle evaporation of aluminium. The Josephson tunnel junctions are formed at the overlap between the long thin island parallel to the centre conductor and the fingers extending from the much larger reservoir coupled to the ground plane.

and an electric field between the centre conductor and the ground plane that is a remarkable  $E_{\text{rms}} \approx 0.2 \text{ V m}^{-1}$ , some hundred times larger than in the three-dimensional cavities used in atomic microwave cavity QED<sup>3</sup>. The large vacuum field strength results from the extremely small effective mode volume ( $\sim 10^{-6}$  cubic wavelengths) of the resonator<sup>12</sup>.

The resonator is coupled via two coupling capacitors  $C_{\text{in/out}}$ , one at each end (see Fig. 1b), to the input and output transmission lines that allow its microwave transmission to be probed (see Fig. 2a–c). The predominant source of dissipation is the loss of photons from the resonator through these ports at a rate  $\kappa = \omega_r/Q$ , where  $Q$  is the (loaded) quality factor of the resonator. The internal (uncoupled) loss of the resonator is negligible ( $Q_{\text{int}} \approx 10^6$ ). Thus, the average photon lifetime in the resonator  $T_r = 1/\kappa$  exceeds 100 ns, even for our initial choice of a moderate quality factor  $Q \approx 10^4$ .

The Cooper pair box (CPB) consists of a several micrometre long and submicrometre wide superconducting island which is coupled via two submicrometre size Josephson tunnel junctions to a much larger superconducting reservoir, and is fabricated in the gap between the centre conductor and the ground plane of the resonator, at an antinode of the field (see Fig. 1c). The CPB is a two-state system described by the hamiltonian<sup>13</sup>  $H_a = -(E_{\text{el}}\sigma_x + E_J\sigma_z)/2$ , where  $E_{\text{el}} = 4E_C(1 - n_g)$  is the electrostatic energy and  $E_J = E_{J,\text{max}}\cos(\pi\Phi_b)$  is the Josephson energy. The overall energy scales of these terms, the charging energy  $E_C$  and the Josephson energy  $E_{J,\text{max}}$ , can be readily engineered during the fabrication by the choice of the total box capacitance and resistance respectively, and then further tuned in situ by electrical means. A gate voltage  $V_g$  applied to the input port (see Fig. 2a), induces a gate charge  $n_g = V_g C_g^*/e$  that controls  $E_{\text{el}}$ , where  $C_g^*$  is the effective capacitance between the input port of the resonator and the island of the CPB. A flux bias  $\Phi_b = \Phi/\Phi_0$ , applied with an external coil to the loop of the box, controls  $E_J$ . Denoting the ground state of the box as  $|\downarrow\rangle$  and the first excited state as  $|\uparrow\rangle$  (see Fig. 2d), we have a two-level system whose energy separation  $E_a = \hbar\omega_a$  can be widely varied as shown in Fig. 3c. Coherence of the CPB is limited by relaxation from the excited state at a rate  $\gamma_1$ , and by fluctuations of the level separation giving rise to dephasing at a rate  $\gamma_\varphi$ , for a total decoherence rate  $\gamma = \gamma_1/2 + \gamma_\varphi$  (ref. 13).

The Cooper pair box couples to photons stored in the resonator by an electric dipole interaction, via the coupling capacitance  $C_g$ . The vacuum voltage fluctuations  $V_{\text{rms}}$  on the centre conductor of the resonator change the energy of a Cooper pair on the box island by an amount  $\hbar g = dE_0 = eV_{\text{rms}}C_g/C_S$ . We have shown<sup>12</sup> that this coupled system is described by the Jaynes–Cummings hamiltonian  $H_{\text{JC}} = H_r + H_a + \hbar g(a^\dagger\sigma^- + a\sigma^+)$ , where  $\sigma^+$  ( $\sigma^-$ ) creates (annihilates) an excitation in the CPB. It describes the coherent exchange of energy between a quantized electromagnetic field and a quantum two-level system at a rate  $g/2\pi$ , which is observable if  $g$  is much larger than the decoherence rates  $\gamma$  and  $\kappa$ . This strong coupling limit<sup>3</sup>  $g > [\gamma, \kappa]$  is achieved in our experiments. When the detuning  $\Delta = \omega_a - \omega_r$  is equal to zero, the eigenstates of the coupled system are symmetric and antisymmetric superpositions of a single photon and an excitation in the CPB  $|\pm\rangle = (|0, \uparrow\rangle \pm |1, \downarrow\rangle)/\sqrt{2}$  with energies  $E_\pm = \hbar(\omega_r \pm g)$ . Although the cavity and the CPB are entangled in the eigenstates  $|\pm\rangle$ , their entangled character is not addressed in our current cavity QED experiment which spectroscopically probes the energies  $E_\pm$  of the coherently coupled system.

The strong coupling between the field in the resonator and the CPB can be used to perform a quantum nondemolition (QND) measurement of the state of the CPB in the non-resonant (dispersive) limit  $|\Delta| \gg g$ . Diagonalization of the coupled quantum system leads to the effective hamiltonian<sup>12</sup>:

$$H \approx \hbar \left( \omega_r + \frac{g^2}{\Delta} \sigma_z \right) a^\dagger a + \frac{1}{2} \hbar \left( \omega_a + \frac{g^2}{\Delta} \right) \sigma_z$$

The transition frequency  $\omega_r \pm g^2/\Delta$  is now conditioned by the qubit state  $\sigma_z = \pm 1$ . Thus, by measuring the transition frequency of the resonator, the qubit state can be determined. Similarly, the level separation in the qubit  $\hbar(\omega_a + 2a^\dagger a g^2/\Delta + g^2/\Delta)$  depends on the number of photons in the resonator. The term  $2a^\dagger a g^2/\Delta$ , linear in  $\hat{n}$ , is the alternating current (a.c.) Stark shift and  $g^2/\Delta$  is the Lamb shift. All terms in this hamiltonian, with the exception of the Lamb shift, are clearly identified in the results of our circuit QED experiments.

The properties of this coupled system are determined by probing the resonator spectroscopically<sup>12</sup>. The amplitude  $T$  and phase  $\phi$  of a microwave probe beam of power  $P_{RF}$  transmitted through the resonator are measured versus probe frequency  $\omega_{RF}$ . A simplified schematic of the microwave circuit is shown in Fig. 2a. In this setup, the CPB acts as an effective capacitance that is dependent on its  $\sigma_z$  eigenstate, the coupling strength  $g$ , and detuning  $\Delta$ . This variable capacitance changes the resonator frequency and its transmission spectrum. The transmission  $T^2$  and phase  $\phi$  of the resonator for a far-detuned qubit ( $g^2/\kappa\Delta \ll 1$ ), that is, when the qubit is effectively decoupled from the resonator, are shown in Fig. 2b and c. In this case, the transmission is a lorentzian of width  $\delta\nu_r = \nu_r/Q = \kappa/2\pi$  at  $\nu_r$ , and the phase  $\phi$  displays a corresponding step of  $\pi$ . The expected transmission at smaller detuning corresponding to a frequency shift  $\pm g^2/\Delta = \kappa$  are shown by dashed lines in Fig. 2b and c. Such small shifts in the resonator frequency are sensitively measured as a phase shift  $\phi = \pm \tan^{-1}(2g^2/\kappa\Delta)$  of the transmitted microwave at a fixed

probe frequency  $\omega_{RF}$  using beam powers  $P_{RF}$  which controllably populate the resonator with average photon numbers from  $n \approx 10^3$  down to the sub-photon level  $n \ll 1$ . We note that both the resonator and qubit can be controlled and measured using capacitive and inductive coupling only, that is, without attaching any d.c. connections to either system.

Measurements of the phase  $\phi$  versus  $n_g$  are shown in Fig. 3b, and two different cases can be identified for a Cooper pair box with Josephson energy  $E_{J,max}/\hbar > \nu_r$ . In the first case, for bias fluxes such that  $E_J(\Phi_b)/\hbar > \nu_r$ , the qubit does not come into resonance with the resonator for any value of gate charge  $n_g$  (see Fig. 3a). As a result, the measured phase shift  $\phi$  is maximum for the smallest detuning  $\Delta$  at  $n_g = 1$  and gets smaller as  $\Delta$  increases (see Fig. 3b). Moreover,  $\phi$  is periodic in  $n_g$  with a period of  $2e$ , as expected. In the second case, for values of  $\Phi_b$  resulting in  $E_J(\Phi_b)/\hbar < \nu_r$ , the qubit goes through resonance with the resonator at two values of  $n_g$ . Thus, the phase shift  $\phi$  is largest as the qubit approaches resonance ( $\Delta \rightarrow 0$ ) at the points indicated by red arrows (see Fig. 3a, b). As the qubit goes through resonance, the phase shift  $\phi$  changes sign when  $\Delta$  changes sign. This behaviour is in perfect agreement with predictions based on the analysis of the circuit QED hamiltonian in the dispersive regime.

In Fig. 3c the qubit level separation  $\nu_a = E_a/\hbar$  is plotted versus the bias parameters  $n_g$  and  $\Phi_b$ . The qubit is in resonance with the resonator at the points  $[n_g, \Phi_b]$ , indicated by the red curve in one quadrant of the plot. The measured phase shift  $\phi$  is plotted versus

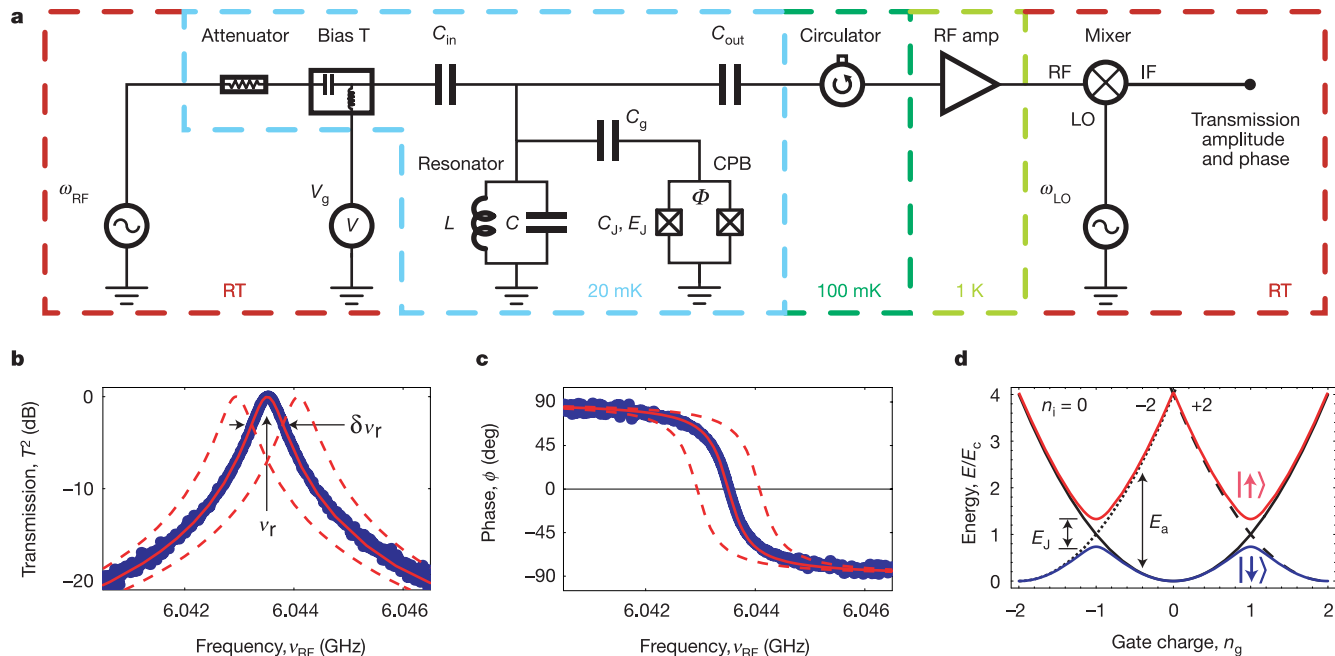


**Figure 2** Measurement scheme, resonator and Cooper pair box. **a**, The resonator with effective inductance  $L$  and capacitance  $C$  coupled through the capacitor  $C_g$  to the Cooper pair box with junction capacitance  $C_J$  and Josephson energy  $E_J$  forms the circuit QED system which is coupled through  $C_{in/out}$  to the input/output ports. The value of  $E_J$  is controllable by the magnetic flux  $\Phi$ . The input microwave at frequency  $\omega_{RF}$  is added to the gate voltage  $V_g$  using a bias-tee. After the transmitted signal at  $\omega_{RF}$  is amplified using a cryogenic high electron mobility (HEMT) amplifier and mixed with the local oscillator at  $\omega_{LO}$ , its amplitude and phase are determined. The circulator and the attenuator prevent leakage of thermal radiation into the resonator. The temperature of individual components is indicated. **b**, Measured transmission power spectrum of the resonator (blue dots), the full linewidth  $\delta\nu_r$  at half-maximum and the centre frequency  $\nu_r$  are indicated. The solid red line is a fit to a Lorentzian with  $Q = \nu_r/\delta\nu_r \approx 10^4$ . **c**, Measured transmission phase  $\phi$  (blue dots) with fit (red line). In panels **b** and **c** the dashed lines are theory curves shifted by

$\pm \delta\nu_r$  with respect to the data. **d**, Energy level diagram of a Cooper pair box. The electrostatic energy  $E_c(n_i - n_g)^2$ , with charging energy  $E_c = e^2/2C_\Sigma$ , is indicated for  $n_i = 0$  (solid black line),  $-2$  (dotted line) and  $+2$  (dashed line) excess electrons forming Cooper pairs on the island.  $C_\Sigma$  is the total capacitance of the island given by the sum of the capacitances  $C_J$  of the two tunnel junctions, the coupling capacitance  $C_g$  to the centre conductor of the resonator and any stray capacitances. In the absence of Josephson tunnelling the states with  $n_i$  and  $n_i + 2$  electrons on the island are degenerate at  $n_g = 1$ . The Josephson coupling mediated by the weak link formed by the tunnel junctions between the superconducting island and the reservoir lifts this degeneracy and opens up a gap proportional to the Josephson energy  $E_J = E_{J,max} \cos(\pi\Phi_b)$ , where  $E_{J,max} = \hbar\Delta_{Al}/8e^2R_J$ , with the superconducting gap of aluminium  $\Delta_{Al}$  and the tunnel junction resistance  $R_J$ . A ground-state band  $|\downarrow\downarrow\rangle$  and an excited-state band  $|\uparrow\uparrow\rangle$  are formed with a gate charge and flux-bias-dependent energy level separation of  $E_a$ .

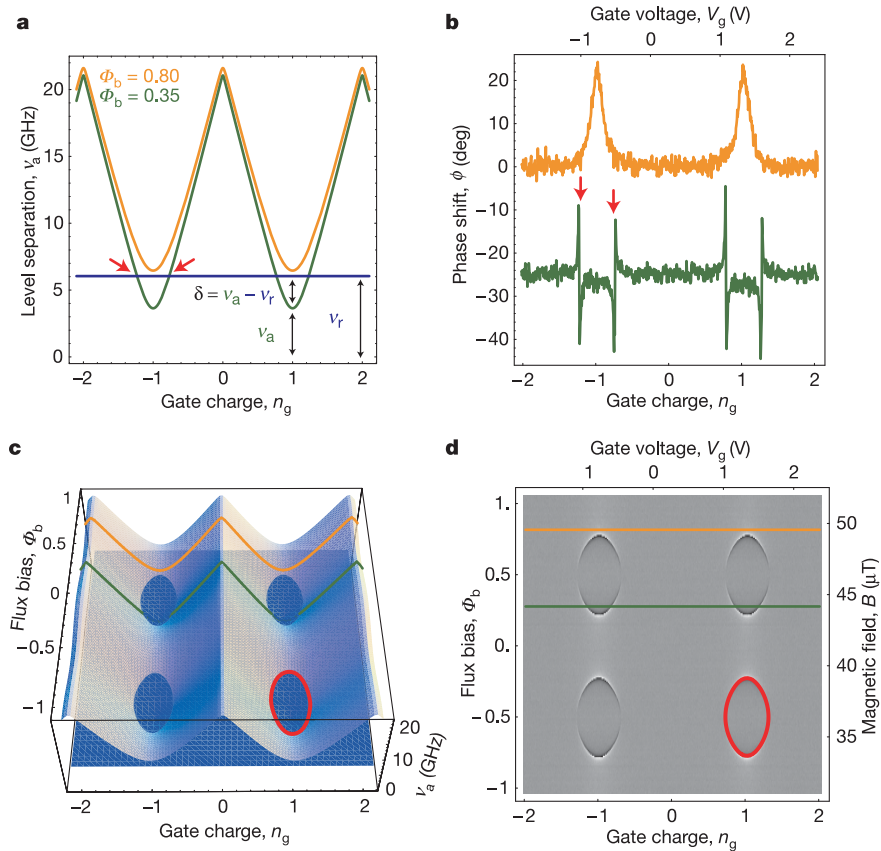


**Figure 3** Strong coupling circuit QED in the dispersive regime. **a**, Calculated level separation  $\nu_a = \omega_a/2\pi = E_a/h$  between ground  $|\downarrow\rangle$  and excited state  $|\uparrow\rangle$  of qubit for two values of flux bias  $\Phi_b = 0.8$  (orange line) and  $\Phi_b = 0.35$  (green line). The resonator frequency  $\nu_r = \omega_r/2\pi$  is shown by a blue line. Resonance occurs at  $\nu_a = \nu_r$  symmetrically around degeneracy  $n_g = \pm 1$ ; also see red arrows. The detuning  $\Delta/2\pi = \delta = \nu_a - \nu_r$  is indicated. **b**, Measured phase shift  $\phi$  of the transmitted microwave for values of  $\Phi_b$  in **a**. Green curve is offset by  $-25$  deg for visibility. **c**, Calculated qubit level separation  $\nu_a$  versus bias parameters  $n_g$  and  $\Phi_b$ . The resonator frequency  $\nu_r$  is indicated by the blue plane. At the intersection, also indicated by the red

curve in the lower right-hand quadrant, resonance between the qubit and the resonator occurs ( $\delta = 0$ ). For qubit states below the resonator plane the detuning is  $\delta < 0$ , above  $\delta > 0$ . **d**, Density plot of measured phase shift  $\phi$  versus  $n_g$  and  $\Phi_b$ . Light colours indicate positive  $\phi$  ( $\delta > 0$ ), dark colours negative  $\phi$  ( $\delta < 0$ ). The red line is a fit of the data to the resonance condition  $\nu_a = \nu_r$ . In **c** and **d**, the line cuts presented in **a** and **b** are indicated by the orange and the green line, respectively. The microwave probe power  $P_{RF}$  used to acquire the data is adjusted such that the maximum intra-resonator photon number  $n$  at  $\nu_r$  is about ten for  $g^2/\kappa\Delta \ll 1$ . The calibration of the photon number has been performed in situ by measuring the a.c.-Stark shift of the qubit levels.

both  $n_g$  and  $\Phi_b$  in Fig. 3d. We observe the expected periodicity in flux bias  $\Phi_b$  with one flux quantum  $\Phi_0$ . The set of parameters  $[n_g, \Phi_b]$  for which the resonance condition is met is marked by a sudden sign change in  $\phi$ , which allows a determination of the Josephson energy  $E_{J,max} = 8.0 (\pm 0.1)$  GHz and the charging energy  $E_C = 5.2 (\pm 0.1)$  GHz.

These data clearly demonstrate that the properties of the qubit can be determined in a transmission measurement of the resonator and that full in situ control over the qubit parameters is achieved. We note that in the dispersive regime this new read-out scheme for the Cooper pair box is most sensitive at charge degeneracy ( $n_g = 1$ ), where the qubit is to first order decoupled from  $1/f$  fluctuations in its charge environment, which minimizes dephasing<sup>6</sup>. This property is advantageous for quantum control of the qubit at  $n_g = 1$ , a point where traditional electrometry, using a single electron transistor (SET) for example<sup>27</sup>, is unable to distinguish the qubit states. We note that this dispersive QND measurement of the qubit state<sup>12</sup> is the complement of the atomic microwave cavity QED measurement in which the state of the cavity is inferred non-destructively from the phase shift in the state of a beam of atoms sent through the cavity<sup>3,28</sup>.

Making use of the full control over the qubit hamiltonian, we then tune the flux bias  $\Phi_b$  so that the qubit is at  $n_g = 1$  and in resonance with the resonator. Initially, the resonator and the qubit are cooled into their combined ground state  $|0, \downarrow\rangle$ ; see inset in

Fig. 4b. Owing to the coupling, the first excited states become a doublet  $|\pm\rangle$ . Similarly to ref. 4, we probe the energy splitting of this doublet spectroscopically using a weak probe beam so that  $n \ll 1$ . The intra-resonator photon number,  $n$ , is calibrated by measuring the a.c.-Stark shift of the qubit in the dispersive case. The resonator transmission  $T^2$  is first measured for large detuning  $\Delta$  with a probe beam populating the resonator with a maximum of  $n \approx 1$  at resonance; see Fig. 4a. From the lorentzian line the photon decay rate of the resonator is determined as  $\kappa/2\pi = 0.8$  MHz. The probe beam power is subsequently reduced by 5 dB and the transmission spectrum  $T^2$  is measured in resonance ( $\Delta = 0$ ); see Fig. 4b. We clearly observe two well-resolved spectral lines separated by the vacuum Rabi frequency  $\nu_{Rabi} \approx 11.6$  MHz. The individual lines have a width determined by the average of the photon decay rate  $\kappa$  and the qubit decoherence rate  $\gamma$ . The data are in excellent agreement with the transmission spectrum numerically calculated using the given value  $\kappa/2\pi = 0.8$  MHz and the single adjustable parameter  $\gamma/2\pi = 0.7$  MHz.

The transmission spectrum shown in Fig. 4b is highly sensitive to the photon number in the cavity. The measured transmission spectrum is consistent with the expected thermal photon number of  $n \leq 0.06$  ( $T < 100$  mK); see red curve in Fig. 4b. Owing to the anharmonicity of the coupled atom-cavity system in the resonant case, an increased thermal photon number would reduce trans-

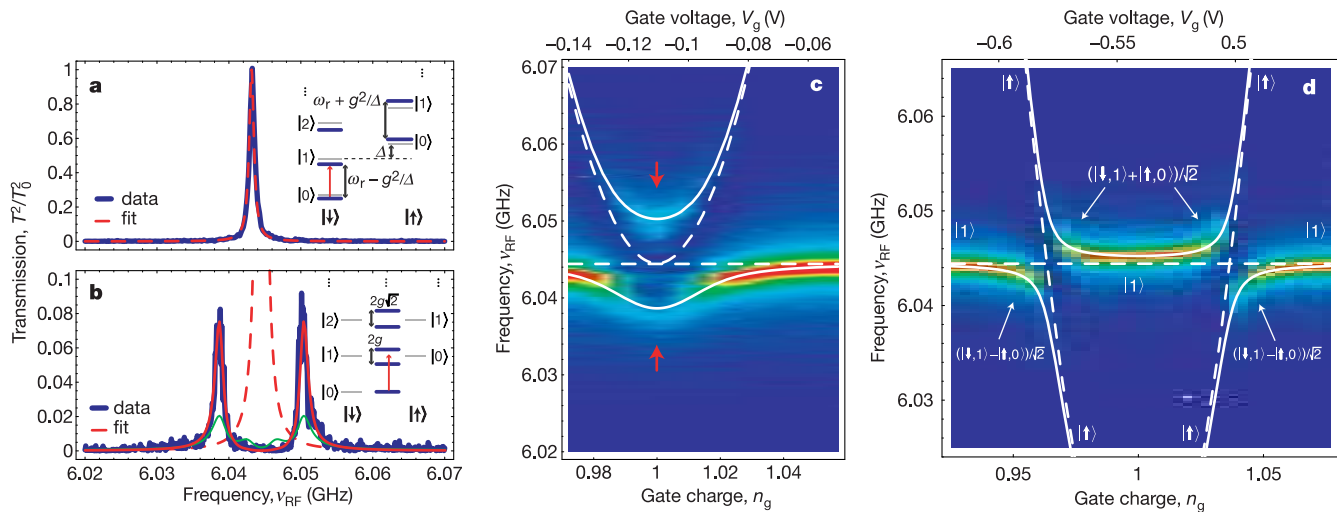


**Figure 4** Vacuum Rabi mode splitting. **a**, Measured transmission  $T^2$  (blue line) versus microwave probe frequency  $\nu_{\text{RF}}$  for large detuning ( $g^2/\Delta\kappa \ll 1$ ) and fit to Lorentzian (dashed red line). The peak transmission amplitude is normalized to unity. The inset shows the dispersive dressed states level diagram. **b**, Measured transmission spectrum for the resonant case  $\Delta = 0$  at  $n_g = 1$  (blue line) showing the vacuum Rabi mode splitting compared to numerically calculated transmission spectra (red and green lines) for thermal photon numbers of  $n = 0.06$  and  $0.5$ , respectively. The dashed red line is the calculated transmission for  $g = 0$  and  $\kappa/2\pi = 0.8$  MHz. The inset shows the resonant dressed

states level diagram. **c**, Resonator transmission amplitude  $T$  plotted versus probe frequency  $\nu_{\text{RF}}$  and gate charge  $n_g$  for  $\Delta = 0$  at  $n_g = 1$ . Blue colour corresponds to small  $T$ , red colour to large  $T$ . Dashed lines are uncoupled qubit level separation  $\nu_a$  and resonator resonance frequency  $\nu_r$ . Solid lines are level separations found from exact diagonalization of  $H_{\text{JC}}$ . Spectrum shown in **b** corresponds to line cut along red arrows. **d**, As in **c**, but for  $E_J/h < \nu_r$ . The dominant character of the corresponding eigenstates is indicated.

mission and give rise to additional peaks in the spectrum owing to transitions between higher excited doublets<sup>30</sup>. The transmission spectrum calculated for a thermal photon number of  $n = 0.5$  (see green curve in Fig. 4b) is clearly incompatible with our experimental data, indicating that the coupled system has in fact cooled to near its ground state, and that we measure the coupling of a single qubit to a single photon. The nonlinearity of the cavity QED system is also observed at higher probe beam powers, as transitions are driven between states higher up the dressed state ladders (not shown).

We also observe the anti-crossing between the single photon resonator state and the first excited qubit state by tuning the qubit into and out of resonance with a gate charge near  $n_g = 1$  and measuring the transmission spectrum (see Fig. 4c). The vacuum Rabi peaks evolve from a state with equal weight in the photon and qubit at  $n_g = 1$  (as shown in Fig. 4b) to predominantly photon states for  $n_g \gg 1$  or  $n_g \ll 1$ . The observed peak positions agree well with calculations considering the qubit with level separation  $\nu_a$ , a single photon in the resonator with frequency  $\nu_r$  and a coupling strength of  $g/2\pi$ ; see solid lines in Fig. 4c. For a different value of flux bias  $\Phi_b$  such that  $E_a/h < \nu_r$  at  $n_g = 1$ , two anti-crossings are observed (see Fig. 4d) again in agreement with theory.

The observation of the vacuum Rabi mode splitting and the corresponding avoided crossings demonstrates that the strong coupling limit of cavity QED has been achieved, and that coherent superpositions of a single qubit and a single photon can be generated on a superconducting chip. This opens up many new possibilities for quantum optical experiments with circuits. Possible applications include using the cavity as a quantum bus to couple widely separated qubits in a quantum computer, or as a quantum memory to store quantum information, or even as a generator and detector of single microwave photons for quantum communication. □

Received 11 June; accepted 12 July 2004; doi:10.1038/nature02851.

1. Walls, D. & Milburn, G. *Quantum Optics* (Springer, Berlin, 1994).
2. Mabuchi, H. & Doherty, A. Cavity quantum electrodynamics: Coherence in context. *Science* **298**, 1372–1377 (2002).
3. Raimond, J., Brune, M. & Haroche, S. Manipulating quantum entanglement with atoms and photons in a cavity. *Rev. Mod. Phys.* **73**, 565–582 (2001).

4. Thompson, R. J., Rempe, G. & Kimble, H. J. Observation of normal-mode splitting for an atom in an optical cavity. *Phys. Rev. Lett.* **68**, 1132–1135 (1992).
5. Nakamura, Y., Pashkin, Y. A. & Tsai, J. S. Coherent control of macroscopic quantum states in a single-Cooper-pair box. *Nature* **398**, 786–788 (1999).
6. Vion, D. *et al.* Manipulating the quantum state of an electrical circuit. *Science* **296**, 886–889 (2002).
7. Martinis, J. M., Nam, S., Aumentado, J. & Urbina, C. Rabi oscillations in a large Josephson-junction qubit. *Phys. Rev. Lett.* **89**, 117901 (2002).
8. Chiorescu, I., Nakamura, Y., Harmans, C. J. P. M. & Mooij, J. E. Coherent quantum dynamics of a superconducting flux qubit. *Science* **299**, 1869–1871 (2003).
9. Yamamoto, T., Pashkin, Y. A., Astafiev, O., Nakamura, Y. & Tsai, J. S. Demonstration of conditional gate operation using superconducting charge qubits. *Nature* **425**, 941–944 (2003).
10. Berkley, A. J. *et al.* Entangled macroscopic quantum states in two superconducting qubits. *Science* **300**, 1548–1550 (2003).
11. Bouchiat, V., Vion, D., Joyez, P., Esteve, D. & Devoret, M. H. Quantum coherence with a single Cooper pair. *Phys. Scr.* **T76**, 165–170 (1998).
12. Blais, A., Huang, R.-S., Wallraff, A., Girvin, S. & Schoelkopf, R. Cavity quantum electrodynamics for superconducting electrical circuits: an architecture for quantum computation. *Phys. Rev. A* **69**, 062320 (2004).
13. Makhlin, Y., Schön, G. & Shnirman, A. Quantum-state engineering with Josephson-junction devices. *Rev. Mod. Phys.* **73**, 357–400 (2001).
14. Buisson, O. & Hekking, F. in *Macroscopic Quantum Coherence and Quantum Computing* (eds Averin, D. V., Ruggiero, B. & Silvestrini, P.) (Kluwer, New York, 2001).
15. Marquardt, F. & Bruder, C. Superposition of two mesoscopically distinct quantum states: Coupling a Cooper-pair box to a large superconducting island. *Phys. Rev. B* **63**, 054514 (2001).
16. Al-Saidi, W. A. & Stroud, D. Eigenstates of a small Josephson junction coupled to a resonant cavity. *Phys. Rev. B* **65**, 014512 (2001).
17. Plastina, F. & Falcì, G. Communicating Josephson qubits. *Phys. Rev. B* **67**, 224514 (2003).
18. Blais, A., Maassen van den Brink, A. & Zagoskin, A. Tunable coupling of superconducting qubits. *Phys. Rev. Lett.* **90**, 127901 (2003).
19. Yang, C.-P., Chu, S.-I. & Han, S. Possible realization of entanglement, logical gates, and quantum-information transfer with superconducting-quantum-interference-device qubits in cavity QED. *Phys. Rev. A* **67**, 042311 (2003).
20. You, J. Q. & Nori, F. Quantum information processing with superconducting qubits in a microwave field. *Phys. Rev. B* **68**, 064509 (2003).
21. Kiraz, A. *et al.* Cavity-quantum electrodynamics using a single InAs quantum dot in a microdisk structure. *Appl. Phys. Lett.* **78**, 3932–3934 (2001).
22. Childress, L., Sørensen, A. S. & Lukin, M. D. Mesoscopic cavity quantum electrodynamics with quantum dots. *Phys. Rev. A* **69**, 042302 (2004).
23. Irish, E. K. & Schwab, K. Quantum measurement of a coupled nanomechanical resonator–Cooper-pair box system. *Phys. Rev. B* **68**, 155311 (2003).
24. Weisbuch, C., Nishioka, M., Ishikawa, A. & Arakawa, Y. Observation of the coupled exciton-photon mode splitting in a semiconductor quantum microcavity. *Phys. Rev. Lett.* **69**, 3314–3317 (1992).
25. Vucokovic, J., Fattal, D., Santori, C., Solomon, G. S. & Yamamoto, Y. Enhanced single-photon emission from a quantum dot in a micropost microcavity. *Appl. Phys. Lett.* **82**, 3596 (2003).
26. Day, P. K., LeDuc, H. G., Mazin, B. A., Vayonakis, A. & Zmuidzinas, J. A broadband superconducting detector suitable for use in large arrays. *Nature* **425**, 817–821 (2003).
27. Lehnert, K. *et al.* Measurement of the excited-state lifetime of a microelectronic circuit. *Phys. Rev. Lett.* **90**, 027002 (2003).

28. Noguez, G. *et al.* Seeing a single photon without destroying it. *Nature* **400**, 239–242 (1999).  
 29. Schuster, D. I. *et al.* AC-Stark shift and dephasing of a superconducting qubit strongly coupled to a cavity field. Preprint at <http://www.arXiv.org/cond-mat/0408367> (2004).  
 30. Rau, I., Johansson, G. & Shnirman, A. Cavity QED in superconducting circuits: susceptibility at elevated temperatures. Preprint at <http://www.arXiv.org/cond-mat/0403257> (2004).

**Acknowledgements** We thank J. Teufel, B. Turek and J. Wyatt for their contributions to the project and are grateful to P. Day, D. DeMille, M. Devoret, S. Weinreb and J. Zmuidzinas for numerous conversations. This work was supported in part by the National Security Agency and Advanced Research and Development Activity under the Army Research Office, the NSF, the David and Lucile Packard Foundation, the W. M. Keck Foundation, and the Natural Science and Engineering Research Council of Canada.

**Competing interests statement** The authors declare that they have no competing financial interests.

**Correspondence** and requests for materials should be addressed to A. W. ([andreas.wallraff@yale.edu](mailto:andreas.wallraff@yale.edu)).

## Generation of ultraviolet entangled photons in a semiconductor

Keiichi Edamatsu<sup>1,2</sup>, Goro Oohata<sup>1,3</sup>, Ryosuke Shimizu<sup>2</sup> & Tadashi Itoh<sup>4,2</sup>

<sup>1</sup>Research Institute of Electrical Communication, Tohoku University, Sendai 980-8577, Japan

<sup>2</sup>CREST, Japan Science and Technology Agency (JST), Japan

<sup>3</sup>ERATO Semiconductor Spintronics Project, JST, Japan

<sup>4</sup>Graduate School of Engineering Science, Osaka University, Toyonaka 560-8531, Japan

Entanglement is one of the key features of quantum information and communications technology. The method that has been used most frequently to generate highly entangled pairs of photons<sup>1,2</sup> is parametric down-conversion. Short-wavelength entangled photons are desirable for generating further entanglement between three or four photons, but it is difficult to use parametric down-conversion to generate suitably energetic entangled photon pairs. One method that is expected to be applicable for the generation of such photons<sup>3</sup> is resonant hyper-parametric scattering (RHPS): a pair of entangled photons is generated in a semiconductor via an electronically resonant third-order nonlinear optical process. Semiconductor-based sources of entangled photons would also be advantageous for practical quantum technologies, but attempts to generate entangled photons in semiconductors have not yet been successful<sup>4,5</sup>. Here we report experimental evidence for the generation of ultraviolet entangled photon pairs by means of biexciton resonant RHPS in a single crystal of the semiconductor CuCl. We anticipate that our results will open the way to the generation of entangled photons by current injection, analogous to current-driven single photon sources<sup>6,7</sup>.

The material we used in this study was copper chloride (CuCl) single crystal. Because CuCl has a large bandgap (~3.4 eV), it is suitable for generating photon pairs in the short wavelength region near ultraviolet. Furthermore, the material has large binding energies for the exciton (~200 meV) and biexciton (~30 meV). These characteristics have made CuCl one of the most thoroughly investigated materials on the physics of excitons and biexcitons (ref. 8 and references therein). In particular, the ‘giant oscillator strength’ in the two-photon excitation of the biexciton results in a large increase in RHPS efficiency, which is advantageous for our experiment. In fact the RHPS in CuCl has been observed since the 1970s (refs 8, 9 and ref. 10 and references therein). Figure 1a schematically shows the RHPS process in resonance to the biexciton state. The two pump (parent) photons (frequency  $\omega_i$ ) resonantly create the

biexciton, and are converted into the two scattered (daughter) photons ( $\omega_s, \omega_s'$ ). The biexciton state ( $\Gamma_1$ ) created in this process has zero angular momentum ( $J = 0$ ), so we expected the polarizations of the daughter photons to be entangled so that their total angular momentum is also zero. With this expectation in mind, we note that polarization correlation between two classical pump beams has been known since the early 1980s (ref. 11). In practice, instead of the oversimplified picture in Fig. 1a, we must consider the exciton-polariton picture; the RHPS obeys the phase-matching condition that takes into account the polariton dispersion relation<sup>8</sup>. The RHPS in this case is also called two-photon resonant polariton scattering or spontaneous hyper-Raman scattering. In this process, shown in Fig. 1b, the biexciton is created from a pair of parent photons (polaritons, more accurately). The sum of the parent photons’ energies matches the biexciton energy. The biexciton progressively coherently decays into two polaritons, the sum of whose photon energies, as well as the sum of momenta, is conserved as that of the biexciton. Although the RHPS in CuCl has been known for decades, the possibility of generating entangled photons by this process was theoretically pointed out only lately<sup>12</sup>. In addition, a large parametric gain via the biexcitonic resonance in CuCl was reported recently<sup>13</sup>. Similar stimulated parametric scattering of polaritons has also been observed in semiconductor microcavities, even at high temperatures<sup>14</sup>.

In the present experiment, we used a vapour-phase-grown thin single crystal of CuCl. Figure 2 presents the schematic drawing of our experimental set-up and Fig. 3 shows the spectrum of light emitted from the sample. The large peak at the downward arrow in Fig. 3 is the Rayleigh scattered light of the pump beam that was tuned to the two-photon excitation resonance of the biexciton. The two peaks indicated by LEP and HEP (lower and higher energy polaritons) on either side of the pump beam originate from the RHPS. The RHPS is very efficient (a few orders of magnitude higher than that of typical parametric down-conversion): We got of the order of  $10^{10}$  photons  $s^{-1} sr^{-1}$  by using pump light of ~2 mW. A pair of photons, one from LEP and the other from HEP, is emitted into different directions according to the phase-matching condition, so we placed two optical fibres at appropriate positions and led each photon within the pair into two independent monochromators followed by two photomultipliers (PMTs). A time-interval analyser recorded the time interval ( $\tau$ ) between the detected

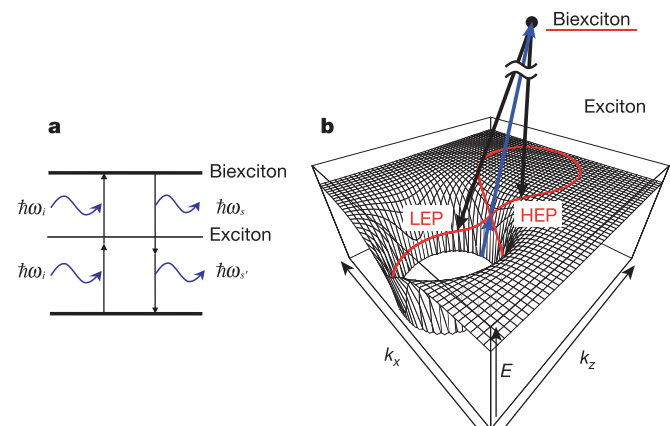


**Figure 1** Schematic diagram of the resonant hyper-parametric scattering (RHPS) via biexciton. **a**, Two pump (parent) photons of frequency  $\omega_i$  are converted to the two scattered (daughter) photons ( $\omega_s, \omega_s'$ ). **b**, The polariton dispersion drawn in two dimensions of momentum space. The biexciton decays into two polaritons that satisfy the phase-matching condition so that both energy and momentum are conserved. The red curve on the polariton-dispersion surface indicates the states on which the phase-matching condition can be satisfied.

## ac Stark Shift and Dephasing of a Superconducting Qubit Strongly Coupled to a Cavity Field

D. I. Schuster, A. Wallraff, A. Blais, L. Frunzio, R.-S. Huang,\* J. Majer, S. M. Girvin, and R. J. Schoelkopf

*Departments of Applied Physics and Physics, Yale University, New Haven, Connecticut 06520, USA*

(Received 16 August 2004; published 30 March 2005)

We have performed spectroscopy of a superconducting charge qubit coupled nonresonantly to a single mode of an on-chip resonator. The strong coupling induces a large ac Stark shift in the energy levels of both the qubit and the resonator. The dispersive shift of the resonator frequency is used to nondestructively determine the qubit state. Photon shot noise in the measurement field induces qubit level fluctuations leading to dephasing which is characteristic for the measurement backaction. A crossover in line shape with measurement power is observed and theoretically explained. For weak measurement a long intrinsic dephasing time of  $T_2 > 200$  ns of the qubit is found.

DOI: 10.1103/PhysRevLett.94.123602

PACS numbers: 42.50.Pq, 32.60.+i, 42.50.Lc, 85.35.Gv

The investigation of strong coupling between a single quantum two-level system and a single photon, as first realized in atomic cavity quantum electrodynamics (CQED) [1], is not only at the forefront of research in quantum optics and atomic physics [2] but also has great prospects in the realm of quantum information processing [3] where realizing entanglement between qubits and photons is essential for quantum communication. Recently, it has been proposed [4] and demonstrated for the first time in a solid state system that strong coupling CQED [5,6] can be realized in superconducting quantum circuits [7]. Following these results, strong coupling has also been achieved in a second solid state system, namely, semiconducting quantum dots embedded in microcavities [8,9]. In this Letter we demonstrate the use of *nonresonant (dispersive)* strong coupling between a Cooper pair box (CPB) [10] and a coherent microwave field in a high quality transmission line resonator to measure the quantum mechanical state of the Cooper pair box in a quantum nondemolition (QND) scheme [4,11,12]. The interaction between the Cooper pair box and the measurement field containing  $n$  photons on average gives rise to a large ac Stark shift of the qubit energy levels, analogous to the one observed in CQED [13], demonstrated here for the first time in superconducting qubits. As a consequence of the strong coupling, quantum fluctuations in  $n$  induce a broadening of the transition linewidth, which represents the backaction of the measurement on the qubit.

In our circuit QED architecture [4] [see Fig. 1(a)] a split Cooper pair box [10], modeled by the two-level Hamiltonian  $H_a = -1/2(E_{el}\sigma_x + E_J\sigma_z)$  [14], is coupled capacitively to the electromagnetic field of a full wave ( $l = \lambda$ ) transmission line resonator, described by a harmonic oscillator Hamiltonian  $H_r = \hbar\omega_r(a^\dagger a + 1/2)$ . In the Cooper pair box, the energy difference  $E_a = \hbar\omega_a = (E_{el}^2 + E_J^2)^{1/2}$  between the ground state  $|\downarrow\rangle$  and the first excited state  $|\uparrow\rangle$  [see Fig. 1(b)], is determined by its electrostatic energy  $E_{el} = 4E_C(1 - n_g)$  and its Josephson coupling energy  $E_J = E_{J,max} \cos(\pi\Phi_b)$ . Here,  $E_C = e^2/2C_\Sigma \approx 5$  GHz is the charging energy given by the total

box capacitance  $C_\Sigma$ ,  $n_g = C_g^*V_g/e$  is the gate charge controlled by the gate voltage  $V_g$  applied through a gate with effective capacitance  $C_g^*$ , and  $E_{J,max} \approx 8$  GHz is the maximum Josephson coupling energy of the two junctions which is modulated by applying a flux bias  $\Phi_b = \Phi/\Phi_0$  to the loop of the split box [see Fig. 1(a)].  $\Phi_0 = 2e/h$  is the magnetic flux quantum. Near its resonance frequency  $\omega_r = 1/\sqrt{LC} \approx 2\pi \cdot 6$  GHz, the resonator is accurately modeled as a harmonic oscillator with lumped inductance  $L$  and capacitance  $C$ .

In the presence of strong mutual coupling between the qubit and the resonator [5], their *dressed* excitation ener-

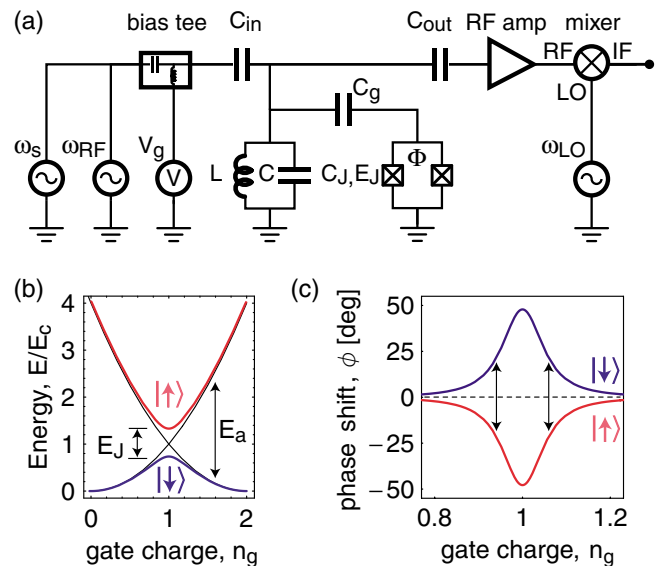


FIG. 1 (color online). (a) Simplified circuit diagram of measurement setup. The phase  $\phi$  and amplitude  $T$  of a microwave at  $\omega_{rf}$  transmitted through the resonator, amplified, and mixed down to an intermediate frequency  $\omega_{IF} = \omega_{rf} - \omega_{LO}$  using a local oscillator at  $\omega_{LO}$  is measured. An additional spectroscopy microwave at  $\omega_s$  is applied to the input port of the resonator. (b) Ground  $|\downarrow\rangle$  and excited  $|\uparrow\rangle$  state energy levels of CPB vs gate charge  $n_g$ . (c) Calculated phase shift  $\phi$  in ground and excited states vs  $n_g$  for  $\Delta_{a,r}/2\pi = 100$  MHz.

gies  $\tilde{\omega}_a$  and  $\tilde{\omega}_r$ , are modified from their bare values  $\omega_a$  and  $\omega_r$ . For large detuning  $\Delta_{a,r} = \omega_a - \omega_r$  the dressed energy levels are determined by the Hamiltonian [4]

$$H \approx \hbar \left( \omega_r + \frac{g^2}{\Delta_{a,r}} \sigma_z \right) a^\dagger a + \frac{1}{2} \hbar \left( \omega_a + \frac{g^2}{\Delta_{a,r}} \right) \sigma_z, \quad (1)$$

where  $g/2\pi \approx 5.8$  MHz is the coupling strength between a single photon and the qubit [5]. In this nonresonant case, the dressed resonator frequency  $\tilde{\omega}_r = \omega_r \pm g^2/\Delta_{a,r}$  depends on the qubit state  $\sigma_z = \pm 1$  and the detuning  $\Delta_{a,r}$ . The qubit state can thus be inferred from the phase shift  $\phi$  that a probe microwave transmitted through the resonator at frequency  $\omega_{rf}$  experiences because of the interaction with the qubit [4,5]. In Fig. 1(c), the expected phase shift  $\phi = \pm \tan^{-1}(2g^2/\kappa\Delta_{a,r})$ , where  $\kappa = \omega_r/Q$  is the decay rate of photons from the resonator with quality factor  $Q \approx 10^4$ , is plotted versus gate charge  $n_g$ .  $\phi$  is maximum at  $n_g = 1$  where the detuning  $\Delta_{a,r}$  is smallest and falls off as the detuning is increased with increasing  $n_g$ . Moreover,  $\phi$  has opposite signs in the ground  $|\downarrow\rangle$  and excited  $|\uparrow\rangle$  states of the CPB.

Qubit state transitions can be driven by applying an additional microwave of frequency  $\omega_s$ , detuning  $\Delta_{s,a} = \omega_s - \tilde{\omega}_a$ , and power  $P_s$  to the input port of the resonator [see Fig. 1(a)]. On resonance ( $\Delta_{s,a} = 0$ ) and for a continuous (cw) large amplitude spectroscopy drive, the qubit transition saturates and the populations in the excited and the ground states approach 1/2. In this case, the measured phase shift of the probe beam at  $\omega_{rf}$  is expected to saturate at  $\phi = 0$  [see Fig. 1(c)]. By sweeping the spectroscopy frequency  $\omega_s$  and the gate charge  $n_g$  and *continuously* measuring  $\phi$ , we have mapped out the energy level separation

$\tilde{\omega}_a$  of the qubit (see Fig. 2). In the lower panel of Fig. 2(a), the measured phase shift  $\phi$  is shown for the nonresonant case, where  $\omega_s < \tilde{\omega}_a$  for all values of gate charge  $n_g$ . The measured phase shift is, as expected, a continuous curve similar to the one shown in Fig. 1(c). In the middle panel of Fig. 2(a), the spectroscopy microwave at  $\nu_s = \omega_s/2\pi = 6.15$  GHz is in resonance with the qubit at  $n_g = 1$ , populating the excited state and thus inducing a dip in the measured phase shift  $\phi$  around  $n_g = 1$ , as expected. Note that, as predicted [4], our measurement scheme has the advantage of being most sensitive at charge degeneracy, a bias point where traditional electrometry, using a radio frequency single electron transistor [15], for example, is unable to distinguish the qubit states.

When  $\nu_s$  is increased to higher values, resonance with the qubit occurs for two values of  $n_g$  situated symmetrically around  $n_g = 1$ , leading to two symmetric dips in  $\phi$  [see upper panel of Fig. 2(a)]. From the  $[n_g, \nu_s]$  positions of the spectroscopic lines in the measured phase  $\phi$ , the Josephson energy  $E_J = 6.2$  GHz and the charging energy  $E_C = 4.8$  GHz are determined in a fit using the full qubit Hamiltonian beyond the two-level approximation [14] [see density plot of  $\phi$  vs  $n_g$  and  $\nu_s$  in Fig. 2(b)]. In this experiment the flux bias  $\Phi_b$  has been chosen to result in a minimum detuning of about  $\Delta_{a,r}/2\pi \approx 100$  MHz at  $n_g = 1$ . The tunability of  $E_J$  (i.e., the detuning at charge degeneracy) has been demonstrated previously [5]. It is also worth noting that the spectroscopy frequency  $\omega_s$  typically remains strongly detuned ( $\Delta_{s,r} = \omega_s - \omega_r > 2\pi 100$  MHz) from the resonator, such that a large fraction of the spectroscopy photons are reflected at the input port and only a small number  $n_s$ , determined by the Lorentzian line shape of the resonator, populates the resonator.

Various other radio or microwave frequency qubit readout schemes have been developed recently [15–17]. In a related experiment, the level separation of a split Cooper pair box coupled *inductively* to a *low frequency, moderate Q* tank circuit has been determined spectroscopically [18].

The width and the saturation level of the spectroscopic lines discussed above depend sensitively on the power  $P_s$  of the spectroscopic drive. Both quantities are related to the excited state population

$$P_\uparrow = 1 - P_\downarrow = \frac{1}{2} \frac{n_s \omega_{\text{vac}}^2 T_1 T_2}{1 + (T_2 \Delta_{s,a})^2 + n_s \omega_{\text{vac}}^2 T_1 T_2}, \quad (2)$$

found from the Bloch equations in steady state [19], where  $\omega_{\text{vac}} = 2g$  is the vacuum Rabi frequency,  $n_s$  the average number of spectroscopy photons in the resonator,  $T_1$  the relaxation time, and  $T_2$  the dephasing time of the qubit. We have extracted the transition linewidth and saturation from spectroscopy frequency scans for different drive powers  $P_s$  with the qubit biased at charge degeneracy ( $n_g = 1$ ). We observe that the spectroscopic lines have a Lorentzian line shape with width and depth in accordance with Eq. (2). The

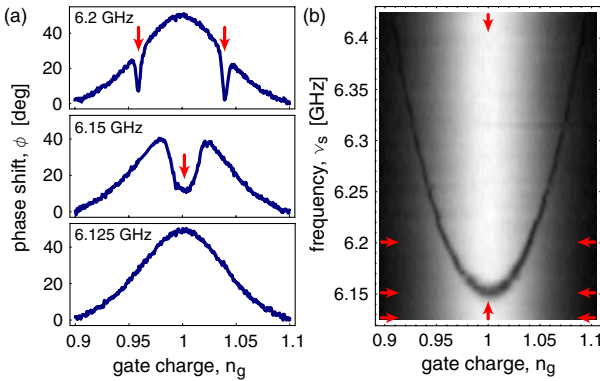


FIG. 2 (color online). (a) Probe microwave phase shift  $\phi$  vs gate charge  $n_g$  at spectroscopy frequency  $\nu_s = 6.125$  GHz (lower panel), 6.15 GHz (middle panel), and 6.2 GHz (upper panel). (b) Density plot of  $\phi$  vs  $n_g$  and  $\nu_s$ ; white (black) corresponds to large (small) phase shift. Horizontal arrows indicate line cuts shown in (a); vertical arrows indicate line cuts shown in Fig. 4(a). Measurements in (a) and (b) were performed populating the resonator with  $n \sim 25$  photons on average.

half width at half maximum (HWHM) of the line is found to follow the expected power dependence  $2\pi\delta\nu_{\text{HWHM}} = 1/T_2' = (1/T_2^2 + n_s\omega_{\text{vac}}^2 T_1/T_2)^{1/2}$  [19], where the input microwave power  $P_s$  is proportional to  $n_s\omega_{\text{vac}}^2$  [see Fig. 3(a)]. In the low power limit ( $n_s\omega_{\text{vac}}^2 \rightarrow 0$ ), the unbroadened linewidth is found to be small,  $\delta\nu_{\text{HWHM}} \approx 750$  kHz, corresponding to a long dephasing time of  $T_2 > 200$  ns at  $n_g = 1$ , where the qubit is only second order sensitive to charge fluctuations limiting the dephasing time in this sample. At a larger drive, the width increases proportionally to the drive amplitude. The depth of the spectroscopic dip at resonance ( $\Delta_{s,a} = 0$ ) reflects the probability of the qubit to be in the excited state  $P_\uparrow$  and depends on  $P_s$  as predicted by Eq. (2) [see Fig. 3(b)]. At low drive the population increases linearly with  $P_s$  and then approaches 0.5 for large  $P_s$ . From time resolved measurements (data not shown),  $T_1$  is found to be on the order of a few microseconds, a value which is much shorter than that expected for radiative decay of the qubit in the cavity [4], indicating the existence of other, possibly non-radiative decay channels.

In the above we have demonstrated that the strong coupling of the qubit to the radiation field modifies the resonator transition frequency in a way that can be exploited to measure the qubit state. Correspondingly, the resonator acts back onto the qubit through their mutual strong coupling. Regrouping the terms of the Hamiltonian in Eq. (1) one sees that the *dressed* qubit level separation is given by  $\tilde{\omega}_a = \omega_a + 2ng^2/\Delta_{a,r} + g^2/\Delta_{a,r}$ , where we note that the resonator gives rise to an ac Stark shift of the qubit levels of  $\pm ng^2/\Delta_{a,r}$ , proportional to the intracavity photon number  $n = \langle a^\dagger a \rangle$ , as well as a Lamb shift  $\pm g^2/2\Delta_{a,r}$ , due to the coupling to the vacuum fluctuations. The ac Stark shift is measured spectroscopically at  $n_g = 1$  for fixed power  $P_s$  by varying the probe beam power  $P_{\text{rf}}$  which changes the average measurement photon number  $n$  in the resonator (see Fig. 4). We observe that the qubit level

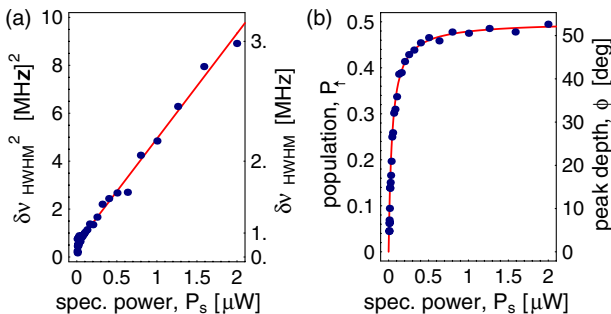


FIG. 3 (color online). (a) Measured qubit linewidth  $\delta\nu_{\text{HWHM}}$  vs input spectroscopy power  $P_s$  (solid circles) with fit (solid line). Probe beam power  $P_{\text{rf}}$  is adjusted such that  $n < 1$ . (b) Measured peak depth  $\phi$  and excited state population probability  $P_\uparrow$  on resonance  $\Delta_{s,a} = 0$  vs  $P_s$  (solid circles) with fit (solid line).

separation  $\tilde{\nu}_a = \tilde{\omega}_a/2\pi$  is linear in  $P_{\text{rf}}$  [see Fig. 5(a)], i.e., that the ac Stark shift  $\nu_{\text{ac}} = 2ng^2/2\pi\Delta_{a,r}$  is linear in the photon number  $n$ , as expected. In the limit of  $P_{\text{rf}} \rightarrow 0$  ( $n \rightarrow 0$ ), the bare qubit level separation  $\omega_a + g^2/\Delta_{a,r} = 2\pi \cdot 6.15$  GHz is determined, where  $g^2/\Delta_{a,r}$  is the small Lamb shift which cannot be separated from  $\omega_a$  in our current experiments. Knowing the coupling constant  $g$  from an independent measurement of the vacuum Rabi mode splitting [5] and  $\Delta_{a,r}$  from spectroscopic measurements in the  $n \rightarrow 0$  limit, the dependence of the intracavity photon number  $n$  on the input power  $P_{\text{rf}}$  is determined from the measured ac Stark shift  $\nu_{\text{ac}}$ . We find that an input microwave power of  $P_{\text{rf}} = -29$  dBm corresponds to  $n = 1$  which is consistent with an intended attenuation of approximately 105 dB in the input coaxial line. The ac Stark shift of the qubit at this particular detuning is a remarkable 0.6 MHz per photon in the cavity and is comparable to the linewidth. Using this method, the intracavity photon number was calibrated to a precision of  $\sim \pm 1$  dB for the vacuum Rabi mode splitting measurements presented in Ref. [5].

Quantum fluctuations (photon shot noise)  $\delta n$  around the average photon number  $n$  of the coherent field populating the resonator give rise to random fluctuations in the qubit transition frequency due to the ac Stark shift. This leads to measurement-induced dephasing, and thus to a broadening of the qubit linewidth (see Figs. 4 and 5). This is the measurement backaction and can be understood quantitatively by considering the relative phase  $\varphi(t) = 2g^2/\Delta_{a,r} \int_0^t dt' \delta n(t')$  accumulated in time between the ground and the excited states of the qubit. Following Ref. [4], the measurement-induced phase decay of the qubit is then characterized by

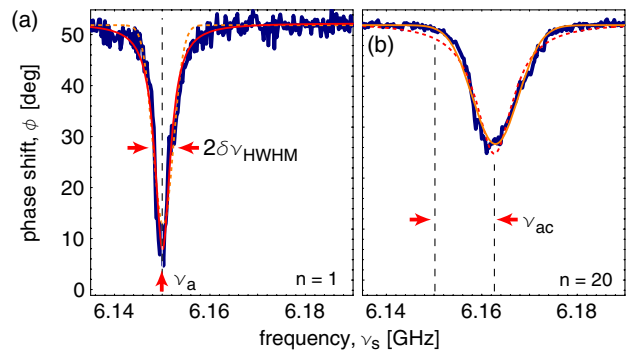


FIG. 4 (color online). Measured spectroscopic lines (wide lines with noise) at (a) intracavity photon number  $n \approx 1$  ( $P_{\text{rf}} = -30$  dBm) with fit to Lorentzian line shape (solid line) and at (b)  $n \approx 20$  ( $P_{\text{rf}} = -16$  dBm) with fit to Gaussian line shape (solid line). Dashed lines are best fits to (a) Gaussian or (b) Lorentzian line shapes, respectively. The qubit transition frequency  $\nu_a$  at low  $P_{\text{rf}}$ , the half width half maximum  $\delta\nu_{\text{HWHM}}$ , and the ac Stark shift  $\nu_{\text{ac}}$  of the lines are indicated.

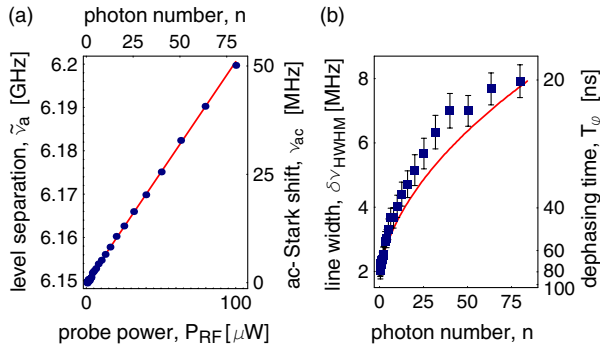


FIG. 5 (color online). (a) Measured qubit level separation  $\tilde{\nu}_a$  and fit (solid line) vs input microwave probe power  $P_{rf}$ . The ac Stark shift  $\nu_{ac}$  and the intracavity photon number  $n$  extracted from the fit are also indicated. (b) Measurement broadened qubit linewidth  $\delta\nu_{\text{HWHM}}$  vs  $n$ . Error bars are reflecting estimated systematic uncertainties in the extracted linewidth. The corresponding total dephasing time  $T_\varphi = 1/2\pi\delta\nu_{\text{HWHM}}$  is also indicated. The solid line is obtained from Eq. (4) with a spectroscopy power broadened  $T_2' \approx 80$  ns.

$$\langle e^{i\varphi(t)} \rangle = \exp \left[ -\frac{2g^4}{\Delta_{a,r}^2} \iint_0^t dt_1 dt_2 \langle \delta n(t_1) \delta n(t_2) \rangle \right], \quad (3)$$

where the fluctuations  $\delta n$  are assumed to be Gaussian. In the above expression, the photon correlation function  $\langle \delta n(t) \delta n(0) \rangle = n \exp(-\kappa|t|/2)$  of the coherent probe beam in the resonator is governed by the cavity decay rate  $\kappa$  and physically represents the white photon shot noise filtered by the cavity response. The spectroscopic line shape  $S(\omega)$  is obtained from the Fourier transform of  $\langle \exp[i\varphi(t)] \rangle e^{-t/T_2'}$ , where  $1/T_2'$  takes into account dephasing mechanisms independent of the measurement

$$S(\omega) = \frac{1}{\pi} \sum_{j=0}^{\infty} \frac{(-4\chi)^j}{j!} \frac{1/T_2' + 2\kappa\chi + j\kappa/2}{(\omega - \tilde{\omega}_a)^2 + (1/T_2' + 2\kappa\chi + j\kappa/2)^2}. \quad (4)$$

The form of the line shape depends on the dimensionless parameter  $\chi = n\theta_0^2$ , where  $\theta_0 = 2g^2/\kappa\Delta_{a,r}$  is the transmission phase shift describing the strength of the measurement. For small  $\chi$  the measurement rate is slow compared to  $\kappa$  and the phase diffuses in a random walk  $\langle \varphi(t)^2 \rangle \sim 4\theta_0^2 n \kappa t$ , leading to a homogeneously broadened Lorentzian line of HWHM of  $2\theta_0^2 n \kappa + 1/T_2'$ . For large  $\chi$ , i.e., strong measurement, the measurement rate exceeds  $\kappa$  leading to a qubit transition frequency which depends on the instantaneous value of the cavity photon number and hence to an inhomogeneously broadened Gaussian line [see Fig. 4(b)], whose variance is simply  $\sqrt{n}$  multiplied by the Stark shift per photon. The full crossover from intrinsic Lorentzian line shape with width  $\propto n$  at small  $n$  to Gaussian line shape with width  $\propto \sqrt{n}$  at large  $n$  as described by Eq. (4) with no adjustable parameters is in good agreement with the measured dependence of the linewidth on  $n$  [see Fig. 5(b)]. The slightly increased measured linewidth could be attributed

to fluctuations (e.g., charge noise) activated at high photon numbers and to the nonlinearity of the ac Stark shift above the critical photon number [4]. We note that this effect is not seen in Fig. 4(a) because of compensation by the change of the cavity pull at large  $n$  from the zero-photon limit  $g^2/\Delta$ .

In our experiments we have demonstrated that the strong coupling of a Cooper pair box to a nonresonant microwave field in an on-chip cavity gives rise to a large qubit dependent shift in the excitation energy of the resonator. The ac Stark effect shifts the qubit level separation by about one linewidth per photon at 2% detuning, and the backaction of the fluctuations in the field gives rise to a large broadening of the qubit line. Good agreement of the line shape with theory indicates that the dispersive measurement is QND, as expected.

We thank M. Devoret and I. Chiorescu for discussions. This work was supported in part by NSA and ARDA under ARO Contract No. DAAD19-02-1-0045, and the NSF under Grants No. ITR-0325580 and No. DMR-0342157, the David and Lucile Packard Foundation, the W. M. Keck Foundation, and the NSERC of Canada.

\*Also at Ames Laboratory, Iowa State University, Ames, IA 50011, USA.

- [1] H. Mabuchi and A. Doherty, *Science* **298**, 1372 (2002).
- [2] D. Walls and G. Milburn, *Quantum Optics* (Springer-Verlag, Berlin, 1994).
- [3] M. A. Nielsen and I. L. Chuang, *Quantum Computation and Quantum Information* (Cambridge University Press, Cambridge, U.K., 2000).
- [4] A. Blais *et al.*, *Phys. Rev. A* **69**, 062320 (2004).
- [5] A. Wallraff *et al.*, *Nature (London)* **431**, 162 (2004).
- [6] I. Chiorescu *et al.*, *Nature (London)* **431**, 159 (2004).
- [7] Y. Nakamura, Y. A. Pashkin, and J. S. Tsai, *Nature (London)* **398**, 786 (1999); D. Vion *et al.*, *Science* **296**, 886 (2002); J. M. Martinis, S. Nam, J. Aumentado, and C. Urbina, *Phys. Rev. Lett.* **89**, 117901 (2002); Y. Yu *et al.*, *Science* **296**, 889 (2002); I. Chiorescu, Y. Nakamura, C. J. P. M. Harmans, and J. E. Mooij, *Science* **299**, 1869 (2003); T. Yamamoto *et al.*, *Nature (London)* **425**, 941 (2003).
- [8] T. Yoshie *et al.*, *Nature (London)* **432**, 200 (2004).
- [9] J. P. Reithmaier *et al.*, *Nature (London)* **432**, 197 (2004).
- [10] V. Bouchiat *et al.*, *Phys. Scr.* **T76**, 165 (1998).
- [11] P. Grangier, J. A. Levenson, and J.-P. Poziat, *Nature (London)* **396**, 537 (1998).
- [12] G. Nogues *et al.*, *Nature (London)* **400**, 239 (1999).
- [13] P. Brune *et al.*, *Phys. Rev. Lett.* **72**, 3339 (1994).
- [14] Y. Makhlin, G. Schön, and A. Shnirman, *Rev. Mod. Phys.* **73**, 357 (2001).
- [15] K. Lehnert *et al.*, *Phys. Rev. Lett.* **90**, 027002 (2003).
- [16] A. Lupascu *et al.*, *Phys. Rev. Lett.* **93**, 177006 (2004).
- [17] I. Siddiqi *et al.*, *Phys. Rev. Lett.* **93**, 207002 (2004).
- [18] D. Born *et al.*, *Phys. Rev. B* **70**, 180501 (2004).
- [19] A. Abragam, *The Principles of Nuclear Magnetism* (Oxford University Press, Oxford, 1961).

# Fabrication and Characterization of Superconducting Circuit QED Devices for Quantum Computation

Luigi Frunzio, Andreas Wallraff, David Schuster, Johannes Majer, and Robert Schoelkopf

**Abstract**—We present fabrication and characterization procedures of devices for circuit quantum electrodynamics (cQED). We have made 3-GHz cavities with quality factors in the range  $10^4$ – $10^6$ , which allow access to the strong coupling regime of cQED. The cavities are transmission line resonators made by photolithography. They are coupled to the input and output ports via gap capacitors. An Al-based Cooper pair box is made by e-beam lithography and Dolan bridge double-angle evaporation in superconducting resonators with high quality factor. An important issue is to characterize the quality factor of the resonators. We present an RF-characterization of superconducting resonators as a function of temperature and magnetic field. We have realized different versions of the system with different box-cavity couplings by using different dielectrics and by changing the box geometry. Moreover, the cQED approach can be used as a diagnostic tool of qubit internal losses.

**Index Terms**—Distributed parameter circuits, Q factor, scattering parameters measurement, superconducting cavity resonators.

## I. INTRODUCTION

WE have recently demonstrated that a superconducting quantum two-level system can be strongly coupled to a single microwave photon [1], [2]. The strong coupling between a quantum solid state circuit and an individual photon, analogous to atomic cavity quantum electrodynamics (CQED) [3], has previously been envisaged by many authors, see [4] and references therein. Our circuit quantum electrodynamics architecture [4], in which a superconducting charge qubit, the Cooper pair box (CPB) [5], is coupled strongly to a coplanar transmission line resonator, has great prospects both for performing quantum optics experiments [6] in solids and for realizing elements for quantum information processing [7] with superconducting circuits [8]–[14] and also for other architectures [15], [16].

In developing these qubit-resonator systems, one key ingredient is to design and realize transmission line resonators with high internal quality factor,  $Q_{\text{int}}$ , and with resonant frequency,  $\nu_o$ , in the 5–15 GHz range to match the other energy scales of our device, and to be in the quantum regime ( $h\nu_o \gg k_B T$ ) at  $T = 30$  mK. On the other hand, the resonator is loaded with input and output capacitances and we need a loaded quality

factor  $Q_L \approx 10^4$  in order to obtain reasonably fast rate of measurement,  $\kappa = \nu_o/Q_L \approx 1$  MHz.

In fabricating the transmission line resonator, we opted for a coplanar waveguide (CPW) for many different reasons. First, a CPW has a simple layer structure with no need for deposited insulators. Second, it has a balanced structure with a relatively easy planar connection to the CPB. Third, a CPW has a  $\nu_o$  that is relatively insensitive to kinetic inductance and dominated by geometrical distributed inductance. Last but not the least, CPW-based structures, made by Al thin film deposited on sapphire, have been recently shown [17] to allow very high  $Q$ 's (order of  $10^6$ ).

We decided to fabricate on passivated Si wafers because this is the substrate on which we had previously developed the qubit fabrication. We also decided to try as material for the resonators both Al, for easy compatibility with the qubit process, and Nb, because its higher critical temperature allows testing of resonators at higher temperatures.

In Section II, we present design consideration for devices for circuit quantum electrodynamics (cQED). We will show that we can engineer  $Q$  with different coupling of the resonator to the input and output ports and that the internal losses can be made negligible at the designed  $Q$  [1], [2]. Section III introduces the fabrication procedures for both the resonator and the CPB. Sections IV–VI present an RF-characterization of the superconducting transmission line resonators versus temperature and magnetic field.

## II. CIRCUIT DESIGN

A picture of a  $10 \times 3$  mm<sup>2</sup> chip containing a 3-GHz superconducting Nb CPW resonator is shown in Fig. 1(a). The length of the meandering resonator is  $2l = 4$  mm. The center conductor is  $10 \mu\text{m}$  wide, separated from the lateral ground planes extending to the edges of the chip by a  $5 \mu\text{m}$  gap, resulting in a wave impedance of the coplanar waveguide of  $Z = 50 \Omega$  to match the impedance of conventional microwave components. The capacitance per unit length is  $C_s \approx 0.13$  fF/ $\mu\text{m}^2$  which gives a total resonator capacitance of  $C = C_s l/2 = 1.6$  pF. The resonator is coupled by identical capacitors at each end (see solid line square in Fig. 1(a)) to an input and output feed line, fanning out to the edge of the chip and keeping the impedance constant. In Fig. 1(b) and (1d) are shown micrographs of two of the coupling capacitors with different geometries. The one in Fig. 1(b) consists of two  $100\text{-}\mu\text{m}$  long and  $4\text{-}\mu\text{m}$  wide fingers separated by a  $2\text{-}\mu\text{m}$  gap. It has a capacitance,  $C_{\kappa,b} \approx 6$  fF, larger than that in Fig. 1(d), which has a simpler geometry with a  $4\text{-}\mu\text{m}$  gap and  $C_{\kappa,d} \approx 0.3$  fF.

Manuscript received October 4, 2004. This work was supported in part by the National Security Agency (NSA) and Advanced Research and Development Activity (ARDA) under Army Research Office (ARO) Contract DAAD19-02-1-0045, the NSF ITR Program under Grant DMR-0325580, the NSF under Grant DMR-0342157, the David and Lucile Packard Foundation, and the W. M. Keck Foundation.

The authors are with the Department of Applied Physics, Yale University, New Haven, CT 06520 USA (e-mail: luigi.frunzio@yale.edu).

Digital Object Identifier 10.1109/TASC.2005.850084

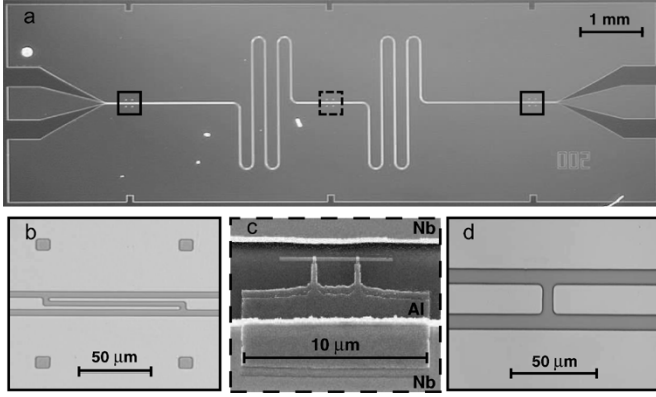


Fig. 1. Picture of a device for circuit QED. (a) The 3 GHz superconducting coplanar waveguide resonator is fabricated using optical lithography. The length of the meandering resonator is  $l = 24$  mm. The center conductor is  $10 \mu\text{m}$  wide, separated from the lateral ground planes extending to the edges of the chip by a  $5 \mu\text{m}$  gap. The resonator is coupled by identical capacitors at each end (solid line squares) to input and output ports. (b) Micrograph of a coupling capacitance with two  $100 \mu\text{m}$  long and  $4 \mu\text{m}$  wide fingers separated by a  $2 \mu\text{m}$  gap. (c) Scanning electron micrograph of a Cooper pair box fabricated onto the silicon substrate into the gap between the center conductor (top) and the ground plane (bottom) in the center of a resonator (dashed line square) using electron beam lithography and double angle evaporation of aluminum. (d) Micrograph of a coupling capacitance with a  $4 \mu\text{m}$  gap.

The capacitive coupling to the input and output lines, together with the loading impedance,  $R_L = 50 \Omega$ , are very important in determining the loaded quality factor  $Q_L$ , defined by

$$\frac{1}{Q_L} = \frac{1}{Q_{\text{int}}} + \frac{1}{Q_{\text{ext}}} \quad (1)$$

where the external quality factor is

$$Q_{\text{ext}} = \frac{\omega C}{G_{\text{ext}}} \quad (2)$$

with

$$G_{\text{ext}} = \frac{2R_L C_\kappa^2 \omega^2}{1 + R_L^2 C_\kappa^2 \omega^2}. \quad (3)$$

There are two possible regimes for the resonator. It can be undercoupled when  $C_\kappa$  is small (like  $C_{\kappa,d}$ ) and then  $Q_L \approx Q_{\text{int}}$ . This is the regime in which it is possible to measure  $Q_{\text{int}}$ . Otherwise, the resonator can be overcoupled when  $C_\kappa$  is large (like  $C_{\kappa,b}$ ) and then  $Q_L \approx Q_{\text{ext}}$ . It is then possible to engineer the  $Q_L$  to obtain fast measurement with  $\kappa$  much larger than the qubit decay rates [1], [2].

In Fig. 1(c) an electron micrograph of a Cooper pair box is shown. The CPB consists of a  $7\text{-}\mu\text{m}$  long and  $200\text{-nm}$  wide superconducting island parallel to the center conductor which is coupled via two  $200 \times 100 \text{ nm}^2$  size Josephson tunnel junctions to a much larger superconducting reservoir. The CPB is fabricated onto the silicon substrate [see dashed line square in Fig. 1(a)] in the gap between the center conductor (top) and the ground plane (bottom) at an antinode of the electric field in the resonator. The Josephson junctions are formed at the overlap between the island and the fingers extending from the reservoir, which is capacitively coupled to the ground plane. The CPB is a two-state system described by the Hamiltonian  $H =$

$-(E_{el}\sigma_x + E_J\sigma_z)/2$  where  $E_{el}$  is the electrostatic energy and  $E_J = E_{J,max} \cos(\pi\Phi_b)$  is the Josephson energy. The overall energy scales of these terms, the charging energy  $E_{el}$  and the Josephson energy  $E_{J,max}$ , can be readily engineered during the fabrication by the choice of the total box capacitance and resistance respectively, and then further tuned *in situ* by electrical means. A flux bias  $\Phi_b = \Phi/\Phi_o$ , applied with an external coil to the loop of the box, controls  $E_J$ . We have demonstrated that changing the length of the CPB island and its distance to the center conductor and changing the dielectrics (removing the passivation step of the Si substrate), we can obtain stronger couplings of qubit and resonator as predicted by simple electrostatic calculations of the capacitances.

### III. DEVICE FABRICATION

The pattern of 36 different Nb resonators is generated exposing a bilayer photoresist (600 nm LOR5A and  $1.2 \mu\text{m}$  S1813) through a mask with traditional UV photolithography. Then a  $200\text{-nm}$  thick Nb film is dc magnetron sputtered in Ar at  $1.5 \text{ Pa}$  with a rate of  $1 \text{ nm/s}$  in an UHV system with a base pressure of  $20 \mu\text{Pa}$ . The substrate is a  $2''$   $300\text{-}\mu\text{m}$  thick p-doped (Boron) (100) oriented Si wafer with resistivity  $\rho > 1000 \Omega\text{cm}$  previously passivated by thermal wet oxidation with a  $470\text{-nm}$  thick layer of  $\text{SiO}_2$ . A lift-off process in NMP followed by ultrasonic agitation completes the resonator fabrication.

Al resonators are fabricated on the same type of substrate depositing a  $200\text{-nm}$  thick Al film by thermal evaporation at a rate of  $1 \text{ nm/s}$  in the same UHV system. Then the same mask is used to expose a single photoresist layer ( $1.2 \mu\text{m}$  S1813) and then realized by wet etching ( $8 : 4 : 1 : 1 = \text{H}_3\text{PO}_4 : \text{CH}_3\text{COOH} : \text{HNO}_3 : \text{H}_2\text{O}$ ) the metal.

In both cases, chips containing individual resonators are obtained by dicing the Si wafer. The CPB qubit [Fig. 1(c)] is then fabricated on an individual resonator by a simple Dolan bridge technique [18] exposing a bilayer resist (500 nm MMA-(8.5)MAA EL13 and  $100 \text{ nm}$  950 K PMMA A3) by e-beam lithography and then e-beam evaporating Al ( $35 \text{ nm}$  for the base and  $70 \text{ nm}$  for the top electrode) at a rate of  $1 \text{ nm/s}$  in a double-angle UHV system with a base pressure of  $20 \mu\text{Pa}$ . The junction barrier is realized with a  $12 \text{ min}$  thermal oxidation in a  $400 \text{ Pa}$  of  $\text{O}_2$ . A lift-off process in hot acetone and ultrasonic agitation complete the device. To couple the qubit reservoir to ground with a large capacitance, the base electrode is deposited with a little angle taking advantage of the shadow of the thicker Nb film to define the capacitor.

### IV. MEASUREMENT TECHNIQUE

The frequency dependence of the transmission through the resonators<sup>1</sup> was measured using a vector network analyzer. The equivalent circuit of the measurement setup is shown in the inset of Fig. 3. The sample was mounted on a PC board in a closed copper sample box (Fig. 2) equipped with blind mate SMP connectors that launch the microwaves onto the PC board CPW's. The sample was cooled to temperatures ranging from

<sup>1</sup>The transmission is measured in  $\text{dB} = 10 \log |V_2/V_1|^2$ , where  $V_2$  is the voltage measured at the input port of the analyzer and  $V_1$  is the voltage applied at the output port of the analyzer.

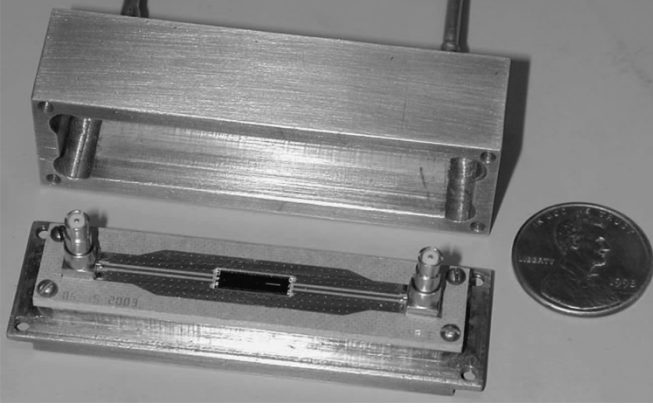


Fig. 2. Picture of the copper sample box containing a resonator mounted on the PC board.

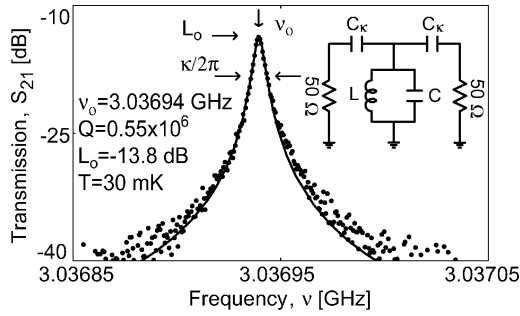


Fig. 3. Measured transmission power spectrum of an undercoupled resonator. The solid line is a fit to a Lorentzian line.

the critical temperature,  $T_c$  of the superconducting films down to  $T = 30$  mK.

The transmission  $S_{21}$  through the resonator around its fundamental resonant frequency  $\nu_o$  is shown in Fig. 3 at  $T = 30$  mK. The curve was acquired using a  $-60$  dBm input power<sup>2</sup> and a room temperature amplifier. The input power was lowered until no distortion of the resonance curve due to excessive input power could be observed. The network analyzer was response calibrated ( $S_{21}$ ) up to the input and output ports of the cryostat and the absorption of the cabling in the cryostat was determined to be approximately  $-7$  dB in a calibrated  $S_{11}$  and  $S_{22}$  reflection measurement. The quality factor of the resonator is determined by fitting a Lorentzian line to the measured power spectrum as shown by the solid line in Fig. 3. This is the power spectrum of an undercoupled resonator and from the fit we have extracted  $\nu_o = 3.03694$  GHz. At this frequency the insertion loss is  $L_o = -13.8$  dB. The quality factor is determined from the full width at half max of the fitted power spectrum and is found to be  $Q_L \approx Q_{\text{int}} = \nu_o/2\delta\nu_o = 2\pi\nu_o/\kappa = 0.55 \times 10^6$ .

## V. TEMPERATURE DEPENDENCE OF $Q$ AND $\nu_o$

In Fig. 4, we show the measured temperature dependence of the quality factor  $Q$  for an undercoupled resonator (solid dots) and an overcoupled one (open dots). The lines in Fig. 4 are generated by summing a  $Q_{\text{int}}$  that scales exponentially with the reduced temperature,  $T_c/T$ , in parallel with a constant  $Q_{\text{ext}}$ . At

<sup>2</sup>The input power is in dBm where  $-60$  dBm =  $20 \log(1 \mu\text{W}/1 \text{ mW})$ .

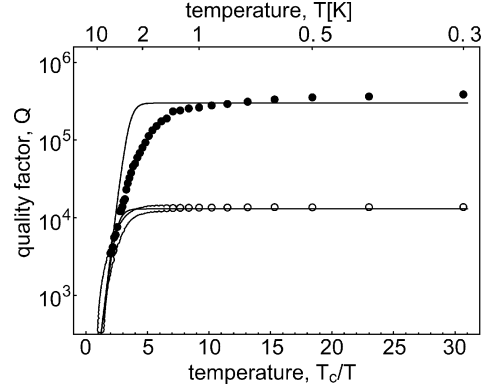


Fig. 4. Temperature dependence of the quality factor  $Q$  of two 3 GHz superconducting Nb coplanar waveguide resonators at their first harmonic resonant frequency (6 GHz). Solid dots are data collected on a undercoupled resonator and open dots are from an overcoupled one. The lines are generated by summing a  $Q_{\text{int}}$  that scales exponentially with the reduced temperature,  $T_c/T$ , in parallel with a constant  $Q_{\text{ext}}$ .

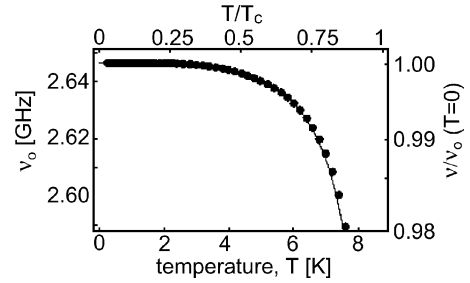


Fig. 5. Temperature dependence of the resonant frequency  $\nu_o$  of a superconducting Nb coplanar waveguide resonator. Solid line is a fit to a kinetic inductance model.

low temperature, the coupling saturates the  $Q$  of the overcoupled resonator, while it seems that  $Q$  for the undercoupled one has still some weak temperature dependence whose nature is still unknown. We speculate that either vortices or losses in the dielectrics could limit the  $Q$  of this resonator but neither of these interpretations offer an easy understanding of the weak temperature dependence.

We have observed a shift of the resonant frequency  $\nu_o$  with temperature as shown in Fig. 5, which can be understood in terms of the temperature dependent kinetic inductance of the resonator [17], [19].  $\nu_o$  is proportional to  $1/\sqrt{L}$ , where the total inductance of the resonator  $L$  is the sum of the temperature independent geometric inductance  $L_m$  and the temperature dependent kinetic inductance  $L_k$ . The kinetic inductance scales as  $L_k \propto \lambda_L(T)^2$ , where  $\lambda_L(T)$  is the temperature dependent London penetration depth. The best fit in Fig. 4 was achieved for a ratio  $L_k/L_m \approx 4\%$  and a critical temperature of  $T_c \approx 8.75$  K, which we have independently measured on a test sample fabricated on the same wafer.

## VI. MAGNETIC FIELD DEPENDENCE OF $Q$

As explained in Section II, we need to apply a magnetic field perpendicular to the qubit loop in order to tune  $E_J$ . Then, we measured the quality factor of two resonators as a function of the magnetic field at  $T = 300$  mK, as shown in Fig. 6. It is evident that the Nb film (upper part) is less sensitive to the applied

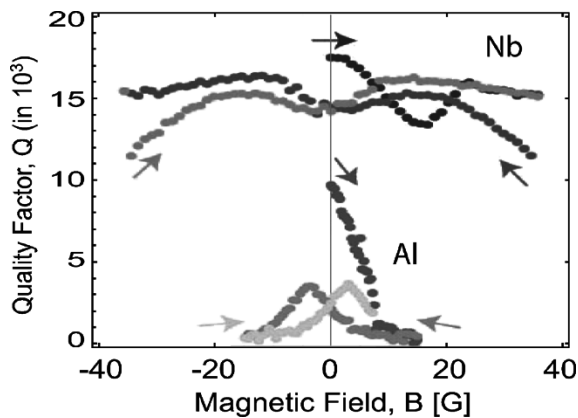


Fig. 6. Magnetic field dependence of the quality factor  $Q$  of two different superconducting coplanar waveguide resonators at  $T = 300$  mK. In the upper part data refer to a Nb resonator, while in the lower part they refer to an Al resonator. Arrows indicate the direction in which the magnetic field was swept in both case starting from zero.

field than the Al film (lower part). In both cases there seems to be a reproducible and irreversible hysteretic behavior that can be reset by thermal cycling the sample. In our recent works [1], [2] we have observed a focusing effect on the magnetic field such that the effective field in the gap of the resonator was approximately two orders of magnitude larger than the applied magnetic field. We believe that the hysteretic phenomena could be in fact a result of vortices being trapped in the resonator film due to these large effective fields.

## VII. CONCLUSION

In summary, we have designed and fabricated devices for realizing a circuit quantum electrodynamics architecture in which a qubit can be strongly coupled to a single microwave photon. We have shown that we can engineer  $Q$  with different coupling of the resonator to the input and output ports and that the internal losses can be made negligible at the designed  $Q$ . Indeed, we have achieved high  $Q = 0.55 \times 10^6$  in the undercoupled CPW resonators and  $Q \approx 10^4$  in the overcoupled ones, which allow fast measurement of the qubit.

To help determine the mechanism of the losses, one can fabricate resonators on different substrates [Si with different resistivity, sapphire,  $\text{Si}_3\text{N}_4$ ], or in different superconductors (Ta, Al). In fact, quality factor measurements in this type of resonant circuits serve as a sensitive probe of material losses in dielectrics and superconductors in the GHz frequency range at millikelvin temperatures. These presently unknown properties may in fact pose a serious limit for all superconducting qubits, though the large internal  $Q$ 's already observed are highly encouraging. Better knowledge of the material losses, and tech-

niques to characterize them, may be crucial not only for future improvements of circuit QED devices, but also for designing and realizing robust, long-lived superconducting qubits.

## REFERENCES

- [1] A. Wallraff, D. Schuster, A. Blais, L. Frunzio, R.-S. Huang, J. Majer, S. Kumar, S. Girvin, and R. Schoelkopf, "Strong coupling of a single photon to a superconducting qubit using circuit quantum electrodynamics," *Nature*, vol. 431, pp. 162–167, 2004.
- [2] D. Schuster, A. Wallraff, A. Blais, L. Frunzio, R.-S. Huang, J. Majer, S. M. Girvin, and R. J. Schoelkopf, "AC-Stark shift and dephasing of a superconducting qubit strongly coupled to a cavity field," *Phys. Rev. Lett.*, to be published.
- [3] H. Mabuchi and A. Doherty, "Cavity quantum electrodynamics: Coherence in context," *Science*, vol. 298, pp. 1372–1377, 2002.
- [4] A. Blais, R.-S. Huang, A. Wallraff, S. Girvin, and R. Schoelkopf, "Cavity quantum electrodynamics for superconducting electrical circuits: an architecture for quantum computation," *Phys. Rev. A*, vol. 69, p. 062 320, 2004.
- [5] V. Bouchiat, D. Vion, P. Joyez, D. Esteve, and M. H. Devoret, "Quantum coherence with a single Cooper pair," *Physica Scripta*, vol. T76, pp. 165–170, 1998.
- [6] D. Walls and G. Milburn, *Quantum Optics*. Berlin, Germany: Springer-Verlag, 1994.
- [7] M. A. Nielsen and I. L. Chuang, *Quantum Computation and Quantum Information*. Cambridge, U.K.: Cambridge Univ. Press, 2000.
- [8] Y. Nakamura, Y. A. Pashkin, and J. S. Tsai, "S. Coherent control of macroscopic quantum states in a single-Cooper-pair box," *Nature*, vol. 398, pp. 786–788, 1999.
- [9] D. Vion, A. Aassime, A. Cottet, P. Joyez, H. Pothier, C. Urbina, D. Esteve, and M. H. Devoret, "Manipulating the quantum state of an electrical circuit," *Science*, vol. 296, pp. 886–889, 2002.
- [10] J. M. Martinis, S. Nam, J. Aumentado, and C. Urbina, "Rabi oscillations in a large Josephson-junction qubit," *Phys. Rev. Lett.*, vol. 89, p. 117 901, 2002.
- [11] Y. Yu, S. Han, X. Chu, S.-I. Chu, and Y. Wang, "Coherent temporal oscillations of macroscopic quantum states in a Josephson junction," *Science*, vol. 296, pp. 889–892, 2002.
- [12] I. Chiorescu, Y. Nakamura, C. J. P. M. Harmans, and J. E. Mooij, "Coherent quantum dynamics of a superconducting flux qubit," *Science*, vol. 299, pp. 1869–1871, 2003.
- [13] T. Yamamoto, Y. A. Pashkin, O. Astafiev, Y. Nakamura, and J. S. Tsai, "Demonstration of conditional gate operation using superconducting charge qubits," *Nature*, vol. 425, pp. 941–944, 2003.
- [14] I. Chiorescu, P. Bertet, K. Semba, Y. Nakamura, C. J. P. M. Harmans, and J. E. Mooij, "Coherent dynamics of a flux qubit coupled to a harmonic oscillator," *Nature*, vol. 431, pp. 159–162, 2004.
- [15] A. S. Srensen, C. H. van derWal, L. Childress, and M. D. Lukin, "Capacitive coupling of atomic systems to mesoscopic conductors," *Phys. Rev. Lett.*, vol. 92, p. 063 601, 2004.
- [16] L. Tian, P. Rabl, R. Blatt, and P. Zoller, *Interfacing Quant. Opt. Solid State Qubits*, to be published.
- [17] P. K. Day, H. G. LeDuc, B. A. Mazin, A. Vayonakis, and J. Zmuidzinas, "A broad-band superconducting detector suitable for use in large arrays," *Nature*, vol. 425, pp. 817–821, 2003.
- [18] G. J. Dolan, "Offset masks for lift-off processing," *Appl. Phys. Lett.*, vol. 31, pp. 337–339, 1977.
- [19] K. Yoshida, K. Watanabe, T. Kisu, and K. Enpuku, "Evaluation of magnetic penetration depth and surface resistance of superconducting thin films using coplanar waveguides," *IEEE Trans. Appl. Supercond.*, vol. 5, no. 2, pp. 1979–1982, Jun. 1995.

## Approaching Unit Visibility for Control of a Superconducting Qubit with Dispersive Readout

A. Wallraff, D. I. Schuster, A. Blais, L. Frunzio, J. Majer, M. H. Devoret, S. M. Girvin, and R. J. Schoelkopf

*Departments of Applied Physics and Physics, Yale University, New Haven, Connecticut 06520, USA*

(Received 27 February 2005; published 1 August 2005)

In a Rabi oscillation experiment with a superconducting qubit we show that a visibility in the qubit excited state population of more than 95% can be attained. We perform a dispersive measurement of the qubit state by coupling the qubit nonresonantly to a transmission line resonator and probing the resonator transmission spectrum. The measurement process is well characterized and quantitatively understood. In a measurement of Ramsey fringes, the qubit coherence time is larger than 500 ns.

DOI: [10.1103/PhysRevLett.95.060501](https://doi.org/10.1103/PhysRevLett.95.060501)

PACS numbers: 03.67.Pp, 42.50.Pq, 85.35.Gv

One of the most promising solid-state architectures for the realization of a quantum information processor [1] is based on superconducting electrical circuits [2]. A variety of such circuits acting as qubits [1], the basic carriers of quantum information in a quantum computer, have been created and their coherent control has been demonstrated [3–8]. Recent experiments have realized controlled coupling between different qubits [9–13] and also first two-qubit quantum logic gates [14].

An outstanding question for superconducting qubits, and in fact for all solid-state implementations of quantum information processors, is whether the qubits are sufficiently well isolated to allow long coherence times and high-fidelity preparation and control of their quantum states. This question is complicated by inevitable imperfections in the measurement. A canonical example is a Rabi oscillation experiment, where the experimenter records the oscillations of a meter's response as a function of pulse length to infer the qubit's excited state population immediately after the pulse. The measurement contrast (e.g., the amplitude of the meter's measured swing relative to its maximum value) is reduced in general by both errors in the qubit preparation and readout, and sets a lower limit on the visibility of oscillations in the qubit population. Most experiments with superconducting qubits to date have reported only the measurement contrast, implying only a lower limit on the visibility in the range of 10%–50% [3–8,14].

A full understanding of the measurement process is required to extract the qubit population from the meter's output. The qubit control is then characterized by the visibility, defined as the maximum qubit population difference observed in a Rabi oscillation or Ramsey fringe experiment. It is essential to demonstrate that a qubit can be controlled without inducing undesired leakage to other qubit states or entanglement with the environment. Some experiments [15] observe a substantial reduction of the visibility due to entanglement with spurious environmental fluctuators [16]. In the few experiments in which the contrast has been characterized, it was close to the expected value [17,18], which implies that high visibility should be achievable with superconducting qubits.

In this Letter, we report results on time-domain control of the quantum state of a superconducting qubit, where the qubit state is determined using a dispersive microwave measurement in a circuit quantum electrodynamics (QED) architecture [19]. This novel technique has shown good agreement with predictions in steady-state experiments [20]. Here, we observe the measurement response, both during and after qubit state manipulation, which is in quantitative agreement with the theoretical model of the system, allowing us to separate the contributions of the qubit and the readout to the observed contrast. The observed contrast of 85% and a visibility of greater than 95% for Rabi oscillations demonstrates that high accuracy control is possible in superconducting qubits.

In our circuit QED architecture [19], a Cooper pair box [21], acting as a two level system with ground  $|\downarrow\rangle$  and excited states  $|\uparrow\rangle$  and level separation  $E_a = \hbar\omega_a = \sqrt{E_{el}^2 + E_J^2}$  is coupled capacitively to a single mode of the electromagnetic field of a transmission line resonator with resonance frequency  $\omega_r$ ; see Fig. 1(a). As demonstrated for this system, the electrostatic energy  $E_{el}$  and the Josephson energy  $E_J$  of the split Cooper pair box can be controlled *in situ* by a gate voltage  $V_g$  and magnetic flux  $\Phi$  [20,22]; see Fig. 1(a). In the resonant ( $\omega_a = \omega_r$ ) strong coupling regime a single excitation is exchanged coherently between the Cooper pair box and the resonator at a rate  $g/\pi$ , also called the vacuum Rabi frequency [22]. In the nonresonant regime ( $|\Delta| = |\omega_a - \omega_r| > g$ ) the capacitive interaction gives rise to a dispersive shift  $(g^2/\Delta)\sigma_z$  in the resonance frequency of the cavity which depends on the qubit state  $\sigma_z$ , the coupling  $g$ , and the detuning  $\Delta$  [19,20]. We have suggested that this shift in resonance frequency can be used to perform a quantum nondemolition (QND) measurement of the qubit state [19]. With this technique we have recently measured the ground state response and the excitation spectrum of a Cooper pair box [20,22].

In the experiments presented here, we coherently control the quantum state of a Cooper pair box in the resonator by applying microwave pulses of frequency  $\omega_s$ , which are resonant or nearly resonant with the qubit transition frequency  $\omega_a/2\pi \approx 4.3$  GHz, to the input port  $C_{in}$  of the resonator; see Fig. 1(a). Even though  $\omega_s$  is strongly de-

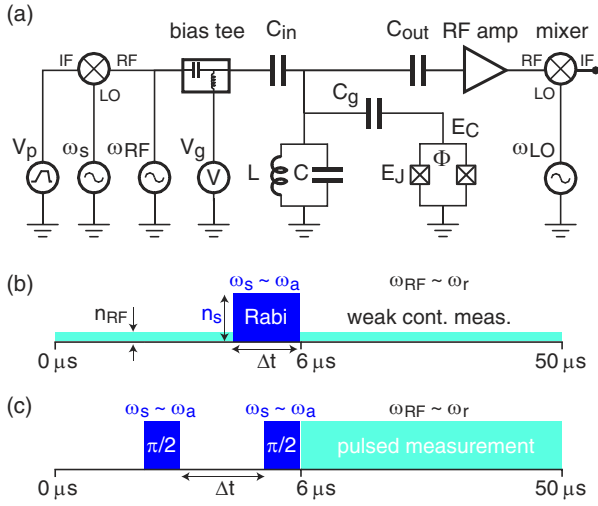


FIG. 1 (color online). (a) Simplified circuit diagram of measurement setup. A Cooper pair box with charging energy  $E_C$  and Josephson energy  $E_J$  is coupled through capacitor  $C_g$  to a transmission line resonator, modeled as parallel combination of an inductor  $L$  and a capacitor  $C$ . Its state is determined in a phase sensitive heterodyne measurement of a microwave transmitted at frequency  $\omega_{RF}$  through the circuit, amplified and mixed with a local oscillator at frequency  $\omega_{LO}$ . The Cooper pair box level separation is controlled by the gate voltage  $V_g$  and flux  $\Phi$ . Its state is coherently manipulated using microwaves at frequency  $\omega_s$  with pulse shapes determined by  $V_p$  [8]. (b) Measurement sequence for Rabi oscillations with Rabi pulse length  $\Delta t$ , pulse frequency  $\omega_s$ , and amplitude  $\propto \sqrt{n_s}$  with continuous measurement at frequency  $\omega_{RF}$  and amplitude  $\propto \sqrt{n_{RF}}$ . (c) Sequence for Ramsey fringe experiment with two  $\pi/2$  pulses at  $\omega_s$  separated by a delay  $\Delta t$  and followed by a pulsed measurement.

tuned from the resonator frequency  $\omega_r$ , the resonator can be populated with  $n_s$  drive photons which induce Rabi oscillations in the qubit at a frequency of  $\nu_{Rabi} = \sqrt{n_s}g/\pi$ . Simultaneously, we perform a continuous dispersive measurement of the qubit state by determining both the phase and the amplitude of a coherent microwave beam transmitted through the resonator at frequency  $\omega_{RF}$  which is resonant or nearly resonant with the resonator frequency  $\omega_r/2\pi \approx 5.4$  GHz [19,22]. The phase shift  $\phi = \tan^{-1}(2g^2/\kappa\Delta)\sigma_z$  is the response of our meter from which we determine the qubit population. For the measurement, we chose a resonator that has a quality factor of  $Q \sim 0.7 \times 10^4$  corresponding to a photon decay rate of  $\kappa/2\pi = 0.73$  MHz. The resonator is populated with  $n \sim 1$  measurement photons on average, where  $n$  is calibrated using the ac-Stark shift [20]. All experiments are performed in a dilution refrigerator at a temperature of 20 mK. The charging energy of the box is  $E_C = e^2/2C \approx h 5.2$  GHz. Details on the device fabrication can be found in Ref. [23].

We initially determine the maximum swing of the meter in a calibration measurement by first maximizing the detuning  $\Delta$  to minimize the interaction ( $g^2/\Delta \rightarrow 0$ ) which defines  $\phi = 0$ . We prepare the Cooper pair box in the

ground state  $|\downarrow\rangle$  by relaxation, the thermal population of excited states being negligible. The box is biased at charge degeneracy ( $E_{el} = 0$ ), where its energy is to first-order insensitive to charge noise [4]. Using flux bias, the detuning is adjusted to  $\Delta/2\pi \approx -1.1$  GHz corresponding to a maximum in the Josephson coupling energy of  $E_J/h \approx 4.3$  GHz  $< \omega_r/2\pi$ . In this case we measure a minimum meter response of  $\phi_{|\downarrow\rangle} = -35.3$  deg corresponding to a coupling strength of  $g/2\pi = 17$  MHz. Saturating the qubit transition by applying a long microwave pulse which incoherently mixes the ground and excited states such that the occupation probabilities are  $P_{|\downarrow\rangle} = P_{|\uparrow\rangle} = 1/2$ , the measured phase shift is found to be  $\phi = 0$ , as expected [20]. From these measurements, the predicted phase shift induced by a fully polarized qubit ( $P_{|\uparrow\rangle} = 1$ ) would be  $\phi_{|\uparrow\rangle} = 35.3$  deg. Thus, the maximum swing of the meter is bounded by  $\phi_{|\uparrow\rangle} - \phi_{|\downarrow\rangle}$ .

In our measurement of Rabi oscillations, a short microwave pulse of length  $\Delta t$  is applied to the qubit in its ground state with a repetition rate of 20 kHz while the measurement response  $\phi$  is continuously monitored and digitally averaged  $5 \times 10^4$  times; see Fig. 1(b). The signal to noise ratio (SNR) in the averaged value of  $\phi$  in an integration time of 100 ns is approximately 25, see Fig. 2, corresponding to a SNR of 0.1 in a single shot. For the present setup the single shot readout fidelity for the qubit state integrated over the relaxation time ( $T_1 \sim 7 \mu s$ ) is approximately 30% [24]. Either a readout amplifier with lower noise temperature or a larger signal power would potentially allow a high-fidelity single shot measurement of the qubit state in this setup.

The time dependence of the averaged value of  $\phi$  in response to a  $\pi$  pulse of duration  $\Delta t \sim 16$  ns applied to the qubit is shown in Fig. 2(a). Before the start of the pulse the measured phase shift is  $\phi_{|\downarrow\rangle} \approx -35.3$  deg corresponding to the qubit being in the ground state. Because of the state change of the qubit induced by the pulse, the resonator frequency is pulled by  $2g^2/\Delta$  and, thus, the measured phase shift is seen to rise exponentially towards  $\phi_{|\uparrow\rangle}$  with the resonator amplitude response time  $2/\kappa \approx 400$  ns, i.e., twice the photon life time. After the  $\pi$  pulse, the qubit excited state decays exponentially with its energy relaxation time  $T_1 \sim 7.3 \mu s$ , as extracted from the decay in the measured phase shift; see Fig. 2(a). As a result, the maximum measured response  $\phi_{max}$  does not reach the full value of  $\phi_{|\uparrow\rangle}$ . In general, the measurement contrast  $C = (\phi_{max} - \phi_{min})/(\phi_{|\uparrow\rangle} - \phi_{|\downarrow\rangle})$  will be reduced in any qubit readout for which the qubit lifetime is not infinitely longer than the measurement response time. Additionally, in non-QND measurements the contrast is reduced even further due to mixing of the qubit states induced by the interaction with the measurement apparatus. In our QND measurement presented here, the qubit lifetime is about 15 times the response time of the measurement, allowing us to reach a high maximum contrast of  $C \sim 85\%$  in the bare measurement response  $\phi$ .

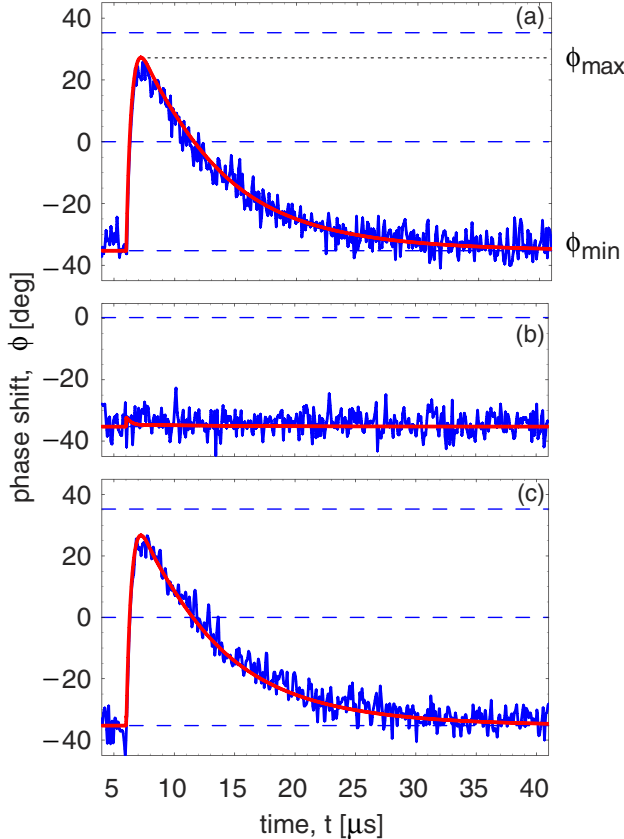


FIG. 2 (color online). Measurement response  $\phi$  (blue lines) and theoretical prediction (red lines) vs time. At  $t = 6 \mu\text{s}$  (a) a  $\pi$  pulse, (b) a  $2\pi$  pulse, and (c) a  $3\pi$  pulse is applied to the qubit. In each panel the dashed lines correspond to the expected measurement response in the ground state  $\phi_{\lfloor\rfloor}$ , in the saturated state  $\phi = 0$ , and in the excited state  $\phi_{\lceil\rceil}$ .

In Figs. 2(b) and 2(c), the measured response  $\phi$  of the meter to a  $2\pi$  and a  $3\pi$  pulse acting on the qubit is shown. As expected, no phase shift is observable for the  $2\pi$  pulse since the response time of the resonator is much longer than the duration  $\Delta t = 32 \text{ ns}$  of the pulse. In agreement with the expectations for this QND scheme, the measurement does not excite the qubit, i.e.,  $\phi_{\min} = \phi_{\max} = \phi_{\lfloor\rfloor}$ . The response to the  $3\pi$  pulse is virtually indistinguishable from the one to the  $\pi$  pulse, as expected for the long coherence and energy relaxation times of the qubit. In the 2D density plot Fig. 3, Rabi oscillations are clearly observed in the phase shift acquired versus measurement time  $t$  and Rabi pulse length  $\Delta t$ .

The observed measurement response  $\phi$  is in excellent agreement with theoretical predictions, see red lines in Fig. 2, demonstrating a good understanding of the measurement process. The temporal response  $\phi(t) = \arg\{i\langle a(t) \rangle\}$  of the cavity field  $a$  is calculated by deriving and solving Bloch-type equations of motion for the cavity and qubit operators [25] using the Jaynes-Cummings Hamiltonian in the dispersive regime [19,20] as the starting

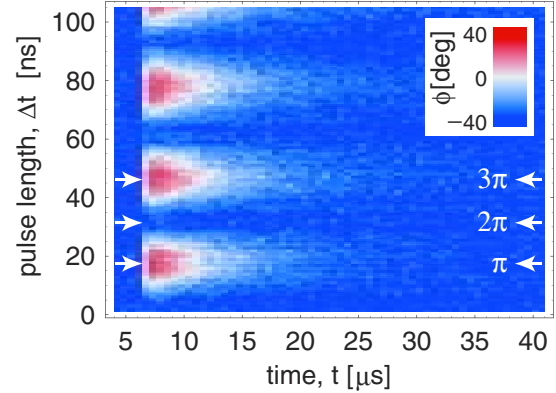


FIG. 3 (color online). Color density plot of phase shift  $\phi$  (see inset for scale) versus measurement time  $t$  and Rabi pulse length  $\Delta t$ . Data shown in Fig. 2 are slices through this data set at the indicated pulse lengths.

point. A semiclassical factorization approximation is done to truncate the resulting infinite set of equations to a finite set (e.g.,  $\langle a^\dagger a \sigma_z \rangle \sim \langle a^\dagger a \rangle \langle \sigma_z \rangle$ ; all lower order products are kept). This amounts to neglecting higher order correlations between qubit and field which is a valid approximation in the present experiment. The calculations accurately model the exponential rise in the observed phase shift on the time scale of the resonator response time due to a state change of the qubit. They also accurately capture the reduced maximum response  $\phi_{\max}$  due to the exponential decay of the qubit. Overall, excellent agreement in the temporal response of the measurement is found over the full range of qubit and measurement time scales with no adjustable parameters; see Fig. 2.

The visibility of the excited state population  $P_{\lceil\rceil}$  in the Rabi oscillations is extracted from the time dependent measurement response  $\phi$  for each Rabi pulse length  $\Delta t$ . We find  $P_{\lceil\rceil}$  by calculating the normalized dot product between the measured response  $\phi$  and the predicted response taking into account the systematics of the measurement. This amounts to comparing the area under a measured response curve to the theoretically predicted area; see Fig. 2. The averaged response of all measurements taken over a window in time extending from the start of the Rabi pulse out to several qubit decay times  $T_1$  is used to extract  $P_{\lceil\rceil}$ . This maximizes the signal to noise ratio in the extracted Rabi oscillations.

The extracted qubit population  $P_{\lceil\rceil}$  is plotted versus  $\Delta t$  in Fig. 4(a). We observe a visibility of  $95 \pm 6\%$  in the Rabi oscillations with error margins determined from the residuals of the experimental  $P_{\lceil\rceil}$  with respect to the predicted values. Thus, in a measurement of Rabi oscillations in a superconducting qubit, a visibility in the population of the qubit excited state that approaches unity is observed for the first time. Moreover, the decay in the Rabi oscillation amplitude out to pulse lengths of 100 ns is very small and consistent with the long  $T_1$  and  $T_2$  times of this charge

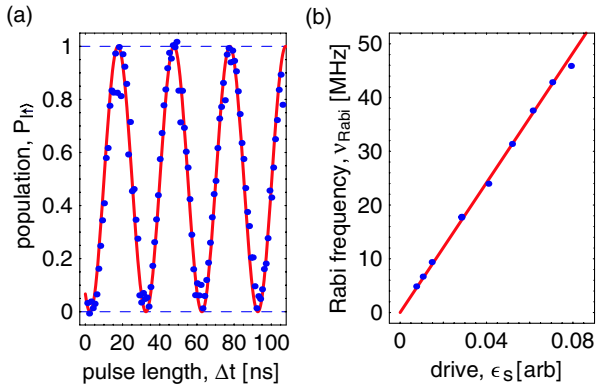


FIG. 4 (color online). (a) Rabi oscillations in the qubit population  $P_{|\uparrow\rangle}$  vs Rabi pulse length  $\Delta t$  (blue dots) and fit with unit visibility (red line). (b) Measured Rabi frequency  $\nu_{\text{Rabi}}$  vs pulse amplitude  $\epsilon_s$  (blue dots) and linear fit.

qubit; see Fig. 4(a) and Ramsey experiment discussed below. We have also verified the expected linear scaling of the Rabi frequency  $\nu_{\text{Rabi}}$  with the pulse amplitude  $\epsilon_s \propto \sqrt{n_s}$ ; see Fig. 4(b).

We have determined the coherence time of the Cooper pair box from a Ramsey fringe experiment at charge degeneracy using  $\pi/2$  pulses of 20 ns duration; see Fig. 1(c). To avoid dephasing induced by a weak continuous measurement beam [20] we switch on the measurement beam only after the end of the second  $\pi/2$  pulse. The resulting Ramsey fringes oscillating at the detuning frequency  $\delta_{a,s} = \omega_a - \omega_s \sim 6$  MHz decay with a long coherence time of  $T_2 \sim 500$  ns; see Fig. 5(a). The corresponding qubit phase quality factor of  $Q_\phi = T_2 \omega_a / 2 \sim 6500$  is

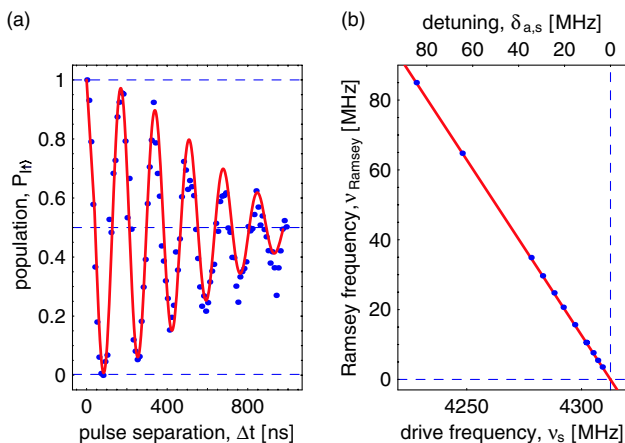


FIG. 5 (color online). (a) Measured Ramsey fringes (blue dots) observed in the qubit population  $P_{|\uparrow\rangle}$  vs pulse separation  $\Delta t$  using the pulse sequence shown in Fig. 1(b) and fit of data to sinusoid with Gaussian envelope (red line). (b) Measured dependence of Ramsey frequency  $\nu_{\text{Ramsey}}$  on detuning  $\delta_{a,s}$  of drive frequency (blue dots) and linear fit (red line).

similar to the best values measured so far in qubits biased at an optimal point [4]. The Ramsey frequency is shown to depend linearly on the detuning  $\delta_{a,s}$ , as expected; see Fig. 5(b). We note that a measurement of the Ramsey frequency is an accurate time resolved method to determine the qubit transition frequency  $\omega_a = \omega_s + 2\pi\nu_{\text{Ramsey}}$ .

In conclusion, performing Rabi and Ramsey experiments we have observed high visibility in the oscillations of state population of a superconducting qubit. The temporal response and the backaction of the readout are quantitatively understood and well characterized. Our charge qubit, which is embedded in a well-controlled electromagnetic environment, has  $T_1$  and  $T_2$  times among the longest realized so far in superconducting systems. The simplicity and level of control possible in this circuit QED architecture makes it an attractive candidate for superconducting quantum computation.

We thank Jay Gambetta for discussions. This work was supported in part by NSA and ARDA under ARO Contract No. DAAD19-02-1-0045, and the NSF under Grants No. ITR-0325580 and No. DMR-0342157, the David and Lucile Packard Foundation, the W.M. Keck Foundation, and the NSERC of Canada.

- 
- [1] M. A. Nielsen and I. L. Chuang, *Quantum Computation and Quantum Information* (Cambridge University Press, Cambridge, 2000).
  - [2] M. H. Devoret, A. Wallraff, and J. M. Martinis, cond-mat/0411174.
  - [3] Y. Nakamura, Y. A. Pashkin, and J. S. Tsai, *Nature* (London) **398**, 786 (1999).
  - [4] D. Vion *et al.*, *Science* **296**, 886 (2002).
  - [5] J. M. Martinis *et al.*, *Phys. Rev. Lett.* **89**, 117901 (2002).
  - [6] Y. Yu *et al.*, *Science* **296**, 889 (2002).
  - [7] I. Chiorescu *et al.*, *Science* **299**, 1869 (2003).
  - [8] E. Collin *et al.*, *Phys. Rev. Lett.* **93**, 157005 (2004).
  - [9] A. J. Berkley *et al.*, *Science* **300**, 1548 (2003).
  - [10] Y. A. Pashkin *et al.*, *Nature* (London) **421**, 823 (2003).
  - [11] J. B. Majer *et al.*, *Phys. Rev. Lett.* **94**, 090501 (2005).
  - [12] I. Chiorescu *et al.*, *Nature* (London) **431**, 159 (2004).
  - [13] R. McDermott *et al.*, *Science* **307**, 1299 (2005).
  - [14] T. Yamamoto *et al.*, *Nature* (London) **425**, 941 (2003).
  - [15] R. Simmonds *et al.*, *Phys. Rev. Lett.* **93**, 077003 (2004).
  - [16] F. Meier and D. Loss, *Phys. Rev. B* **71**, 094519 (2005).
  - [17] T. Duty *et al.*, *Phys. Rev. B* **69**, 140503 (2004).
  - [18] O. Astafiev *et al.*, *Phys. Rev. B* **69**, 180507 (2004).
  - [19] A. Blais *et al.*, *Phys. Rev. A* **69**, 062320 (2004).
  - [20] D. I. Schuster *et al.*, *Phys. Rev. Lett.* **94**, 123602 (2005).
  - [21] V. Bouchiat *et al.*, *Phys. Scr.* **176**, 165 (1998).
  - [22] A. Wallraff *et al.*, *Nature* (London) **431**, 162 (2004).
  - [23] L. Frunzio *et al.*, *IEEE Trans. Appl. Supercond.* **15**, 860 (2005).
  - [24] D. I. Schuster *et al.* (unpublished).
  - [25] A. Blais *et al.* (unpublished).